

Novel Techniques of Optical Detection and Observation of Periodic Crystals

by

Darshan Desai, B.Sc., M.Sc., M.S.

A Dissertation

In

Physics

Submitted to the Graduate Faculty
of Texas Tech University in
Partial Fulfillment of
the Requirements for
the Degree of

Doctor of Philosophy

Approved

Dr. Luis Grave de Peralta
Chair of Committee

Dr. Ayrton A. Bernussi

Dr. Charles W. Myles

Mark Sheridan
Dean of the Graduate School

December 2016

Copyright 2016, Darshan Desai

TABLE OF CONTENTS

ABSTRACT.....	iii
LIST OF FIGURES	iv
CHAPTER 1 INTRODUCTION	1
CHAPTER 2 ULTRA-THIN OPTICAL CONDENSERS	3
Historical Overview	4
Fundamental properties of SPs.....	6
Optical excitation of SPP waves	8
Using SPP waves for microscopy	11
Resolution limit of SP microscopes	16
Non-plasmonic Ultra-Thin Condensers	20
CHAPTER 3 OPTICAL CONDENSERS IN WET-MOUNTING SETUPS	24
Experimental Setup	24
Reconfigurable optical condensers	27
Imaging biological samples over periodic crystals	28
Origin of condenser-like behavior in wet-mounting setups	30
Reconfigurable optical condenser for detection of periodic crystals	34
CHAPTER 4 FOURIER PTYCHOGRAPHIC MICROSCOPY USING HEMISPHERICAL DIGITAL CONDENSERS	42
Experimental Setup	43
FPM image reconstruction algorithm	46
Performance of the FPM image reconstruction algorithm.....	49
Resolution limit of the imaging setups using FPM technique	56
Convergence of the FPM image reconstruction algorithm	62
CHAPTER 5 DUAL-SPACE MICROSCOPY USING HEMISPHERICAL DIGITAL CONDENSERS	64
Implementation of Dual Space Microscopy technique	65
Super-resolution imaging of periodic crystals using DSM technique	70
Convergence of the DSM image reconstruction algorithm.....	72
CHAPTER 6 CONCLUSION.....	76
BIBLIOGRAPHY	80

ABSTRACT

The aim of this dissertation is to demonstrate non-interferometric far-field observation and detection of two-dimensional periodic crystals with truly high lateral resolution at visible frequencies using some of the contemporary techniques. The Plasmonic and Non-plasmonic Ultra-Thin optical condensers based on illumination of object using evanescent surface waves that can be resonantly coupled to propagating waves for imaging with enhanced resolution in the far-field region are discussed. Also, simple and efficient optical condensers formed in wet-mounting setups that can be easily reconfigured for obtaining variable condenser numerical aperture are shown to provide enhanced lateral resolution for optical detection of two-dimensional periodic crystals that are nearly eight times smaller than the Rayleigh resolution limit, and then, using a series of experiments and computations simulations, the origin of mysterious condenser-like behavior in such setups is discussed.

Although it is always possible to tweak the experimental setup for obtaining enhanced lateral resolution, combining numerical processing techniques with experimental process of image acquisition permits even better performance. Optical observation of periodic crystals using phase-retrieval imaging technique called Fourier Ptychographic Microscopy is demonstrated using Hemispherical Digital Condensers. It is demonstrated that for imaging two-dimensional periodic crystals with single spatial periodicity, the resolution limit of Fourier Ptychographic Microscopy is the Rayleigh resolution limit. The source of this limitation on the resolution is demonstrated to have been identified using experiments and computational simulations, and then, a recently proposed technique of imaging two-dimensional periodic crystals called Dual-Space Microscopy that was presented to overcome this limitation is demonstrated to achieve super-resolution imaging of two-dimensional periodic crystals.

LIST OF FIGURES

Figure 2.1	Vacuum-line A cannot produce SPP waves, whereas dielectric line C can produce SPP waves at intersection of the dielectric-line C with SP dispersion curve B when dielectric layer is used. For propagating waves of frequency that is close the asymptotic limit of the non-linear dispersion of SPs, the SPP wave-vector is much larger than the wave-vector of the propagating waves.....	7
Figure 2.2	Schematic diagrams of (a) Otto configuration, and (b) Kretschmann configuration. Electric fields in the metal layer, and magnetic fields are not shown in the diagrams. Green arrow indicates incident light.....	9
Figure 2.3	Simulated angular response of the dielectric-metal structure. The resonant absorption is a signature of generation of SPP waves.....	10
Figure 2.4	Surface plasmon microscope [40].....	13
Figure 2.5	Experimental results demonstrating that the images in SP microscopes are produced due to coherent superposition of waves. Back focal-plane images shown in (d-f) are produced using structures shown in (a-c) [68]......	15
Figure 2.6	The polarization of leakage radiation from SPP waves. The white line indicates the transmission axis of the polarizer placed below the objective lens [39]......	16
Figure 2.7	Process of fabricating the two-dimensional periodic crystals of chromium pillars to be observed using non-plasmonic UTCs.....	18
Figure 2.8	(a-b) Real plane images, and (c-d) corresponding Fourier plane images produced using (a, c) plasmonic UTC, and (b, d) plasmonic UTC with a drop of water over the top surface. The white arrow in image (c) indicates central bright zero order diffraction ring. The circular arc in image (d) has been drawn to indicate the increased diameter of the circular condenser rings in comparison to those in image (c) [40]......	19
Figure 2.9	Process of fabricating the two-dimensional periodic crystals of chromium pillars to be observed using non-plasmonic UTCs.....	21
Figure 2.10	(a-b) Real plane images, and (c-d) corresponding Fourier plane images that are obtained using (a, c) non-plasmonic UTC, and (b, d) non-plasmonic UTC with a large drop of water over the top surface [40]......	22

Figure 3.1	Images (a-b) show the experimental setups used for the results shown in this chapter. Images (c-d) show the photographs of an add-on optical module made by cutting the top-part of an oil-immersion objective lens, which can be used in setup shown in image (b). [79]	25
Figure 3.2	Comparison of the efficiency of optical condensers is shown using the back focal-plane images (d), (e), and (f), which are obtained by the imaging the structures shown in (a), (b), and (c) respectively. [78]	26
Figure 3.3	Schematic diagrams of Reconfigurable condensers are shown in images (a), (c), and (h). Image (b) shows variation of condenser numerical aperture with the space thickness of the structure sketched in image (a). Images (d-g) and (i-l) show variation in condenser numerical aperture as the drop of liquid with low boiling point evaporates over the structure in images (c) and (h) respectively. [78, 79]	28
Figure 3.4	Images of live <i>Escherichia coli</i> strands that are obtained using the coverslip-sandwich structure sketched in Fig. 3.2(c). The real plane image (a) shows a bacterial strand over the two-dimensional periodic structure of chromium pillars with $p=300$ nm periodicity, and image (b) is the corresponding back focal-plane image. The scale bar in image (a) corresponds to $2\ \mu\text{m}$. [78]	29
Figure 3.5	Real plane images (a, c, e), and back focal-plane images (b, d, f) are obtained by illuminating chromium pillars structure with the “simplest possible microscope condenser” sketched in Fig. 3.3(h). Images (g-h) are the corresponding back focal-plane images obtained using coverslip-sandwich structure sketched in Fig. 3.3(h). [79]	30
Figure 3.6	Images (b-c) are obtained on putting spatial filter as shown in (a) show better contrast than images (d-e) obtained without spatial filter, using coverslip-sandwich structure. Images (g, i, k) obtained using collimated perpendicular light beam incident on (f, h, j), respectively, indicates that scattering at the inner edge causes formation of circular condenser rings. [78]	33
Figure 3.7	Images (a-b) show pair of real plane and back focal-plane images of periodic crystal of chromium pillars obtained using an oil-immersion objective lens, and images (c-d) show a pair of real plane and back focal-plane images obtained from add-on optical module shown in Fig. 3.1(c, d), which was made from the same	

objective lens. Image (e) shows the procedure to obtain simulated real plane in (f). Images (g-h) show add-on optical module filled with index matching oil, and images (i-j) show the inability of such structure to produce circular condenser rings. [79]..... 35

Figure 3.8 Images shown in (a-d) are the back focal-plane images of the sample structure in Fig. 3.3(h), and images shown in (e-h) are the back focal-plane images of the sample structure in Fig. 3.3(c). [79] 39

Figure 3.9 Ray-optics simulations that demonstrate that the efficiency of the “simplest microscope condenser structure” and coverslip-sandwich condenser structure can be attributed to cavity-based resonance. [79] 40

Figure 4.1 Image (a) shows experimental setup with HDC sources. Images (b-d) show the images acquired for chromium pillars structure using setup shown in image (a). Images (e-f) show images of nanowires using (e) perpendicularly incident white light, and (f) HDC source. Intensity profiles of nanowire in images (e-f) clearly indicates resolution enhancement. [84] 43

Figure 4.2 FPM image reconstruction process. Images (a-d) show the simulated real space and Fourier space intensity and phase corresponding to periodicity $p=500$ nm. Images (e-h) show process to obtain low resolution real space intensity, and corresponding phase. Images (i-l) show results of FPM reconstruction. [95] 50

Figure 4.3 Images (a-b) show experimentally acquired low resolution images of chromium pillars structure with periodicities of 300 nm and 500 nm in mutually perpendicular directions with $NA_o=1.3$. Images (c-e) show the real plane, Fourier plane, and real plane phase obtained after FPM image reconstruction. [100] 52

Figure 4.4 Images (a-b) and (c-d) are the pairs of real plane and Fourier plane obtained using $NA_c=0.58$ and 0.73 , respectively, and images (e-f) are corresponding FPM reconstructed images. Images (g-h) is the pair of real plane and Fourier plane images obtained using $NA_c=0.97$. Images (i-j) and (l-m) are FPM reconstructed images, which are obtained using $NA_c=0.87$ and 0.97 , and all low resolution real plane images, respectively. Images (j) and (l) show the region of interest corresponding to area marked with red square in images (k) and (n). [100] 53

Figure 4.5	Images (a-b) are reconstructed images corresponding to $p=500$ nm period, for $NA_c=0.87$ and 0.97 . Image (c) shows the expected location of diffraction spots for different condenser numerical aperture values. [95, 100].....	55
Figure 4.6	FPM reconstructed images corresponding to (a-b) $NA_c=0.58$ and 0.73 , and (c-d) $NA_c=0.87$ and 0.97 . [100].....	56
Figure 4.7	FPM reconstructed images for period $p=267$ nm that have an incorrect period of 459 nm in image (a), which can be verified by incorrect location of diffraction spikes at $NA=0.97$ in image (b). [95].....	57
Figure 4.8	FPM reconstructed images for period $p=500$ nm that have an incorrect period of 459 nm in image (a) when only simulated low resolution real space intensity corresponding to $NA_c=0.87$ and 0.97 are used, which can be verified by incorrect location of diffraction spikes at $NA=0.97$ in (b). [95]	58
Figure 4.9	Low resolution real space and corresponding Fourier space intensity and phase in the initial steps of FPM process is shown in images (a-d). On using correct phase shown in (f) that is obtained from simulations, the initial shift in Fourier space results in correct location of diffraction spike at the end of iteration. [95].....	60
Figure 4.10	Images in (a, b) show real space intensity and phase that serves as the object under observation. The corresponding FPM reconstructed real space intensity and phase is shown in images (c-d). Images (e-h) show the beginning of the process for $NA_c=0.87$ in the first iteration of the FPM reconstruction process. [95].....	61
Figure 4.11	Convergence of the FPM image reconstruction algorithm. Average normalized mean-square error metric for thousands of periodicities in the following ranges (a) $300 \text{ nm} < p < 600 \text{ nm}$, and (b) $260 \text{ nm} < p < 280 \text{ nm}$, for numerical aperture value of $NA_o=0.8$ corresponding to the objective lens. [95]	63
Figure 5.1	(a) is RP image that serves as the object, and (b) is the corresponding FP image. (c-d) is a pair of simulated low resolution RP image and corresponding FP image obtained using $NA_c=0.97$. (e-f) is a pair of reconstructed RP image and corresponding FP image obtained from processing simulated images. (g-h) is a pair of experimentally acquired low resolution RP image and corresponding FP image obtained using $NA_c=0.97$. (i-j) is a pair of reconstructed RP image and corresponding	

	FP image obtained from processing experimental images. [97].....	68
Figure 5.2	Pairs of reconstructed RP and FP images obtained using (a-b) simulated images, and (c-d) experimentally acquired images. [97].....	69
Figure 5.3	Pairs of reconstructed RP and FP images obtained from (a-b) simulated images, (c-d) experimentally acquired RP and FP images, and (e-f) experimentally acquired RP and FP images that were processed to remove noise related to reflections from the inner surface of the digitally controlled HDC source. [97].....	71
Figure 5.4	(a) Average normalized mean-squared error-metric for Group 1. (b-c) Reconstructed real space and Fourier space for $p=500$ nm from Group 1. [96]	72
Figure 5.5	(a) Average normalized mean-squared error-metric for Group 2. (b-c) Reconstructed real space and Fourier space for $p=267$ nm from Group 2. [96]	73
Figure 5.6	(a) Average normalized mean-squared error-metric for Group 3. (b-c) Reconstructed real space and Fourier space for $p_1=267$ nm, $p_2=400$ nm, and $p_3=667$ nm, which belongs to Group 3. [96]	74

CHAPTER 1

INTRODUCTION

Bright-field microscopy is the simplest optical characterization technique, where the object under observation is illuminated with white-light, and the light that is transmitted through the object is collected by an objective lens for observation in the far-field region. In 1873, Ernst Abbe discovered that the lateral resolution from such imaging setups is limited, and proposed using inclined illumination from optical condensers to double the maximum possible lateral resolution in bright-field microscopy technique. The traditional design of optical condensers proposed by Abbe is still widely used for biological and industrial imaging applications, however, the imaging setups with traditional design of optical condensers suffer from two major limitations: (1) it involves bulky mechanical and optical parts, and (2) are diffraction-limited. This dissertation is dedicated to study of some of the techniques have been proposed to overcome these limitations.

Chapter 2 presents ultra-thin optical condensers that are based on illumination of object using evanescent surface waves, which can be resonantly coupled to propagating waves for imaging with enhanced resolution in the far-field region. Two types of ultra-thin condensers can generate evanescent surface waves: (1) Plasmonic ultra-thin condensers, which are based on using Surface Plasmon Polariton waves, and (2) Non-plasmonic ultra-thin condensers, which are based on total-internal-reflection based evanescent surface waves. These ultra-thin condensers are smaller than the conventional optical condensers by several orders of magnitude, and can provide true sub-wavelength resolution.

Chapter 3 presents optical condensers formed in wet-mounting setups, which can function as simple and efficient optical condensers. These sample-setups can be easily reconfigured for obtaining variable condenser numerical aperture. The condenser-like illumination from such sample-setups can provide enhanced lateral resolution for optical detection of periodic crystals that are nearly eight times smaller

than the Rayleigh resolution limit. Using a series of experiments and computations simulations, the origin of mysterious condenser-like behavior of the sample-setups that are commonly used for biological imaging is revealed.

Chapter 4 presents implementation of Fourier Ptychographic Microscopy using Hemispherical Digital Condensers. Fourier Ptychographic Microscopy is a novel phase-retrieval imaging technique that uses a set of low resolution real plane images to construct a high resolution image of the object under observation, while simultaneously calculating the unmeasured phase. Using experimental observations and computational simulations, it is demonstrated that this technique provides diffraction-limited performance, i.e. the resolution limit is the Rayleigh resolution limit, for the periodic crystals with single spatial periodicity.

Chapter 5 presents the recently proposed Dual-Space Microscopy using Hemispherical Digital Condensers. Dual Space Microscopy processes experimentally acquired Fourier plane images along with low resolution real plane images to construct a high resolution image of the object under observation, while simultaneously calculating the unmeasured phase. Using experimental observations and computational simulations, it is demonstrated that this technique can be used to image two-dimensional periodic crystals with single spatial periodicity that is smaller than the Rayleigh resolution limit.

Chapter 6 presents the conclusion of this dissertation, and possible directions for future work.

CHAPTER 2

ULTRA-THIN OPTICAL CONDENSERS

Most of the conventional imaging techniques use bulky structures with lenses and diaphragms as optical condensers to provide inclined illumination to object under observation. In order to overcome this limitation, evanescent surface waves can be used to illuminate and observe the sample with high resolution after resonantly coupling them to the propagating waves. The aim of this chapter is to demonstrate the implementation of non-interferometric far-field imaging of nanoscale objects with truly high lateral resolution at visible frequencies, using two different techniques of illumination using surface waves: plasmonic evanescent surface waves excited using fluorescent molecules, and non-plasmonic total internal reflections related evanescent waves.

According to the Drude's theory of metals, electromagnetic field oscillations of light can produce coherent collective time-dependent longitudinal oscillations of the polarization charge at a perfectly planar interface formed by linear, homogeneous, isotropic, and lossless dielectric and metal layers. Unlike s-polarized component of the incident light, the p-polarized component encounters a discontinuity of electric displacement vector at the interface, which permits such charge density oscillations. The quanta of such charge density oscillations existing over a dielectric-metal surface are called Surface Plasmons (SPs). Also, SPs form hybrid pseudo-particles by resonantly coupling with the incident photons, which are known as Surface Plasmon Polaritons (SPPs). As the name of this hybrid pseudo-particle suggests, the plasmon-related energy is located in metal layer, and the polariton-related energy is located in the polarized dielectric layer. A group of many propagating SPPs is called SPP wave. One of the most interesting feature of such structures is that classical electrodynamics would be sufficient to analyze SPPs because the properties of SPPs are subsumed in the dielectric function in the constituent layers [1]. For this reason, the interfacial electromagnetic fields at nanoscale can be easily studied, which is why Surface Plasmonics has grown so rapidly. SPP waves are highly useful for high resolution

imaging of nanostructures because the corresponding electromagnetic fields can be conveniently manipulated by altering refractive index experienced by SPP waves [2]. The scientific and technological developments that result from the study of electromagnetic fields generated due to the interaction of electromagnetic radiation that is incident on dielectric-metal interfaces have been subsumed in the field of study known as Surface Plasmonics.

Historical Overview

In the onset of twentieth century, Wood reported experimental observation of narrow anomalous minimum in the intensity of the light reflected by metal gratings [3]. This is a signature of generation of optical excitation SPP waves, but the phenomenon was not well explained in those times. In 1941, Fano provided first theoretical explanation of the optical excitation of SPP waves [4]. In 1951, Bohm and Pines revealed that the electrons incident on metals lose their energy to collective oscillations of conduction electrons that are created due to the long range nature of the Coulomb interactions [5]. Pines theoretically described how SPP waves can be generated by incident electrons, and termed this collective excitation a ‘plasmon’ [6], a quantum of the previously known Langmuir waves [7], whereas the term ‘polariton’ was first used by Fano for a hybrid pseudo-particle that is formed by coupling of incident photons and bound electrons in dielectric layer [8]. Theoretical framework explaining SPs was first published by Ritchie in 1957 [9], which was experimentally corroborated by Powell and Swann using electron energy loss spectroscopy of Aluminum thin-films [10]. Stern and Ferrell termed these excitations ‘surface’ plasmons in their publication demonstrating how relaxation effects occurring due to oxidation at the surface affects generation of SPs [11]. In 1964, Turbadar revealed that Wood’s reflection anomaly can explained using the conventional theory of thin-films, instead of attributing it to generation of SPs. [12]. In 1968, Otto [13], and Kretschmann [14] invented relatively low-cost techniques for convenient optical excitation of SPPs, due to which Surface Plasmonics was gradually subsumed in the field of Optics. In the same year, Ritchie et al experimentally demonstrated for the first time that Wood’s anomaly can be attributed to generation of SPP waves [15]. In 1974, Cunningham et al coined the term ‘surface plasmon polariton’ for the first time

in scientific literature [16]. By this time, Surface Plasmonics was used for a diverse range of applications in various interdisciplinary fields. In 1987, first SP-based microscopy was reported by Yeatman and Ash, who used laser illumination and Kretschmann configuration to image nearly 3 nm thick dielectric structures on silver thin-films [17]. In 1991, Lenferink et al reported a technique based on vibrating mirror setup to scan for SPP resonance angle [18]. In 1994, Bruijn et al reported a technique of rapidly rotating the sample to obtain better resolution in all directions on the surface [19]. In 1994, Berger et al experimentally reported that the lateral resolution of surface plasmon based microscope depends on the propagation distance of SPPs [20]. In 1996, Yeatman first detailed experimental study of a surface plasmon microscope with several other setups. He reported that the lateral resolution of surface plasmon microscopes is inversely proportional to its sensitivity [21]. Following this, various imaging techniques based on using high numerical aperture objective lens [22], interferometry [23], dark-field configuration [24], fluorescence [25-26], solid immersion lens [27], ellipsometry [28], and several other mechanisms have been published.

A lot of progress was also made in near-field plasmonic imaging at the onset of twenty-first century [29-30]. These near-field plasmonic imaging techniques, however, require post-processing of acquired images, which prohibits real-time imaging. In 2005, Smolyaninov combined the near-field plasmonic imaging technique with far-field imaging to obtain high spatial resolution [31-32]. Smolyaninov used glycerin-gold interface to create SPP waves with a very small wavelength. However, as this technique combines the near-field imaging with far-field imaging, an unconventional imaging setup is required, and special image processing techniques have to be used to reconstruct the image from the acquired data. Likewise, a lot of progress has also been made towards obtaining super-resolution. In 2000, Pendry reported a theoretical framework proposing use of metal thin-films as superlenses [33]. Following this, Melville et al reported experimentally achieved near-field super-resolution by using silver thin-film as a plasmonic lens [34]. Two years later, high resolution far-field images were experimentally demonstrated using novel imaging structure called hyperlens [35], which consisted of cylindrically-layered metamaterial structure, and

was originally proposed by Pendry and Ramakrishna [36]. Far-field high resolution imaging using superlenses was also experimentally demonstrated [37], which was based on theoretical framework proposed by Durant et al [38]. In 2009, Frisbie et al experimentally reported far-field sub-wavelength imaging using a novel structure based on fluorescently illuminating a metal thin-film deposited on a glass substrate [39]. Recently, Desai et al and Grave de Peralta have reported that there are striking similarities between the ultra-thin plasmonic structures used for imaging and conventional design of far-field superlenses, and hence, with further advancement in science of materials, the super-resolution limit shall be easily overcome in the near future [40, 41].

Surface Plasmonics has grown very rapidly over the last few decades because of the advancement of nanofabrication techniques and clean-room facilities. Also, advancements in numerical and image processing techniques and in techniques for simulating electromagnetic processes have contributed a lot in the growth of Surface Plasmonics. In the next section, the fundamentals of generating surface plasmons over a dielectric-metal interface are presented and discussed.

Fundamental properties of SPs

An ‘ideal’ structure to reveal the properties of plasmons is a semi-infinite dielectric-metal interface whose layers are lossless, linear, homogeneous, isotropic, non-magnetic, and non-chiral. The non-linear dispersion relation for a p-polarized SPP wave that propagates such dielectric-metal interface can be obtained using appropriate boundary conditions in the Maxwell’s formalism:

$$\frac{\omega}{c} = \left[\frac{\epsilon_m + \epsilon_d}{\epsilon_m \epsilon_d} \right]^{1/2} k_{spp} \quad (1.1)$$

Here, $\epsilon_m(\omega)$ and $\epsilon_d(\omega)$ are the permittivities for metal and dielectric layer, respectively. Permittivity $\epsilon_z(r, \omega)$ assumes value of ϵ_m in the metal layer, and the value of ϵ_d in the dielectric layer. As real metals have electrical resistance, $\epsilon_m(\omega)$ also has a non-zero imaginary component, and hence, the energy associated with SPPs is absorbed by the metal layer as it propagates. Consequently, the electromagnetic field intensity of the SPPs decreases exponentially with the distance parallel to the interface

and in the direction perpendicular to the interface, such that the propagation length of SPPs on such ideal structure is inversely proportional to imaginary component of wave-vector that is perpendicular to the interface, and the depth of penetration into the dielectric layer is inversely proportional to imaginary component of wave-vector that is parallel to the interface [42].

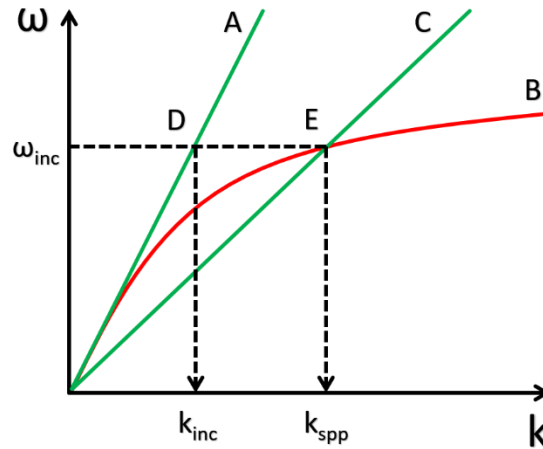


Figure 2.1 Vacuum-line A cannot produce SPP waves, whereas dielectric line C can produce SPP waves at intersection of the dielectric-line C with SP dispersion curve B when dielectric layer is used. For propagating waves of frequency that is close the asymptotic limit of the non-linear dispersion of SPs, the SPP wave-vector is much larger than the wave-vector of the propagating waves.

However, for simplicity, assume that the constituent layers do not offer any internal damping, and in accordance with Drude's theory of metals, if the permittivity of the metal layer is $\epsilon_m = 1 - \left(\frac{\omega_p}{\omega}\right)^2$, where ω_p is the plasmon frequency of the metal. In such case, when the frequency-dependent permittivities of the dielectric and metal layer are real and positive, it can be shown that the generated plasmons are not bound to the interface and do not attenuate in the media. These are called Brewster VP (volume-plasmon) modes, because of absorption of the p-polarized light incident at Brewster's angle that causes these modes. Moreover, if the frequency-dependent permittivities of the constituent layers are real and opposite in sign, the generated plasmons are propagating evanescent waves that are bound to the interface, which can exist with a broad range of frequencies up to $\frac{\omega_p}{\sqrt{1+\epsilon_d}}$. Such modes are known as Fano modes. The qualitative dispersion of Fano SP modes the interface of dielectric-metal

structure is sketched in Fig. 2.1. In order to couple the Fano SP modes with the incident light, the dispersion curves for Fano SP modes must intersect with the dispersion line for the light in air/vacuum. The SPP waves can be generated only when the SPs are coupled to incident photons, else, the SPs would simply exist as evanescent waves near the interface. Note that for light incident at higher frequency, the corresponding SP resonance wave-vector is much larger than the wave-vector of the incident light.

Optical excitation of SPP waves

The prism-coupling techniques suggested by Otto and Kretschmann can be used for optical excitation of SPP waves, which are shown in Fig. 2.2(a) and 2.2(b) respectively. By putting a dielectric layer with an effective refractive index that is larger than that of air/vacuum, the dispersion line for light in that dielectric layer can be made to intersect with the dispersion curve for Fano SP modes. In Otto's configuration, the incident p-polarized light causes total internal reflection related evanescent surface waves at the surface of the prism adjoining the other dielectric (which is usually air/vacuum). The evanescent surface waves penetrate the thin dielectric layer to produce SPs over the metal layer. At a particular angle of incident light, the total internal reflection related evanescent surface waves radiatively couple with the SPs to form SPPs. Electrical resistance in the metal layer causes emission related to internal damping losses, which permits far-field detection of the generation of SPs [13]. Kretschmann, on the other hand, proposed to put a relatively low dielectric layer over the metal layer, as shown in Fig. 2.2(b), so that total internal reflection related evanescent surface waves penetrate the thin metal layer to produce SPs [14]. At a particular angle of incidence, corresponding resonant coupling results in generation of SPP waves at the metal-dielectric interface on the other side of the structure. These techniques form a dielectric light-line in the dispersion diagram that can intersect the non-linear dispersion curve for the Fano SP mode. However, Kretschmann's technique is based on resonant emission, whereas Otto's technique is based on resonant absorption. Consequently, Kretschmann's configuration is widely used for plasmonic imaging. There are several other optical excitation methods, like

coupling using periodic structures [43], coupling using waveguides [44], scattering due to roughness or microscopic structures [45-46], and various other methods.

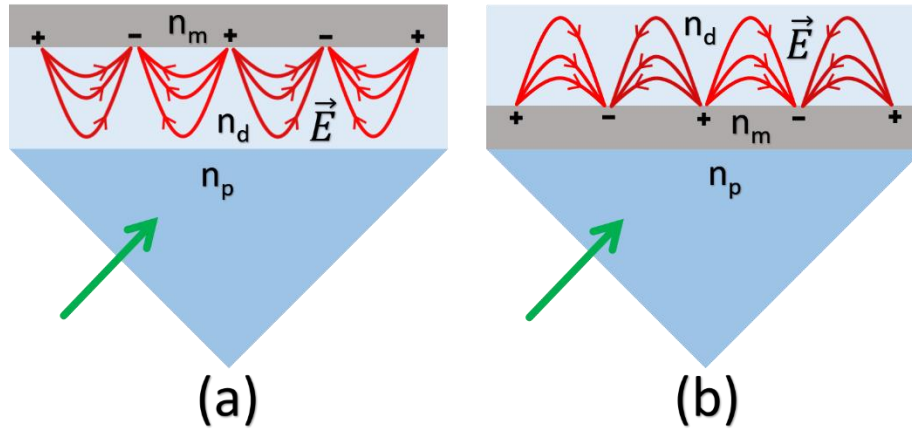


Figure 2.2 Schematic diagrams of (a) Otto configuration, and (b) Kretschmann configuration. Electric fields in the metal layer, and magnetic fields are not shown in the diagrams. Green arrow indicates incident light.

The dispersion relation of SPs can provide the surface plasmon resonance wave-vector, which can be used to determine the surface plasmon resonance angle. The dispersion relation of SPs in semi-infinite dielectric-metal plasmonic structure differs from the realistic plasmonic structures in the laboratory, because SPs strongly depend on their ambience. If the effective refractive index of the SPP waves does not alter significantly due to presence of microscopic objects, dispersion relations for dielectric-metal-dielectric structures reported by Burke et al, or even more complex plasmonic structures can be used [47, 48]. However, when microscopic objects under observation significantly alter the effective refractive index of the evanescent surface waves, deriving an analytical expression for realistic plasmonic structures is very difficult. Also, as most of the conventional experimental methods record data for discrete wave-vectors, experimental determination of dispersion relation with conventional techniques is a tedious process [49]. The most convenient approach to determine the surface plasmon resonance angle is to use reflections from the plasmonic structure. The waves reflected back from the metal layer causes an anomalous minimum in the reflected light intensity due to destructive interference, simultaneously resulting enhancement in interfacial electromagnetic fields [50].

As shown in Fig. 2.3, the intensity of the p-polarized light that is reflected from the plasmonic dielectric-metal structure shown in Fig. 1(b) indicates that nearly none of the incident light is specularly reflected, which is a signature of generation of SPP waves. For this, the simulated plasmonic structure consists of 240 nm thick PMMA superstrate, 50 nm thick gold layer, and a 150 μm thick BK-7 glass substrate. Using technique described in Ref. [48], simulations were conducted for a collimated light beam with p-polarization, which was incident on the interface, at every possible angle of incidence [51].

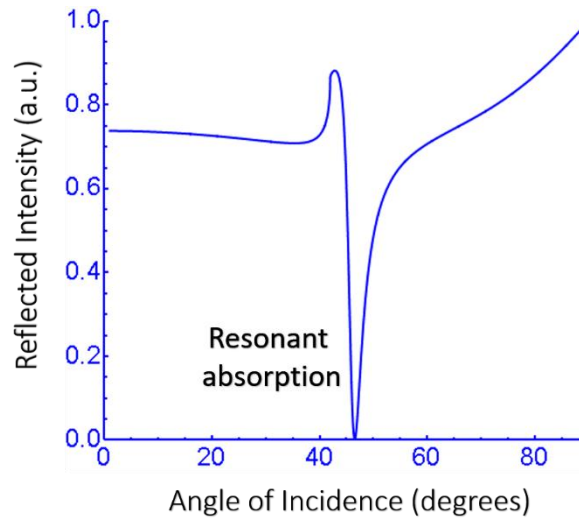


Figure 2.3 Simulated angular response of the dielectric-metal structure. The resonant absorption is a signature of generation of SPP waves.

These interfacial electromagnetic fields are relatively lesser for thinner metal layers because of the change in the amount of reflected intensity. Consequently, if the thickness of the metal layer is increased, the interfacial electromagnetic fields are more enhanced, until the coupling between the modes is reduced to an extent that starts affecting field enhancement adversely, and hence, a certain thickness of metal layer would result in optimum coupling [52]. When the metal layer is sufficiently thin, the electromagnetic fields on one surface of the metal layer can penetrate it to reach the other layer, which can result in a pair of non-degenerate coupled SP modes, which consists of a lower frequency long-range SP mode with symmetric charge distribution, and a higher frequency (lossy) short-range SP mode with anti-symmetric charge distribution [53-54]. The dispersion relation of the SPs also depends on the material

forming the substrate and superstrate, and corresponding thicknesses [55, 56]. Usually, plasmonic structures are characterized by asymmetry - the superstrate is usually thinner than the substrate by a few orders of magnitude. When the thickness of the superstrate layer is increased, the intensity of the reflected light does not change, however, leakage radiation is emitted at relatively larger angle, and corresponding angular spread of the emission of leakage radiation also increases [57]. The substrate is usually much larger than the wavelength of illumination, and hence, in practice, it can be considered to be infinitely thick. As the interfacial electromagnetic fields have to penetrate the superstrate layer to “map” the microscopic objects under observation, a thinner layer with higher refractive index can be used to increase the effective refractive index of SPP waves. Moreover, if the dielectric substrate is lossy, the angle of emission of leakage radiation would depend more strongly on the thickness of the dielectric layer. An important thing to note here is that when the real part of the permittivity of the metal layer is zero, despite generation of SPP waves, the reflected light intensity does not have a minimum for the SP resonance wave-vector. This suggests that when the permittivity of the metal layer is not known, it becomes necessary to know the phase of the reflection coefficient [58]. For the p-polarized light, the rate of change of phase of the reflection coefficient of (which rapidly changes by 360-degrees across “location” for resonance) with respect to the wave-vector of the SPP waves corresponds to the propagation length of the SPPs [59]. Note that for perfectly planar surfaces, the neither the intensity, nor the phase of the reflection coefficient of the s-polarized light show any features related to generation of SPP waves, suggesting that s-polarized light cannot generate SPP waves on a plasmonic structure with perfectly smooth surfaces (unless it is possible to use a negative refractive index material in place of metal layer). It is necessary to know the phase of the reflection coefficient for a precise estimation of the resonance wave-vector related to generation of SPP waves [60], however, for most of the plasmonic imaging setups, a rough estimate of the resonance wave-vector angle is sufficient.

Using SPP waves for microscopy

SPP waves can be optically generated by putting a relatively thin dielectric superstrate layer of fluorescent molecules uniformly dispersed in PMMA over a thin

metal layer deposited on a glass coverslip substrate [25]. The light that is incident perpendicularly on such plasmonic structure excites the fluorescent molecules. Rhodamine-6G (Rh-6G) molecules can be used to provide fluorescence, which can be most efficiently excited at around 530 nm, and the emission maximum is around 570 nm [62]. Some of the lower frequency light that gets scattered by fluorescent molecules corresponds to the relatively large resonance wave-vector associated with generation of SPP waves. Interfacial electromagnetic fields associated with the generated SPP waves can penetrate a thin dielectric layer to “map” the microscopic objects placed over the dielectric layer with enhanced resolution, and hence, thinner dielectric superstrate layer is preferred. However, very thin superstrate layer (< 10 nm) should be avoided to prevent non-radiative quenching of fluorescent Rh-6G molecules. Diffracted SPP waves permit observation of objects in the far-field region due to leakage radiation emission that occurs because of radiative coupling [17, 63]. The leakage radiation appears at an angle that satisfies the condition $k_{spp} = nk_o \sin \theta$, where k_{spp} is the SPP wave-vector, k_o is the in-plane component of the illuminating wave-vector, and θ is the polar angle for emission. Thus, SPP waves that are radiatively coupled to the propagating waves emitted by fluorescence can be detected in the far-field region by collecting corresponding leakage radiation using a conventional imaging setup consisting of a high numerical aperture oil-immersion objective lens.

An experimental setup to accomplish this is as shown in Fig. 2.4. The normally-incident continuous-wave laser source at 532 nm is used to illuminate the Rh-6G molecules. The leakage radiation from the structure is collected by a high numerical aperture (NA_o) oil-immersion objective lens, and is band-pass filtered at the fluorescence emission peak (which is 570 nm for the Rh-6G molecules) to filter-out the excitation wavelength. The light is then imaged at the real plane (RP) and Fourier plane (FP) simultaneously using two CCD cameras. The SPP waves propagating in any one direction on the interface would be emitted as leakage radiation with a very narrow polar angle, which corresponds to bright spot in the back focal-plane of the light collecting objective lens.

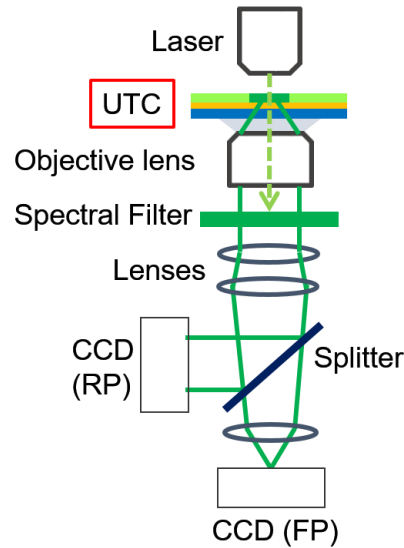


Figure 2.4 Surface plasmon microscope [40]

For a perfectly planar interface, the SPP waves propagate in all directions, and consequently, the light propagating over all directions on the interface results in a circular ring of narrow width, which is centered at the center of the FP [64]. The radial intensity profile of the circular ring has a Lorentzian distribution across the circumference [65]. For the emitted leakage radiation that can be captured by the oil-immersion objective lens, the back focal-plane of the oil-immersion objective lens forms a map of the component of the resonance wave-vector of the SPP waves that are propagating parallel to the interface. Consequently, the effective refractive index experienced by the SPP waves can be determined from the circular ring formed in the back-focal plane of the oil-immersion objective lens [66]. On the other hand, when microscopic objects are placed over the plasmonic structure for observation, some of the intensity of the SPP waves that is diffracted by the microscopic objects gets captured by the oil-immersion objective lens in form of leakage radiation, and is distributed in the back focal-plane of the oil-immersion objective lens, along with the transmitted light forming the central bright ring.

Analysis of leakage radiation in the back focal-plane of the oil-immersion objective lens can reveal several important features of the SPP waves. For example, despite the fact that the fluorescence emission is largely incoherent, the image formation occurs because of coherent superposition of the light waves. This occurs

because wavelength of the SPPs waves is smaller than the coherence length of the fluorescence emission [67]. This fact can be ascertained from the results shown in Fig. 2.5. The dielectric layers in Fig. 2.5(a-c) are approximately 110 nm thick, whereas the uniformly deposited gold layer is approximately 50 nm thick. Fig. 2.5(c) has additional periodic crystal of 50 nm thick gold ridges approximately 2 μm width that are patterned with 4 μm periodicity. On illuminating the plasmonic structure shown in Fig. 2.5(a) with a Laser source, the emitted fluorescence emitted from the bottom PMMA+Rh-6G layer destructively interferes with leakage radiation from the excited SPP waves. Consequently, the back focal-plane image shown in Fig. 2.5(d) that corresponds to the plasmonic structure shown in Fig. 2.5(a) contains a uniformly bright background due to fluorescence emission, with two darks circular rings observed due to destructive interference at effective refractive index of $n=1.01$ and $n=1.24$. Appearance of two SPP modes can be attributed to larger thickness of dielectric layers. The occurrence of destructive interference in this case indicates that the image formation is a result of coherent superposition of waves. For 570 nm wavelength of leakage radiation is spectrally band-pass filtered at 10 nm bandwidth, the coherence length of the fluorescence is determined to be $\lambda^2/\Delta\lambda \approx 30 \mu\text{m}$, which is larger than the coherence length of the SPP waves (20 μm). However, on illuminating the structure shown in Fig. 2.5(b), the fluorescence from the top dielectric layer is expected to get reflected from the metal layer, whereas the leakage radiation is emitted downwards. Consequently, the back focal-plane image shown in Fig. 2.5(e) that corresponds to the plasmonic structure shown in Fig. 2.5(b) contains bright circular rings corresponding to the leakage radiation emission at same angles as that for the dark circular rings in Fig. 2.5(d). The back focal-plane image shown in Fig. 1.5(f) corresponds to the structure shown in Fig. 2.5(c), and resembles the back focal-plane image that is produced by illuminating a grating with plasmonic UTC. As the optical disturbance in the Fourier plane is proportional to the Fourier transform of the optical disturbance in the real plane, image formation must have occurred due to coherent interaction between the leakage radiation and the emitted fluorescence [68].

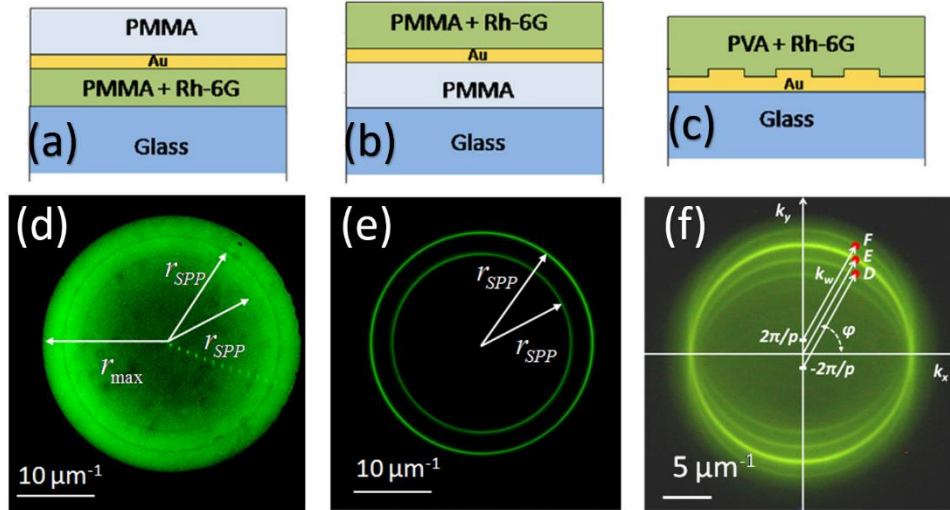


Figure 2.5 Experimental results demonstrating that the images in SP microscopes are produced due to coherent superposition of waves. Back focal-plane images shown in (d-f) are produced using structures shown in (a-c) [68].

Another characteristic of SPP waves that can be studied from the analysis of the back-focal plane is its polarization. Note that altering the thickness of the dielectric superstrate can result in multiple modes from the plasmonic structure, and the asymmetry of the plasmonic structure can also result in s-polarized modes. The SPP waves propagating over the interface change the path on leaking into the substrate, and hence, for a p-polarized SPP wave, the electric field component is radially oriented at the back focal-plane of the oil-immersion objective lens. Likewise, the electric field component of the s-polarized SPP wave is tangential at the back focal-plane of the oil-immersion objective lens [69]. This fact can be verified by inserting a Polarizer in the back focal-plane of the oil-immersion objective lens, which results in the FP images shown in Fig. 2.6. As shown in Fig. 2.6, multiple modes of SPP waves can be excited in the plasmonic structure with 42 nm silver layer coated with poly vinyl alcohol (PVA) doped with Rh-6G fluorescent molecules. When polarizer is inserted in the optical path of the leakage radiation, if the intensity of the leakage radiation decreases in along the transmission-axis of the polarizer, the SPP mode has the s-polarization, whereas if the intensity decreases along the direction perpendicular to the transmission-axis of the polarizer, the SPP mode has p-polarization. Hence, an alternating sequence of s-polarization and p-polarization SPP modes is visible in Fig. 2.6.

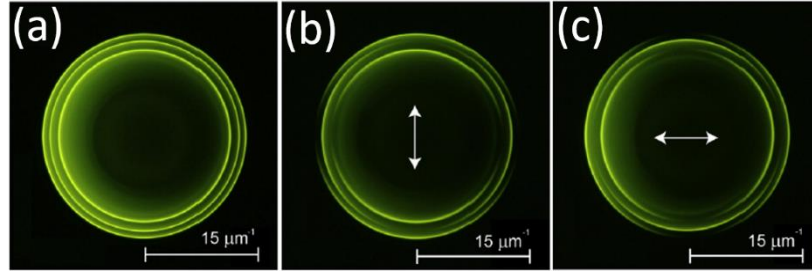


Figure 2.6 The polarization of leakage radiation from SPP waves. The white line indicates the transmission axis of the polarizer placed below the objective lens [39].

Resolution limit of SP microscopes

The quantitative evaluation of the performance of the conventional imaging techniques can be directly performed from the back focal-plane of the oil-immersion objective lens, when the object under observation is a two-dimensional periodic structure. For such structures, the diffraction spots are actually “copies” of the spot centered in the Fourier plane, which corresponds to the light that gets transmitted through the two-dimensional periodic object under observation, and are distributed in the back focal-plane of the oil-immersion objective lens with the same symmetry as that of the object under observation. Abbe’s theory of image formation states that the periodicity of the object can be observed in the real plane of the imaging setup only when two or more consecutive diffraction spots are visible in the Fourier plane along the direction of periodicity. The traditional design of optical condensers provides inclined illumination to the object under observation, so that the diffraction features in the back focal-plane of the oil-immersion objective lens is extended, and hence, on using an optical condenser, the narrow spot corresponding to perpendicular illumination is replaced by a large spot (disc) corresponding to inclined illumination. Note that the presence of such feature in the back focal-plane indicates that the periodic object has been illuminated with a solid cone of light.

Similar principle can be used in case of Surface plasmon microscopes. When a periodic structure is used as an object under observation, the light that is transmitted through the object without being diffracted forms a circular ring that is centered at the center of the Fourier plane, and the leakage radiation corresponding diffracted SPP waves appear as circular rings with centers at the location of the expected location of the diffraction spots, and these diffraction features are arranged with a symmetry

corresponding to the periodic object. Moreover, as stated in the previous section, circular ring is a consequence of SPP waves propagating in all directions over the interface. Consequently, Abbe's theory of image formation can be extended to state that in Surface plasmon microscopes, the periodicity of the object is visible in the real plane as long as two or more consecutive circular diffraction features are at least partially visible in the back focal-plane of the oil-immersion objective lens along the direction of periodicity of the object. Note that the diffraction features in Surface plasmon microscopes, the circular rings, indicate that the object under observation has been illuminated with a hollow cone of light, and hence, plasmonic structures used in imaging can be thought of as optical condensers. Clearly, such structures not only provide better contrast than the traditional design of optical condensers, but their physical size is lesser by several orders of magnitude. This is why such structures are known as plasmonic Ultra-Thin Condensers (UTCs).

The two-dimensional periodic structure that serves as a mechanism for benchmarking the resolution of the Surface plasmon microscope can be fabricated with the help of a combination of electron beam lithography and lift-off techniques. The periodic structure may consist of 15 nm high chromium pillars arranged with desired lattice symmetry, which are fabricated over a 50 nm thick gold layer that adheres to the 150 μm thick glass coverslip with the help of uniformly deposited 2 nm thick chromium layer [66]. As indicated in Fig. 2.7, metal layers can be deposited using electron beam physical vapor deposition (EBPVD) process, and then, 100 nm thick PMMA layer is spin-coated. Then the structure undergoes electron beam lithography, where the exposed regions of the PMMA are ready to be etched out using a solution of methyl-isobutyl-ketone (MIBK) and isopropanol (IPA) solution in appropriate proportions. Then, 15 nm thick layer of chromium is deposited using EBPVD process. Finally, the structure is rinsed in acetone to remove the residual PMMA, thereby creating the required two-dimensional structure. Finally, uniform mixture of Rh-6G molecules and PMMA solution is used to spin-coat 240 nm thick layer exhibiting fluorescence.

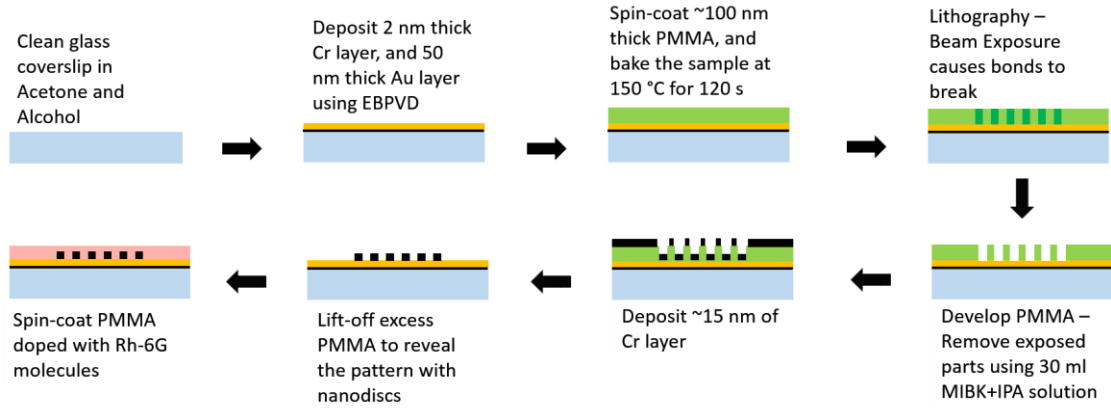


Figure 2.7 Process of fabricating the two-dimensional periodic crystals of chromium pillars to be observed using non-plasmonic UTCs.

The fabricated structure in Fig. 2.7 can now be used for quantitative evaluation of the performance of the Surface plasmon microscope. The minimum observable periodicity of the object in Surface plasmon microscope is given by the following equation:

$$p_{min} = \frac{2\pi}{k_{max} + k_{spp}} = \frac{\lambda}{NA_o + NA_c} \quad (1.2)$$

This equation indicates that the lateral resolution of the Surface plasmon microscope is better than conventional microscopy, especially when low numerical aperture objective lenses have to be used. The plasmonic UTCs also provide better image contrast than conventional imaging techniques, which has been experimentally demonstrated for Surface plasmon microscopy of various types of nanoparticles [70]. The fact that the size of the circular rings corresponds to the effective refractive index experienced by the SPP waves permits dark-field configuration by depositing a thick dielectric layer over the structure, whose refractive index is larger than that corresponding to the diffraction limit of for the objective lens for perpendicular illumination. Pairs of images in Fig. 2.8 show the intensity distribution in the real plane and Fourier plane of the Surface plasmon microscope with oil-immersion objective lens with numerical aperture of $NA_o=1.3$, for a periodic crystal with periodicity $p=400$ nm in mutually perpendicular directions, which are obtained without the water drop over the plasmonic structure (Fig. 2.8(a, c)), and with the drop of water over the plasmonic structure (Fig. 2.8(b, d)). Note that the zeroth order

circular diffraction ring cannot be captured by the oil-immersion objective lens, and only first and second order diffraction rings that are partially captured by the oil-immersion objective lens are distributed in the back focal-plane of the oil-immersion objective lens with the square symmetry that corresponds to the periodicity of the object under observation. As seen in the corresponding image captured real plane of the Surface plasmon microscope, in accordance with the Abbe's theory of image formation, the periodicity of the object under observation is clearly visible.

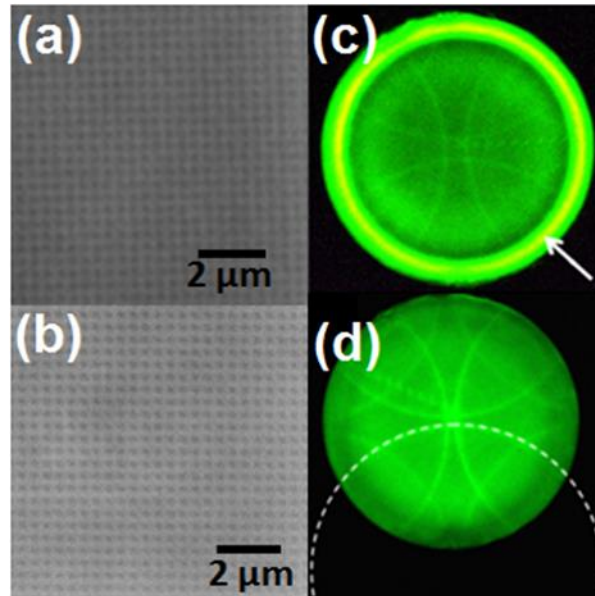


Figure 2.8 (a-b) Real plane images, and (c-d) corresponding Fourier plane images produced using (a, c) plasmonic UTC, and (b, d) plasmonic UTC with a drop of water over the top surface. The white arrow in image (c) indicates central bright zero order diffraction ring. The circular arc in image (d) has been drawn to indicate the increased diameter of the circular condenser rings in comparison to those in image (c) [40].

Non-periodic microscopic objects can also be characterized by analyzing how SPP waves are modulated during propagation. When a non-periodic object is observed in a Surface plasmon microscope, the leakage radiation corresponding to diffracted SPP waves will produce features in the back focal-plane of the oil-immersion objective lens, which may or may not be easily recognized easily on observation. Nanofabricated patterns can also be used to create various kinds of optical elements, for example, a sequence of nanoparticles can function as a beam-splitter, and a sequence of metal rods can function as a Bragg mirror. Prisms and waveguide structures fabricated over metal layer can be used for desired modulation of SPPs.

Also, the diffraction-limited performance of dielectric lenses can be overcome if they can be fabricated over a metal layer [71]. Comprehensive study of various types of nanofabricated optical elements has been done by several research groups [72-75].

Non-plasmonic Ultra-Thin Condensers

Many types of surface waves on dielectric-dielectric interface have been discovered, and are classified on the basis of the properties of the constituent materials, but most of these surface waves cannot be used due to large propagation lengths occurring because of low losses in dielectrics. However, one of the most common types of surface waves on dielectric structures are the total internal reflection related evanescent surface waves. One such possible structure can be created by simply by depositing a layer of PMMA that is uniformly doped with fluorescent Rh-6G molecules (superstrate) over a glass coverslip (substrate). In such case, due to reciprocal Goos-Hanchen effect, the fluorescence emitted in all directions produces surface waves that leak into the substrate [76]. However, in such cases, the radiative coupling with the propagating waves emitted by fluorescent Rh-6G molecules occurs at all angles that are larger than the critical angle for total internal reflection. Hence, for a non-plasmonic structure without any microscopic objects on the top surface, a thick band-like illumination is observed in the back focal-plane of the oil-immersion objective lens.

For quantitative evaluation of the performance of non-plasmonic structures, two-dimensional periodic structures can be fabricated over the glass substrate, as shown in Fig. 2.9. The nanofabrication process begins by cleaning a 150 μm thick glass substrate by rinsing it in acetone and isopropanol, and then spin-coating it with a PMMA layer of approximately 100 nm thickness. Then, an aluminum layer with 10 nm thickness is thermally evaporated over this structure to avoid charge deposition during electron beam lithography. Electron beam lithographic breaks the bonds in the exposed regions of the PMMA layer. To remove the aluminum layer, the structure is rinsed in hydrofluoric acid. The exposed parts of the structure can now be removed using a solution of methyl isobutyl ketone and isopropanol. Nearly 15 nm of chromium is deposited over the template of holes using EBPVD process. Then,

acetone is used to remove the PMMA layer, which leaves a periodic structure with chromium pillars over the glass coverslip. Finally, a PMMA layer with 240 nm thickness, and a uniform distribution of fluorescent Rh-6G molecules is spin-coated on this structure. The experimental setup used for this purpose is the same as Surface plasmon microscopes. These non-plasmonic structures used in imaging also behave like condensers in the experimental setups, and hence, are known as non-plasmonic UTCs.

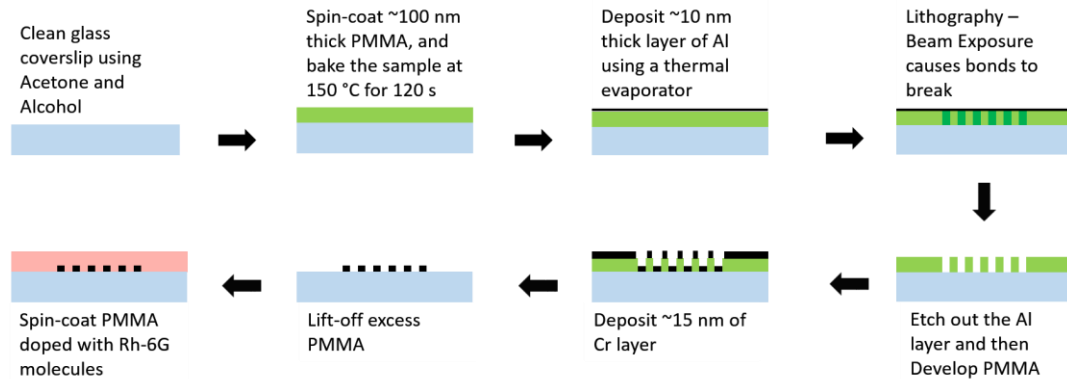


Figure 2.9 Process of fabricating the two-dimensional periodic crystals of chromium pillars to be observed using non-plasmonic UTCs.

When the periodicity of the object under observation is less than that corresponding to the diffraction limit, the back focal-plane of the oil-immersion objective lens consists of a thick continuous band of wave-vectors. This band consists of the light transmitted by the structure that corresponds to zeroth order diffraction by the object, and hence, the illumination band extends from an effective refractive index of nearly 1.00 corresponding to air layer above the PMMA, to the effective refractive index of 1.49 corresponding to the PMMA layer. When the numerical aperture of the oil-immersion objective lens is less than effective refractive index of PMMA layer, only a part of the zeroth order diffraction is captured by the objective lens. When a periodic object is illuminated by total internal reflection related evanescent surface waves from such non-plasmonic structure, the evanescent surface waves are diffracted by the periodic structures, and then leak into the higher refractive index glass substrate, which then gets collected by the oil-immersion objective lens. The diffracted evanescent surface waves leak to form diffraction bands that are distributed with the symmetry that corresponds to the periodicity of the object under observation. Fig.

2.10(c) shows the back focal plane image of a two-dimensional periodic crystal of chromium pillars with a periodicity $p=300$ nm in mutually perpendicular directions, which was obtained using an oil-immersion objective lens with $NA_o=1.3$. Note that in accordance with the Abbe's theory of image formation, the periodicity of the object is visible in the real plane image shown in Fig. 2.10(a).

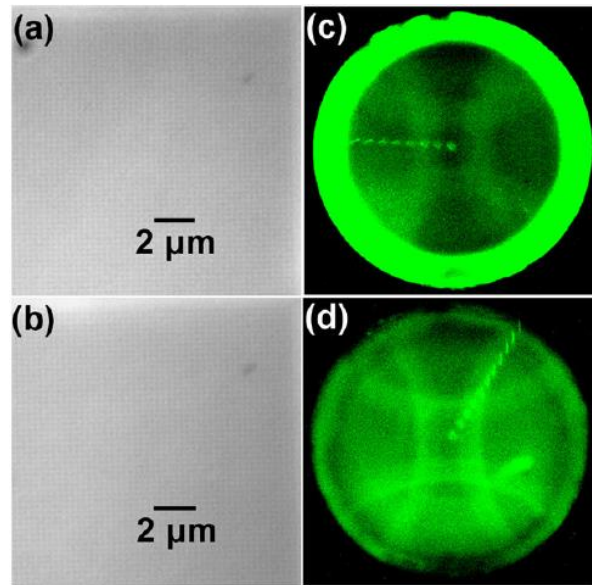


Figure 2.10 (a-b) Real plane images, and (c-d) corresponding Fourier plane images that are obtained using (a, c) non-plasmonic UTC, and (b, d) non-plasmonic UTC with a large drop of water over the top surface [40].

Because evanescent surface waves are involved in imaging, corresponding dark-field imaging configuration can be obtained by depositing a dielectric layer over the structure. Or, by simply putting a water-drop over the structure, the total internal reflection can be made to occur from angle that corresponds to the effective refractive index of water, and consequently, the zeroth order diffraction band cannot be collected by the oil-immersion objective lens, as shown in the image of the back focal-plane of the oil-immersion objective lens in Fig. 2.10(d). Corresponding real plane image shown in Fig. 2.11(b) reveals the periodicity of the object under observation. For two-dimensional periodic crystals, the periodicity can be easily determined from the first order diffraction features that are partially visible in the back focal-plane of the oil-immersion objective lens. Non-plasmonic UTCs may suffer from relatively lower contrast because the fluorescence emitted in all directions creates a uniform background in the FP of the imaging setup. Especially when a part of the first order

diffraction bands fall over the central zeroth order diffraction band, image processing and background correction techniques can be used to reveal the first order diffraction bands [77].

In the imaging setups with plasmonic and non-plasmonic UTCs, the light collected by the objective lens also limits the lateral resolution, and hence, direct (lensless) observation techniques can be employed for limitless resolution. Plasmonic UTCs may have excellent potential for true super-resolution non-interferometric far-field imaging, as the effective refractive index experienced by the evanescent surface waves is limited only by choice of good material for the dielectric layer. In accordance with Abbe's theory of image formation, images in the real plane of the microscope do not contain any information about the higher frequencies, but higher order diffraction features can be found in back-focal plane, and hence, may be used to "stitch" larger effective numerical aperture by overlapping images acquired using a low boiling point liquid with dielectric properties that results in a variable effective refractive index for SPP waves, while simultaneously acquiring unrecorded phase, as done in different phase retrieval techniques.

CHAPTER 3

OPTICAL CONDENSERS IN WET-MOUNTING SETUPS

In plasmonic and non-plasmonic UTCs, as fluorescence is emitted in all directions, a uniform background illumination is created in the back focal-plane of the oil-immersion objective lens. In absence of uniform background illumination, the visibility could be even better for imaging applications [40]. Also, fluorescent molecules irreversibly decompose due to continuous absorption and emission cycles, eventually leaving them unable to fluoresce. In this chapter, unexpected condensers that are formed in the wet-mounting setups are presented, which do not use fluorescence for illumination [78]. Also, using experimental results and computational simulations, the origin of the condenser-like behavior of these optical condensers is discussed [79]. Moreover, a technique to easily reconfigure these unexpected optical condensers for achieving variable condenser numerical aperture using an add-on optical module is discussed in this chapter.

Experimental Setup

The experimental setup sketched in Fig. 3.1(a) is used to perform the experiments described in this chapter that are conducted with an oil-immersion objective lens. A commercially available inverted Nikon Ti-Eclipse microscope is mounted with an oil-immersion objective lens of numerical aperture of $NA_o=1.49$. The spatial beam-block can be placed in the back focal-plane of the objective lens, to remove the un-deviated light that is transmitted through the structure. A spectral band-pass filter is used in combination with the microscope's built-in white light illumination source to have partially coherent light beam fall perpendicularly over the object under observation. For experiments described in this chapter, the wavelength of the illumination coming through the spectral band-pass filter is 570 nm, with approximately 10 nm bandwidth. After the light is transmitted through the structure, it is collected by the oil-immersion objective lens, and simultaneously imaged at real plane and back focal-plane of the imaging setup using two CCD cameras.

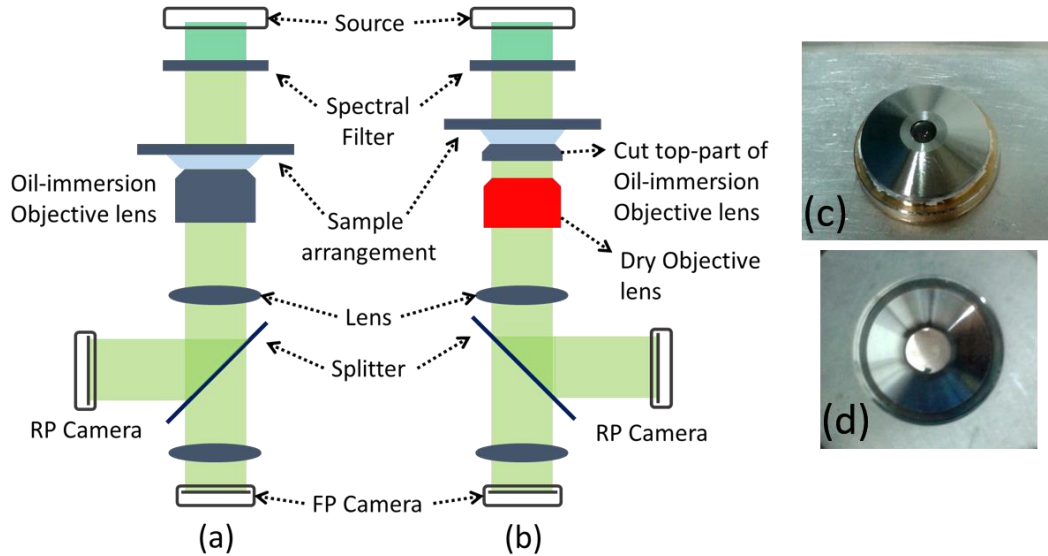


Figure 3.1 Images (a-b) show the experimental setups used for the results shown in this chapter. Images (c-d) show the photographs of an add-on optical module made by cutting the top-part of an oil-immersion objective lens, which can be used in setup shown in image (b). [79]

Comparison of optical condensers

Fig. 3.2(a-c) show the imaging structures used to obtain the images of the back focal-plane of the oil-immersion lens (with $NA_o=1.49$) that are shown in Fig. 3.2(d-f), while imaging the two-dimensional periodic structures of chromium pillars that are patterned on a glass coverslip substrate with a square symmetry in horizontal and vertical directions with a period of $p=300$ nm, height $h=15$ nm, and distance $d=p/2$ between the chromium pillars. This structure was fabricated using the process described in Fig. 2.9. Fig. 3.2(d) was obtained using a plasmonic UTC sketched in Fig. 3.2(a), with 50 nm thick gold layer adhering to the glass coverslip with the help of 2 nm chromium layer. Fig. 3.2(e) was obtained using a structure of chromium pillars fabricated on glass coverslip, which was introduced as “simplest possible condenser” structure in the literature [80], which is sketched in Fig. 3.2(b). The bright spot in the center of the back focal-plane image in Fig. 3.2(e) corresponds to light transmitted through the structure without being diffracted. Consequently, the numerical aperture of the bright spot, $NA_c \sim 0.35$, corresponds to nearly perpendicular illumination from the microscope’s built-in white-light source. The absence of the corresponding first order diffraction spots from the image suggests that the periodicity is less than

minimum observable periodicity for perpendicular illumination. The presence of first order diffraction rings in the back focal-plane of the oil-immersion objective lens indicates that the structure behaves like a condenser. As seen in the image from the back focal-plane of the oil-immersion objective lens shown in Fig. 3.2(e), the other diffraction orders could not be captured by the oil-immersion objective lens, and hence, in accordance with the Abbe's theory of image formation [81], the periodicity of the object shall not be visible in the real plane of the microscope. The periodicity of the object under observation can still be easily determined from the back focal-plane of the light-collecting oil-immersion objective lens.

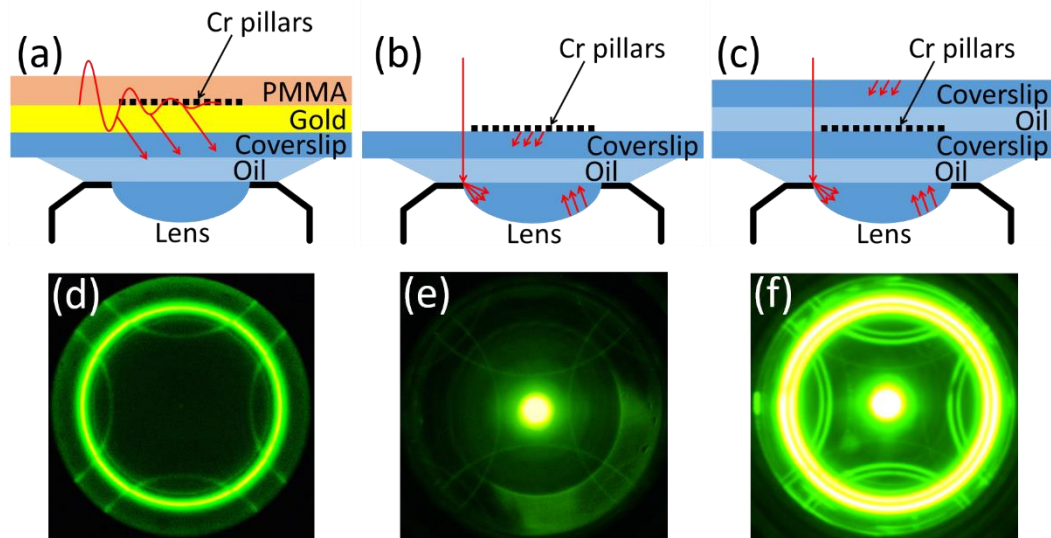


Figure 3.2 Comparison of the efficiency of optical condensers is shown using the back focal-plane images (d), (e), and (f), which are obtained by the imaging the structures shown in (a), (b), and (c) respectively. [78]

Fig 3.2(f) was obtained by the structure sketched in Fig. 3.2(c), which was created by depositing a drop of Nikon's index-matching oil with a refractive index of 1.515 (at normal temperature and pressure) over the glass coverslip containing periodic structure with chromium pillars, and then covering it with another glass coverslip. In accordance with the Abbe's theory of image formation [81], the presence of the consecutive diffraction orders in the back focal-plane of oil-immersion objective lens indicates that the periodicity of the object will be visible in the corresponding real plane of the microscope. Similar coverslip-sandwich structure is frequently used in biological laboratories as wet-mounting setup. A comparison of the images that are

obtained from the back focal-plane of the oil-immersion objective lens shown in Fig. 3.2(d-f), it is clear that the coverslip-sandwich structure provides the best contrast. Also, the circular rings appearing in the back focal-plane of the oil-immersion objective lens shown in Fig 3.2(e) and 3.2(f) suggests that the object under observation was illuminated with hollow cones of light, and hence, behave like optical condensers. The condenser numerical aperture of the partially appearing first order circular diffraction rings appearing in the back focal-plane of oil-immersion objective lens was determined to be nearly 1.50 when the “simplest possible condenser” structure shown in Fig. 3.2(a) was used. Note that the circular condenser rings with similar numerical aperture can be found when coverslip-sandwich structure was used.

Reconfigurable optical condensers

There are two ways in which coverslip-sandwich structures permit variation of the condenser numerical aperture using the geometry of the structure: (1) by altering the thickness of the liquid layer in between the coverslips by changing the spacer thickness, as indicated in Fig. 3.3(a), and (2) by depositing a liquid with a low boiling point over the coverslip-sandwich structure. As shown in Fig. 3.3(b), the condenser numerical aperture decreases as the thickness of the liquid layer between the coverslips is increased. From the graph, the variation of condenser numerical aperture with the spacer thickness was determined to be as per $NA_c = -St + R_0$, where the rate of change of condenser numerical aperture is $S=0.6 \times 10^{-3} \mu\text{m}^{-1}$, and the condenser numerical aperture corresponding to the zero thickness is found to be $R_0=1.505$. This suggests that the coverslip-sandwich structure is a systematically reconfigurable optical condenser. Another approach to obtain a variable condenser numerical aperture is to deposit a large drop of a liquid with low boiling point, like methanol, over the coverslip-sandwich structure. Fig. 3.3(c) schematically shows the coverslip-sandwich structure with a large drop of a low boiling point liquid over the top surface. The drop of liquid over the structure would evaporate with time, which is observed to cause a variation in the diameter of the circular condenser rings in the back-focal plane of the oil-immersion objective lens, as shown in Fig. 3.3(d-g). The most important feature of such easily reconfigurable condensers is that the ambiance of the object under observation does not change with the condenser numerical aperture. Likewise, the

“simplest possible condenser” structure that is shown in Fig. 3.3(h) also permits similar variation in the numerical aperture by depositing a drop of low boiling-point liquid over the top surface, as shown in Figs. 3.3(i-l).

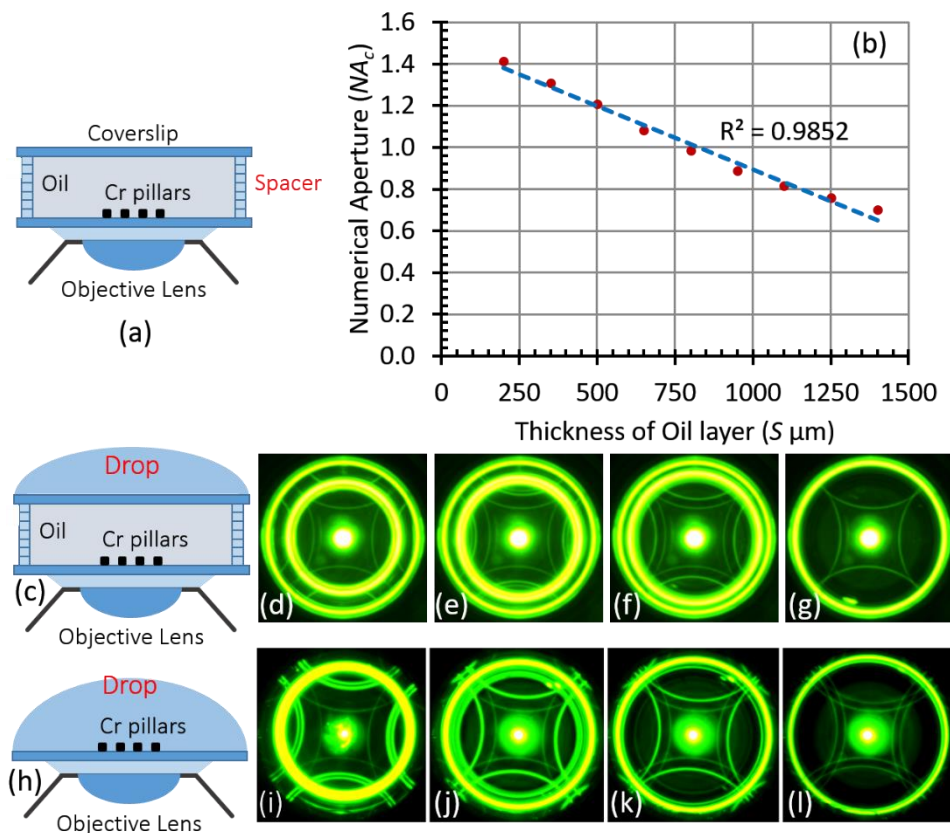


Figure 3.3 Schematic diagrams of Reconfigurable condensers are shown in images (a), (c), and (h). Image (b) shows variation of condenser numerical aperture with the space thickness of the structure sketched in image (a). Images (d-g) and (i-l) show variation in condenser numerical aperture as the drop of liquid with low boiling point evaporates over the structure in images (c) and (h) respectively. [78, 79]

Imaging biological samples over periodic crystals

Water can be used as the liquid used in the coverslip-sandwich structure to facilitate the imaging of biological structures. In order to demonstrate the performance of the coverslip-sandwich arrangement, a solution of live *Escherichia coli* strands mixed in distilled water can be used to form the coverslip-sandwich structure. When this coverslip-sandwich structure is used for imaging, the images formed in real plane and back focal-plane of the oil-immersion objective lens is shown in Fig. 3.4. The cylindrical *Escherichia coli* strand over the two-dimensional periodic crystals are

clearly visible in the real plane images. The size of the cylindrical strand in the real plane image is determined to be approximately $0.65\ \mu\text{m}$. The periodicity of the two-dimensional periodic crystal of chromium pillars over which *Escherichia coli* are lying is $p=300\ \text{nm}$ in the mutually perpendicular directions, and the chromium pillars are distributed with square symmetry over the glass coverslip.

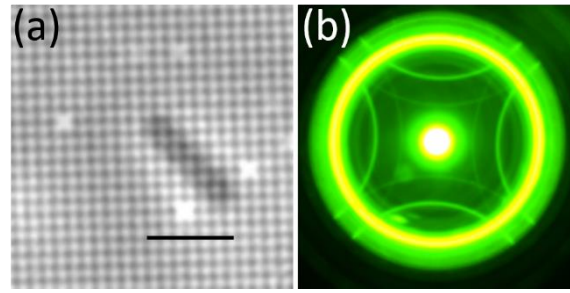


Figure 3.4 Images of live *Escherichia coli* strands that are obtained using the coverslip-sandwich structure sketched in Fig. 3.2(c). The real plane image (a) shows a bacterial strand over the two-dimensional periodic structure of chromium pillars with $p=300\ \text{nm}$ periodicity, and image (b) is the corresponding back focal-plane image. The scale bar in image (a) corresponds to $2\ \mu\text{m}$. [78]

The periodicity of the two-dimensional periodic crystal can be determined from the back focal-plane of the oil-immersion objective lens shows the zeroth order circular diffraction ring centered at the Fourier plane along with the partially visible first order circular diffraction rings. The absence of the first order diffraction spots corresponding to the bright central spot from the microscope's built-in source indicates that the periodicity of the two-dimensional periodic crystal is less than the resolution limit with perpendicular illumination. This indicates that the coverslip-sandwich structure results in true sub-wavelength resolution. The resolution limit of the experimental setup using coverslip-sandwich structure can be expressed by the equation that also governs the resolution limit for traditional design of optical condensers and the UTCs (equation 1.2). This indicates that the minimum possible periodicity with nearly perpendicular illumination ($NA_c=0.35$), when the numerical aperture for the objective lens is $NA_o=1.49$ can be determined to be $p_{min}\sim 370\ \text{nm}$. However, on using coverslip-sandwich structure, the condenser numerical aperture can be increased to up to $NA_c=NA_o$, and hence, the corresponding minimum observable periodicity gets reduced to $p_{min}\sim 190\ \text{nm}$. Moreover, the presence of the *Escherichia*

coli strand indicates that the coverslip-sandwich structures are useful for bio-medical imaging applications.

Origin of condenser-like behavior in wet-mounting setups

The circular condenser rings observed in the images of back focal-plane of the oil-immersion objective lens that are shown in Fig. 3.3(d-g) are strikingly similar despite being obtained with different imaging structures shown in Fig. 3.3(i-l), and hence, results of further studies have been shown in Fig. 3.5 to reveal the common physical mechanism that produces the circular condenser rings.

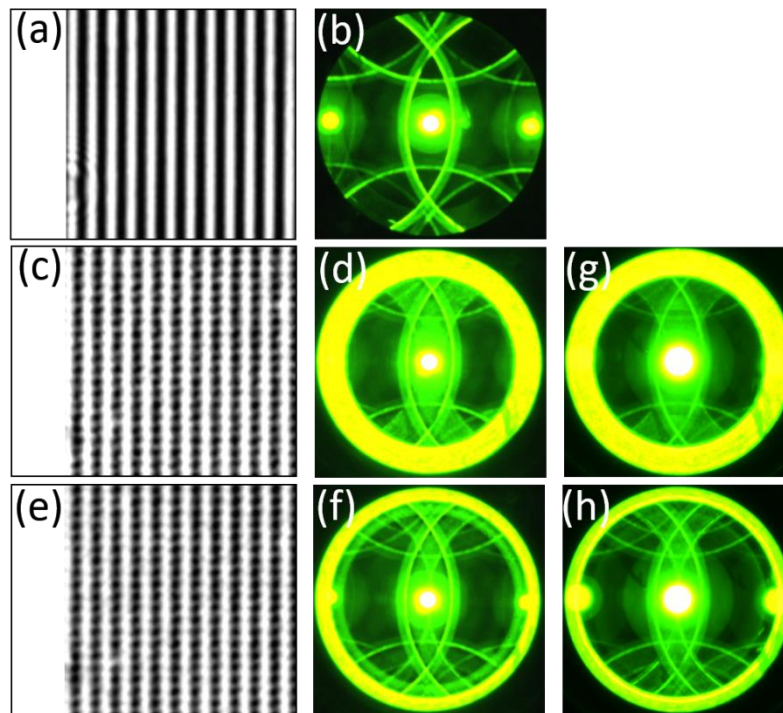


Figure 3.5 Real plane images (a, c, e), and back focal-plane images (b, d, f) are obtained by illuminating chromium pillars structure with the “simplest possible microscope condenser” sketched in Fig. 3.3(h). Images (g-h) are the corresponding back focal-plane images obtained using coverslip-sandwich structure sketched in Fig. 3.3(h). [79]

The real plane images and the back focal-plane images shown in Fig. 3.5 are associated with a two-dimensional periodic crystal of chromium pillars fabricated with rectangular symmetry, with periodicity $p_x=500$ nm along the horizontal axis, and periodicity $p_y=300$ nm along the vertical axis. An oil-immersion objective lens with a numerical aperture of $NA_o=1.3$ was used for observation. The periodicity along the

horizontal axis is larger than the minimum observable periodicity of the objective lens used for observation, and hence, it is always visible in the real plane images and the corresponding back focal-plane of the oil-immersion objective lens. The pair of images shown in Fig. 3.5(a-b) corresponds to the real plane and the back focal-plane images in the “simplest possible condenser” setup. Only the first order circular condenser rings with approximate numerical aperture of $NA_c=1.5$ that are distributed corresponding to vertical periodicity, $p_y=300$ nm, are seen to have been partially captured in the back focal-plane of the oil-immersion objective lens shown in Fig. 3.5(b), in accordance with the Abbe’s theory of image formation, the corresponding periodicity is not visible in the real plane shown in Fig. 3.5(a). However, on depositing a drop of a low boiling point liquid over the “simplest possible condenser” structure, results in the structure shown in Fig. 3.3(h), which can be used to obtain variable numerical aperture condenser rings. The pair of images in Figs are the corresponding real plane and back focal-plane images that were sequentially obtained at a time interval of nearly 6 seconds after depositing a large drop (0.25 ml) of isopropanol over the “simplest possible condenser” structure. This alters the geometry of the top surface, and consequently, the numerical aperture of the circular condenser rings changes from $NA_c=1.04$ in Fig. 3.5(d) to $NA_c=1.12$ in Fig. 3.5(f). In accordance with Abbe’s theory of image formation, as the zeroth order circular condenser ring now appears in the back focal-plane of the oil-immersion objective lens due to change in the geometry of the imaging structure along with the associated first order circular condenser rings that are partially captured ($NA_c < NA_o$), the corresponding real plane image clearly shows the periodicity in the vertical direction.

Likewise, Fig. 3.5(g) shows the image obtained in the back focal-plane of the oil-immersion objective lens when the coverslip-sandwich structure is used for imaging, whereas Fig. 3.5(h) shows an image captured approximately 6 seconds after depositing a drop of isopropanol over the coverslip-sandwich structure, which changes the geometry of the imaging structure to that sketched in Fig. 3.2(c). The real plane images corresponding to the back focal-plane images shown in Figs. 3.5(g) and 3.5(h) are very similar to those shown in Figs. 3.5(d) and 3.5(f), respectively, and hence, are not shown in this work. Even with different geometries, the images captured back

focal-plane of the oil-immersion objective lens when using different imaging structures shown in Figs. 3.2(b), 3.2(c), 3.3(c), and 3.3(h) are very similar. This indicates that these imaging structures are not only efficient condensers, but also suggests that there must be some common physical mechanism that produces circular condenser rings in these imaging structures.

Moreover, this indicates that the geometry of the structure plays an important role in the condenser-like behavior of the structures, which can be investigated further using experimental results shown in Fig. 3.6. A coverslip-sandwich structure shown in Fig. 3.2(c) has a planar geometry, and hence, it cannot alter the direction of the perpendicular illumination to produce the circular condenser rings in the back focal-plane of the oil-immersion objective lens that are observed for this type of structures. Also, the incident illumination is not perfectly perpendicular, but the illumination at slightly inclined angles ($NA_c \sim 0.35$ for the central bright spot) should emerge at the same angle on the other side of the planar geometry. Thus, the perpendicular illumination does directly contribute in formation of the circular condenser rings. Consequently, the light that gets scattered at the top aperture of the oil-immersion objective lens has some contribution in formation of the circular condenser rings. In order to investigate more about the contribution of the light scattered at the top aperture, a specially designed spatial beam-block was introduced in the setup as shown in Fig. 3.6(a) to block the perpendicular illumination from entering the oil-immersion objective lens directly. As observed in Fig. 3.6(b), the circular condenser rings are still formed in the back focal-plane of the oil-immersion objective lens. Also, in accordance with the Abbe's theory of image formation, the corresponding periodicity is observed in the real plane of the experimental setup, as shown in Fig. 3.6(c). Moreover, on comparing the observed intensity of the real plane and back focal-plane images obtained with and without the spatial beam-block that are shown in Figs. 3.6(d-e), it appears that the contrast of the images obtained without the spatial beam-block is relatively poor that the contrast of the images obtained with the spatial beam-block. This again indicates that the perpendicular illumination has no direct contribution in formation of the circular condenser rings, and, instead, the formation of

the circular condenser rings can be attributed to scattering of light that occurs at the top aperture of the oil-immersion objective lens.

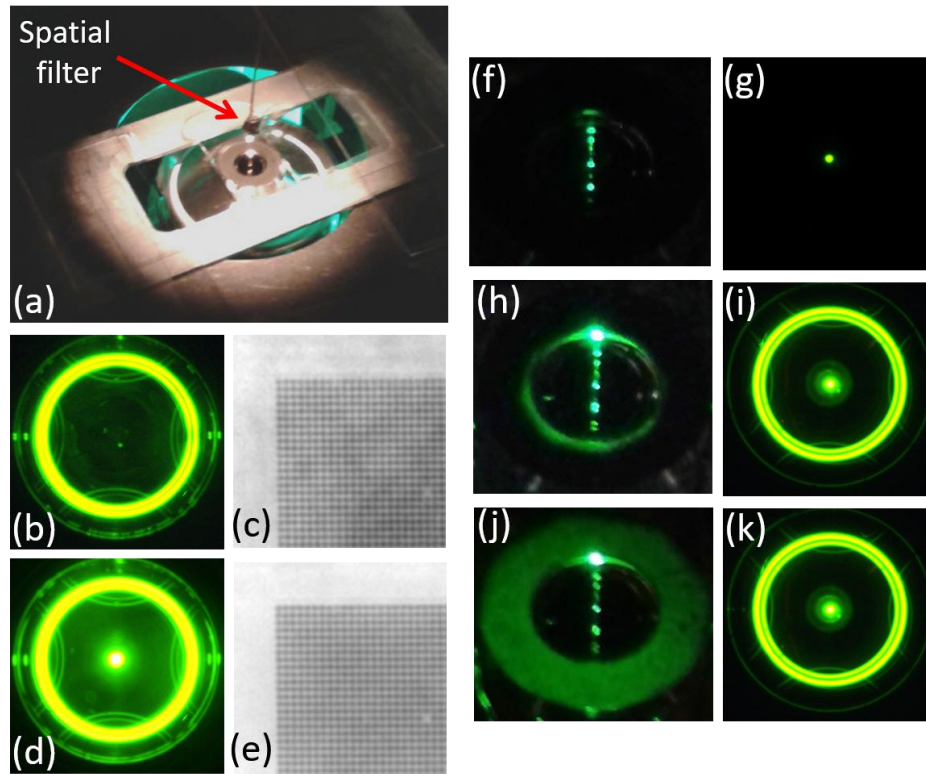


Figure 3.6 Images (b-c) are obtained on putting spatial filter as shown in (a) show better contrast than images (d-e) obtained without spatial filter, using coverslip-sandwich structure. Images (g, i, k) obtained using collimated perpendicular light beam incident on (f, h, j), respectively, indicates that scattering at the inner edge causes formation of circular condenser rings. [78]

This observation can be investigated further to determine if the scattering of light that results in circular condensers rings occurs at the inner edge of the top aperture or at the face of the top aperture of the oil-immersion objective lens. Firstly, a collimated beam of light ($NA_c \sim 0.1$ for the central bright spot corresponding to narrow perpendicularly incident illumination beam in Figs. 3.6(g), 3.6(i), and 3.6(k)) was allowed to enter the oil-immersion objective lens, without letting it fall over the face of the top aperture and the edge of the top aperture of the oil-immersion objective lens, as shown in Fig. 3.6(f). The back focal-plane image obtained this way is shown in Fig. 3.6(g), which does not show any circular condenser rings, and hence, the light that is scattered at the face of the top aperture, or the edge of the top aperture of the oil-immersion objective lens contributes in formation of the circular condenser rings in

the back focal-plane of the oil-immersion lens by illuminating the periodic structure with a solid cone of light. Secondly, the collimated beam is allowed to fall only up to the inner edge of the top aperture of oil-immersion objective lens, as shown in Fig. 3.6(h). Now, the circular condenser rings start appearing in the back focal-plane of the oil-immersion objective lens, as shown in Fig. 3.6(i). Moreover, first order circular diffraction rings are observed as they are partially captured by the oil-immersion objective lens, and are distributed with the symmetry corresponding to the two-dimensional periodic crystal under observation. This indicates that the inner edge of the top aperture of the oil-immersion objective lens contributes in formation of circular condenser rings. Finally, the collimated beam is allowed to fall on the entire top face of the oil-immersion objective lens, as shown in Fig. 3.6(j). The observed intensities in the real plane and the back focal-plane of the oil-immersion objective lens in Fig. 3.6(k) is similar to the observed intensity when the incident collimated beam was allowed to fall only up to the inner edge of the oil-immersion objective lens that is shown in Fig. 3.6(i). This indicates that the light scattered at the top face of the oil-immersion objective lens does not contribute to the formation of circular condenser rings. Consequently, formation of circular condenser rings can be attributed only to the light that gets scattered at the inner edge of the top aperture of the oil-immersion objective lens.

Reconfigurable optical condenser for detection of periodic crystals

The circular condenser rings in the back focal-plane of the oil-immersion objective lens of the coverslip-sandwich structures cannot be observed when dry objective lenses are used. This fact is clearly seen from Figs. 3.7(a) and 3.7(b) that show the real plane and the back focal-plane images of the two-dimensional periodic structures of chromium pillars with periodicity $p=450$ nm that are distributed with square symmetry, which were obtained using a dry objective lens with $NA_o=0.3$. The large squares that appear in the real plane image are the $100 \mu\text{m}^2$ lattices of chromium pillars. This is further corroborated by the back focal-plane image shown in Fig. 3.7(b), which does not have the diffraction features corresponding to the symmetry of the periodic crystals under observation. This indicates that the oil-immersion objective lens has some contribution in formation of the circular condenser rings. The light

scattered at the inner edge of the top aperture of the oil-immersion objective lens would be reflected by the top semi-spherical lens may result in formation of circular condenser rings. In order to investigate the effect of the oil-immersion objective lens, an add-on optical module, which is shown in Figs. 3.1(c) and 3.1(d), and was made by cutting the top part of the oil-immersion objective lens that produces the circular condenser rings.

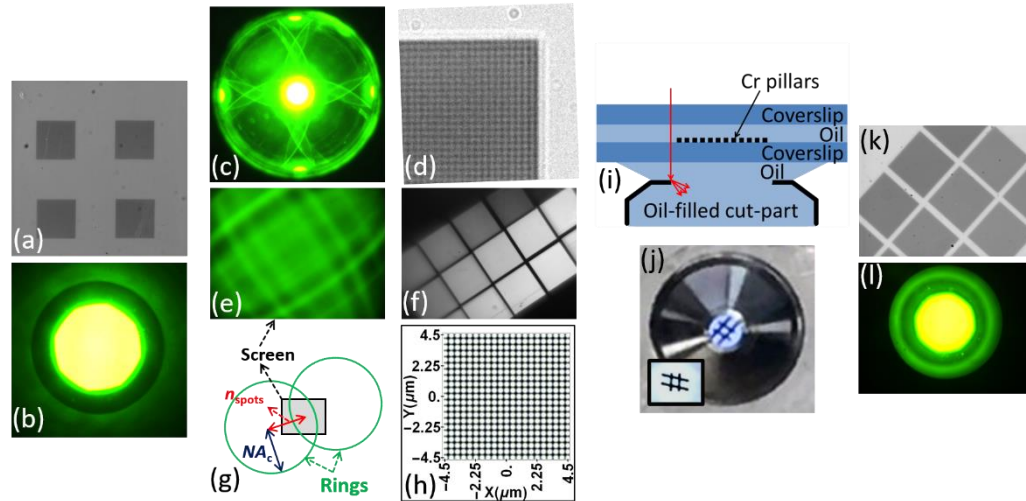


Figure 3.7 Images (a-b) show pair of real plane and back focal-plane images of periodic crystal of chromium pillars obtained using an oil-immersion objective lens, and images (c-d) show a pair of real plane and back focal-plane images obtained from add-on optical module shown in Fig. 3.1(c, d), which was made from the same objective lens. Image (e) shows the procedure to obtain simulated real plane in (f). Images (g-h) show add-on optical module filled with index matching oil, and images (i-j) show the inability of such structure to produce circular condenser rings. [79]

Figs. 3.7(c) and 3.7(d) show the back focal-plane image and the real plane image of a two-dimensional periodic structure of chromium pillars with periodicity $p=450$ nm that are distributed with square symmetry, which were obtained by the oil-immersion lens that was used to make the add-on optical module shown in Fig. 3.1(c) and 3.1(d). Note that for circular condenser rings of numerical aperture 1.50, if the periodicity of the two-dimensional crystal of chromium pillars that is to be observed is $p=450$ nm, the circular condenser rings will pass through the center of the back focal-plane of the objective lens used for observation. This add-on optical module was then put in between the “simplest possible condenser” structure and a dry objective lens with $NA_o=0.08$, as shown in Fig. 3.1(b). Note that in this case, the numerical aperture

of the perpendicular illumination from the microscope's built-in illumination source is larger than the numerical aperture of the objective lens. Consequently, in order to facilitate the direct observation of the circular condenser rings in the back focal-plane of the dry objective lens, a spatial beam-block is put in the back focal-plane of the dry objective lens to remove the bright central spot corresponding to perpendicular illumination. Corresponding back-focal plane image and real plane image of the two-dimensional periodic structures of the chromium pillars distributed in square symmetry with periodicity $p=450$ nm are shown in Figs. 3.7(e) and 3.7(f), respectively. The back focal-plane image of the dry objective lens shown in Fig. 3.7(f) has partially appearing first order diffraction rings that are distributed with the symmetry corresponding to the periodic crystals under observation. However, as the size of the circular condenser rings is much larger in comparison to the numerical aperture of the dry objective lens used for observation, none of the diffraction orders except the first order circular condenser rings are visible in the back focal-plane of the dry objective lens. Consequently, in accordance with the Abbe's theory of image formation [81], the real plane images do not have any information of the periodicity of the object under observation. For the same reason, and as the zeroth order diffraction feature due to perpendicular illumination from microscope's built-in illumination source, this experimental setup is in dark-field configuration. The back focal-plane image of the dry objective lens used for observation can be understood from the schematic diagram of the expected back focal-plane and the actually visible part on the screen shown in Fig. 3.7(i). As mentioned before, the circular condenser rings appearing in the back focal-plane images of the dry objective lens shown in Fig. 3.7(d) correspond to the circular condenser rings of numerical aperture of $NA_c=1.5$ that are visible in "simplest possible condenser" structure sketched in Fig. 3.2(b). Thus, the back focal-plane of the dry objective lens used for observation can be calibrated in terms of the effective refractive index. The average distance between the centers of the partially visible first order diffraction rings from the center of the back focal-plane was determined to be $\Delta n_{spots} \sim 1.28$, which corresponds to a periodicity of $\Delta K=14.10 \mu\text{m}^{-1}$ in the back focal-plane of the dry objective lens that is used for observation. Consequently, the periodicity in the real plane is determined to be 446 nm, which is

within 1% variation from the actual periodicity of the object under observation. Using periodicity of the back focal-plane images, the real plane image can be simulated by taking a two-dimensional Fast Fourier Transform algorithm of the extended back focal-plane image created using centers of the circular condenser rings using Wolfram Mathematica software, which appears to be as shown in Fig. 3.7(h). For a dry objective lens with $NA_o=0.08$, the Rayleigh resolution limit is approximately $3.6 \mu\text{m}$. Consequently, optical detection of the two-dimensional periodic structure of chromium pillars that are distributed in square symmetry with periodicity of $p=450 \text{ nm}$ with a simultaneously large field-of-view indicates true sub-wavelength capability when add-on optical module is used for imaging. Note that the add-on optical module is much lighter than the traditional design of optical condensers [82]. Thus, the coverslip-sandwich structure along with the oil-immersion objective lens used for observation (or the add-on optical module discussed in this section) constitutes an optical condenser that could be used to optically detect the two-dimensional periodic structures with periodicities that are up to approximately eight times smaller than the Abbe's resolution limit. In other words, the circular condenser rings in such structures are formed as the light that gets scattered at the inner edge of the top aperture of the oil-immersion objective lens (or the add-on optical module discussed in this section), and then gets reflected back to the object under observation from the curved surface of the top semi-spherical lens of the oil-immersion objective lens used for observation (or the add-on optical module discussed in this section). This observation also indicates that the top semi-spherical lens of the oil-immersion objective lens that is used for imaging contributes in formation of circular condenser rings. This can be further confirmed with the structure that is schematically shown in Fig. 3.7(g). The add-on optical module discussed in this section was filled with index-matching oil from the inside, and then, it was sealed from the back using a glass coverslip, which is shown in Fig. 3.7(h). Consequently, the curved interface formed by the top semi-spherical lens with the air is removed, and instead, a planar interface is created by the glass interface, which is not expected to modify the incident perpendicular illumination to produce circular condenser rings due to inclined illumination in the back focal-plane of the dry objective lens used for observation. This is corroborated by the unmagnified

appearance of the symbol ‘#’ through the add-on optical module, which is comparable to inset image of the symbol in Fig. 3.7(h). Now, this modified add-on optical module is kept in experimental setup sketched in Fig. 3.1(b) to observe the two-dimensional periodic crystal of chromium pillars with periodicity $p=450$ nm that are distributed with square symmetry with the help of a coverslip-sandwich structure. Corresponding real plane and back focal-plane images are shown in Figs. 3.7(k) and 3.7(l), respectively. Note that the circular condenser rings that should appear near the center of the back focal-plane of the dry objective lens used for observation are now absent. Also, the real plane image consists only of the large featureless square lattices of $100 \mu\text{m}^2$ area. This again confirms that the top semi-spherical lens contributes in formation of the circular condenser rings.

In order to investigate the utility of the add-on optical module as a reconfigurable optical condenser, a large drop of low boiling point liquid (isopropanol) was deposited over the coverslip-sandwich structure, and a sequence of images were captured in the back focal-plane of the dry objective lens (with $NA_o=0.3$) at a time interval of approximately 5 seconds. As the drop of isopropanol evaporates, the circular condenser rings change in size, indicating that the add-on optical module performs similar to the top semi-spherical lens of the oil-immersion objective lens that can be used to create circular condenser rings. The corresponding time evolution of the numerical aperture of the circular condenser rings is shown for coverslip-sandwich structure in Fig. 3.8, and for the “simplest possible condenser” structure in Fig. 3.2(b). In accordance with the performance of the “simplest possible condenser” structure, fraction of the first order circular condenser rings with approximate numerical aperture of 1.50 are observed in the outermost side of the back focal-plane images in all images shown in Fig. 3.8. As the drop of isopropanol evaporates, the numerical aperture of the circular condenser rings formed in the coverslip-sandwich structure is found to change from $1.36 \rightarrow 1.40 \rightarrow 1.44$, and the circular condenser rings formed in the “simplest possible condenser” structure changes from $1.37 \rightarrow 1.41 \rightarrow 1.45$. For both these structures, along with the fraction of the first order circular condenser rings that appear in the back focal-plane of the dry objective lens used for observation, a small, bright, circular condenser ring is also observed, whose numerical aperture progressively

changes from $0.60 \rightarrow 0.66 \rightarrow 0.72 \rightarrow 0.78$ for the coverslip-sandwich structure, and from $0.79 \rightarrow 0.83 \rightarrow 0.87 \rightarrow 0.94$ for the “simplest possible condenser” structure. This clearly demonstrates the utility of the add-on optical module for optical detection of two-dimensional periodic crystals.

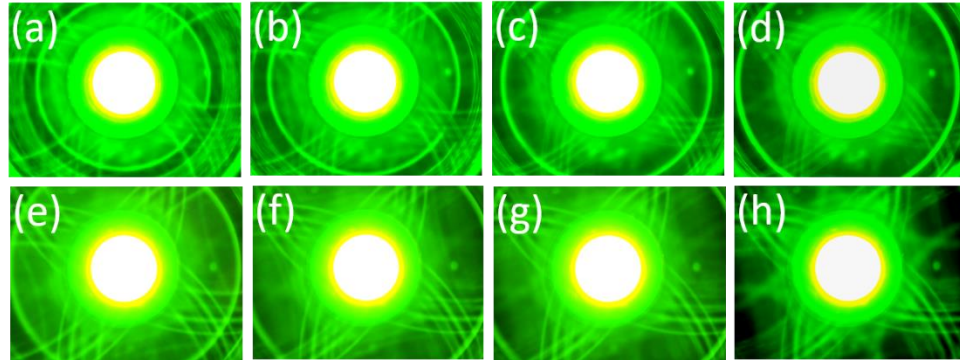


Figure 3.8 Images shown in (a-d) are the back focal-plane images of the sample structure in Fig. 3.3(h), and images shown in (e-h) are the back focal-plane images of the sample structure in Fig. 3.3(c). [79]

Clearly, when using the coverslip-sandwich structure, the circular condenser rings that are formed in the back focal-plane of the oil-immersion objective lens are much brighter with respect to the background illumination. This indicates that some type of cavity-based resonance phenomenon occurring at particular angles is involved in formation of the circular condenser rings. To investigate the role of cavity-based resonance in formation of circular condenser rings, ray-optics simulations of the structures were conducted using Comsol Multiphysics software, for the structure shown in Fig. 3.9(a), where a glass coverslip is placed over the add-on optical module discussed in this section using a refractive index-matching oil layer in between. The add-on optical module used for simulation consists of a perfectly semi-spherical lens of 3 mm radius that is held with the help of a 1 mm thick metal-casing (that also mimics the metal structure of the oil-immersion objective lens used for observation). The glass coverslip substrate used for simulations is considered to be $150 \mu\text{m}$ thick, and the thickness of the oil layer is considered to be 1.4 mm. In subsequent figures, the path traversed by the light in the entire structure is revealed, where the color of the ray at a particular location in the structure denotes the corresponding optical path-length. It is assumed that the perpendicular illumination from the microscope’s built-in source

gets scattered at point A, and hence, for simulation, rays emanating from point A that are travelling in different directions are considered.

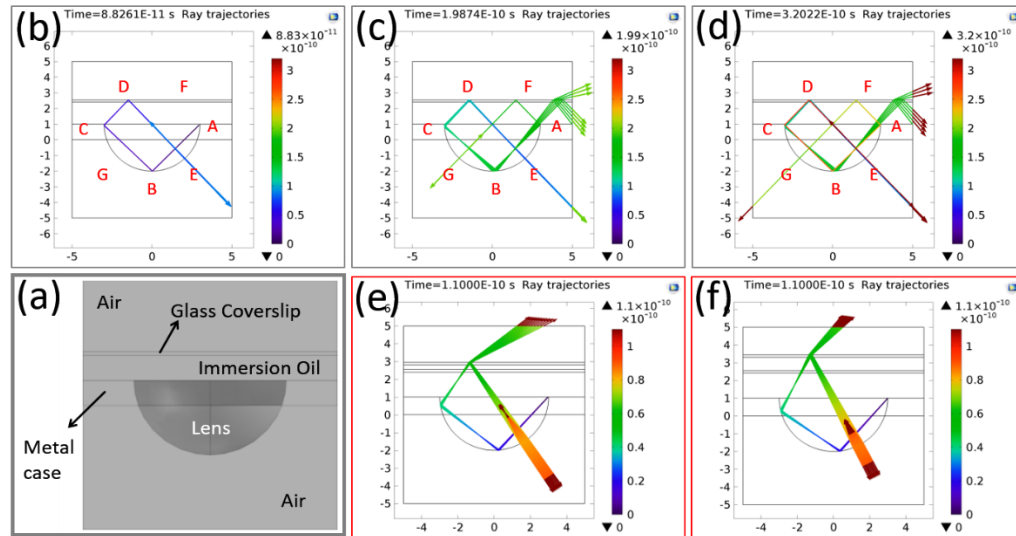


Figure 3.9 Ray-optics simulations that demonstrate that the efficiency of the “simplest microscope condenser structure” and coverslip-sandwich condenser structure can be attributed to cavity-based resonance. [79]

For the case shown in Figs. 3.9(b), 3.9(c), and 3.9(d), the light ray emanating from point A at a certain angle gets reflected at B, C, and then D to reach point E on the semi-spherical lens. After specularly reflecting from the curved surface at point E, the light traverses further along E-D-C-B-A-F-G in a similar manner to form an optical cavity. Note that the light is totally-internally reflected at points D and F at the top surface of the glass coverslip that is used to hold the object under observation. This causes the object to be illuminated using evanescent surface waves associated with total internal reflection, and then leaks into the glass coverslip substrate so that the information in the near-field region is transported to the far-field region. This also explains why the numerical aperture of the circular condenser rings in the “simplest possible condenser” structure always appears to be approximately 1.50. Similar type of optical cavity formation can be observed for coverslip-sandwich structures with two glass coverslips shown in Figs. 3.9(e) and 3.9(f). In this case, the light that is reflected back from the top surface of the upper glass coverslip may provide inclined illumination to the object under observation placed on the bottom coverslip. Also, on comparing Figs. 3.9(e) and 3.9(f), it is clear that on changing the thickness of the oil

layer in the structure the angle of inclination of the light reflected from the top surface of the upper glass coverslip changes, which explains corresponding variation in the condenser numerical aperture.

CHAPTER 4

FOURIER PTYCHOGRAPHIC MICROSCOPY USING HEMISPHERICAL DIGITAL CONDENSERS

Most of the conventional non-interferometric wide-field imaging techniques rely on tweaking the imaging setup in order to achieve better performance. One of the important parameters to quantify the performance of the imaging setups is the space-bandwidth product that can be obtained in its output, which can be found by multiplying the field-of-view with the spatial resolution of the imaging setup [83]. The space-bandwidth product can be physically interpreted as the total number of pixels on the imaging-sensor (usually a CCD camera) required for imaging the area at best possible resolution. For example, when imaging using a dry objective lens from Nikon with 10 \times magnification and numerical aperture of $NA_o=0.3$ and a 570 nm wavelength illumination, it would need an imaging-sensor with 100 million pixels to capture all the information produced by the imaging setup, and consequently, the imaging-sensor operating at 10 Hz should be capable to collect the output data at the rate of approximately 3 billion bytes per second. Another consequence of this is that the size of a pixel on the imaging-sensor is requires to be 6.25 μm^2 (or smaller) to resolve the features in the experimentally acquired images. Clearly, for current levels of technology, all three requirements - the total number of pixels, the size of each pixel, and the data-transfer rate, are very challenging to achieve. In other words, the amount of information generated by the imaging setup with low numerical aperture objective lenses may not be fully utilized due to current technological limitations. Numerical processing techniques can be relatively easily employed to achieve relatively better performance for such imaging setups. Fourier Ptychographic Microscopy (FPM) technique, which is discussed in this chapter, is a recently proposed technique that promises achieve high values of space-bandwidth product of the reconstructed image to obtain better performance from an imaging setup [83]. A series of experimental and computational simulations are discussed in this chapter to reveal the resolution limit when FPM technique is employed with the aim to achieve enhanced lateral resolution.

In the next section, the experimental setup for implementing the FPM technique is discussed.

Experimental Setup

Before discussing the experimental setup for FPM technique that is shown in Fig. 4.1(a), the illumination source that is used for this purpose deserves some explanation.

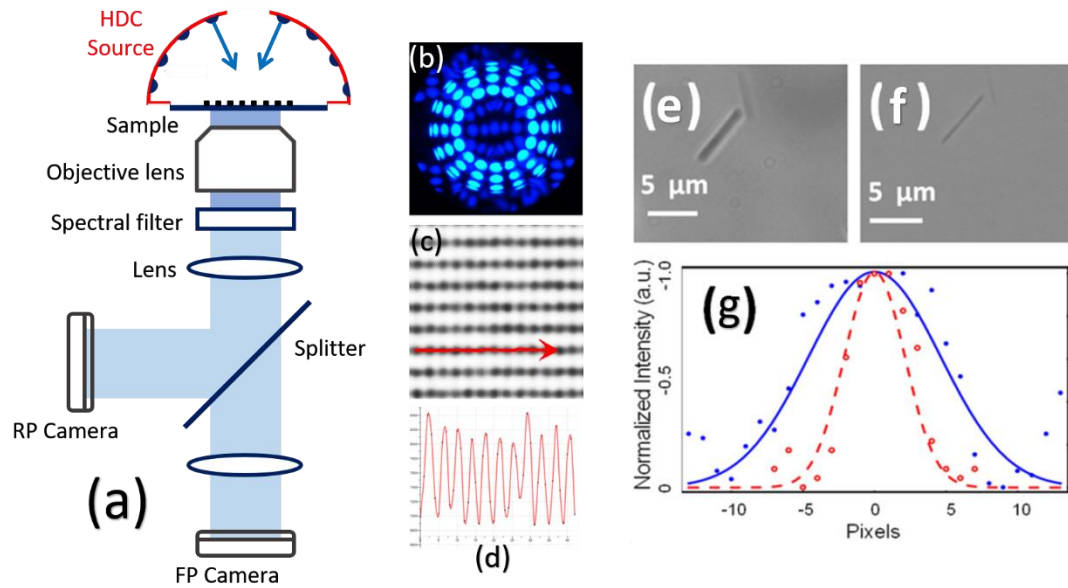


Figure 4.1 Image (a) shows experimental setup with HDC sources. Images (b-d) show the images acquired for chromium pillars structure using setup shown in image (a). Images (e-f) show images of nanowires using (e) perpendicularly incident white light, and (f) HDC source. Intensity profiles of nanowire in images (e-f) clearly indicates resolution enhancement. [84]

The digitally controlled illumination source used for experimentally implementing FPM technique in this chapter is a Hemispherical Digital Condenser (HDC), which is a semi-spherical dome with 64 light-emitting diodes (LEDs) that are distributed in four circular rows on the inner surface of the dome, as shown as “HDC Source” in Fig. 4.1(a). Each of these LEDs can be turned ON and OFF independently of the state of other LEDs on the HDC. The numerical aperture of every LED in the four rows of the HDC is set to $NA_c=0.58, 0.73, 0.87,$ and 0.97 . The digitally controlled HDC has to be centered at the region of interest on the object under observation, which can be verified from the back focal plane of the objective lens used for

observation. A commercially available inverted Nikon Ti-Eclipse microscope can be used in conjunction with the digitally controlled HDC, whose schematically diagram is sketched in Fig. 4.1(a). The light from the digitally controlled HDC illuminates the object under observation, and the corresponding transmitted light is collected using an objective lens. The illumination from the digitally controlled HDC that is used in experiments discussed in this chapter has a peak at approximately 450 nm wavelength. However, for better performance, a spectral band-pass filter at the same wavelength and a spectral bandwidth of 10 nm is inserted below the objective lens. The light transmitted by the object is imaged at the real plane and Fourier plane of the objective lens using internal lenses of the microscope. The HDCs are well-known to implement wide-field non-scanning imaging without any sort of special sample preparation. The enhancement in lateral resolution that is achieved using the digitally controlled HDC can be attributed to inclined illumination from the LEDs.

Fig. 4.1(b) shows the back focal-plane of the objective lens when all LEDs of the HDC source are illuminating a two-dimensional periodic crystal of chromium pillars that are distributed in rectangular symmetry with periodicities $p_x=300$ nm and $p_y=500$ nm in mutually perpendicular directions, and the light transmitted by the periodic crystal is collected by an oil-immersion objective lens with numerical aperture $NA_o=0.8$. The brighter spots in Fig. 4.1(b) correspond to the zero order diffraction spots associated with the illumination from the LEDs of the digitally controlled HDC, whereas the other spots correspond to the diffracted light captured by the objective lens. Consequently, in accordance with the Abbe's theory of image formation, the periodicities in both directions are visible in the corresponding real plane image shown in Fig. 4.1(c), and the graph shown in Fig. 4.1(d) corresponds to the spatial intensity along the red arrow shown in Fig. 4.1(c). As the vertical periodicity (300 nm) of the object under observation is less than the Rayleigh resolution limit for the setup (~ 346 nm), this observation demonstrates the sub-wavelength resolution capability of the HDCs.

HDCs can also be used to image non-periodic samples. Although the images shown in Figs. 4.1(d), and 4.1(e) are not from a HDC that cannot be digitally controlled [84], they exemplify the performance of the HDCs. Approximately 150 nm

thick TiO₂-B nanowires were spin-coated over a glass coverslip, and were imaged using experimental setup shown in Fig. 4.1(a), which consists of an oil-immersion objective lens with numerical aperture $NA_o=1.49$. The image of nanowires that is captured using microscope's built-in white light illumination source emitting light that falls perpendicularly over the object under observation is shown in Fig. 4.1(e), whereas the image of the same region of interest on the object under observation that is captured using HDC is shown in Fig. 4.1(f). The transversal intensity profile of these images of the nanowires shown in Fig. 4.1(g) clearly shows that the lateral resolution achieved using HDC is much better in comparison to that from the microscope's built-in white light illumination source. Note that the experimental data is represented with dots and circles, whereas the red and blue curves indicate the Gaussian fits applied to the experimentally acquired data. The corresponding full width at half maximum (FWHM) of the transversal intensity profile of the nanowire when microscope's built-in white light illumination source is used is determined to be approximately 12 pixels, whereas FWHM when the HDC is used is determined to be approximately 7 pixels, which suggests that the lateral resolution when using HDC has enhanced by approximately 1.7 times.

Note that the equation governing resolution limit can be expressed in terms of minimum observable periodicity of a two-dimensional periodic crystal [84], as shown below, where λ is the illumination wavelength, and $n_{superstrate}$ and $n_{substrate}$ are the refractive indices of the superstrate and substrate layers of the imaging structure, respectively:

$$p_{min} = \frac{\lambda}{n_{superstrate} + n_{substrate}} \quad (4.1)$$

Although HDCs that cannot be digitally controlled for turning off every LED ON and OFF independently can be used for obtaining enhanced lateral resolution, an important parameter, phase of the light transmitted through the object under observation, is never acquired in this type of setups. FPM technique, on the other hand, can be used to obtain this unrecovered phase when used in conjunction with the

digitally controllable HDCs. In the next section, basic working mechanism of the FPM technique is discussed.

FPM image reconstruction algorithm

The FPM technique appears to have been inspired from the well-known Ptychography microscopy (PM) technique [86-88], which was proposed to obtain reconstructed images from a collection of the experimentally acquired far-field diffraction patterns of two-dimensional periodic crystals obtained using transmission electron microscopy (without using lenses), by iteratively solving for an estimate of the intensity and phase of the waves exiting the object under observation which is consistent with the obtained intensity measurements. The FPM technique is based on similar strategy, but unlike PM technique, the object support constraints are applied in the Fourier domain. FPM technique uses low resolution real plane intensity images that are experimentally acquired at different angles of illumination to systematically “stitch” a large synthetic numerical aperture in the Fourier space to obtain a reconstructed real space image with enhanced resolution, while simultaneously retrieving the unmeasured phase of the light that is transmitted through the object under observation.

The phase-retrieval algorithm that is employed for the work shown in this chapter is the well-known Gerchberg-Saxton algorithm, which has been used by research groups that has invented the FPM technique [83, 89]. The passband of the objective lens used for experimental data acquisition and the amplitude of the acquired low resolution real plane images function as the support constraints in the FPM image reconstruction algorithm. Note that, unlike PM technique, the FPM technique does not require scanning the object under observation with a narrow collimated beam. Also, when using digitally controlled HDC for implementing the FPM technique, the uniformity of illumination is better than that when using a planar array of LEDs. Due to the reciprocity principle of Optics, FPM and PM appear to be alternative but equivalent phase-recovery imaging methods [86, 90].

The FPM technique uses a set of low resolution real plane intensity images acquired by using the digitally controlled HDC in the experimental setup shown in

Fig. 4.1(a), and these images are then processed using the FPM image reconstruction algorithm. Each low resolution real plane image contains some “information” about the finally reconstructed image, which has to be systematically added to the reconstructed image. The FPM image reconstruction algorithm begins by assuming that the intensity and the phase of the light transmitted through the object under observation is uniformly one and zero, respectively, whose corresponding Fourier space would be as shown in the equation below (in the beginning, $v = 0$):

$$Z_0 = A(\vec{k})e^{i\varphi(\vec{k})} = \mathcal{F}[a(\vec{r})e^{i\psi(\vec{r})}] \quad (4.2)$$

A low-pass filter corresponding to the numerical aperture of the objective lens used for experimental data acquisition (W) is applied to the reconstructed image, after the image is shifted towards the center of the Fourier plane by the amount corresponding to the wave-vector of the illuminating LED (\vec{k}_j), as shown in the equation below:

$$B(\vec{k})e^{i\phi(\vec{k})} = W \cdot [A(\vec{k} - \vec{k}_j)e^{i\varphi(\vec{k} - \vec{k}_j)}] \quad (4.3)$$

Using two-dimensional Fast Fourier Transform (FFT) function, the amplitude in the corresponding low resolution real plane image is replaced by the amplitude of the experimentally acquired image to add the experimentally acquired “information”, as shown in the equations below:

$$b(\vec{r})e^{i\chi(\vec{r})} = \mathcal{F}^{-1} [B(\vec{k})e^{i\phi(\vec{k})}] \quad (4.4)$$

$$b(\vec{r})e^{i\chi(\vec{r})} \xrightarrow{\text{Replace amplitude}} b_{exp}(\vec{r})e^{i\chi(\vec{r})} \quad (4.5)$$

Then, the data is transformed back to the Fourier plane using two-dimensional inverse FFT function, and is low-pass filtered to only include the amount that can be captured by objective lens, and then shifted back to the location corresponding to the location of the wave-vector of the illuminating LED, as shown in the equations below:

$$c(\vec{k})e^{i\psi(\vec{k})} = \mathcal{F}[b_{exp}(\vec{r})e^{i\chi(\vec{r})}] \quad (4.6)$$

$$D(\vec{k})e^{i\theta(\vec{k})} = W \cdot [c(\vec{k} + \vec{k}_j)e^{i\psi(\vec{k} + \vec{k}_j)}] \quad (4.7)$$

The information already present in the Fourier space that is being reconstructed is given by the following equation, which can be derived from equation (4.3):

$$E(\vec{k})e^{i\theta(\vec{k})} = B(\vec{k} + \vec{k}_j)e^{i\phi(\vec{k} + \vec{k}_j)} \quad (4.8)$$

Hence, the “new information” from the updated data is added to the reconstructed Fourier plane image as shown in the equation below:

$$Z = Z_0 + \beta \cdot [D(\vec{k})e^{i\theta(\vec{k})} - E(\vec{k})e^{i\theta(\vec{k})}] \quad (4.9)$$

In the above equation, β is an image update parameter that can be adjusted between 0 and 1 for finer image reconstruction. Finally, after updating the reconstructed Fourier plane image, the reconstructed real plane intensity and corresponding phase are obtained using two-dimensional FFT function. Note that for subsequent low resolution real plane image to be processed, the new $Z_0 = Z$. These steps are repeated until all the experimentally acquired “information” in the low resolution real plane images is systematically added to the reconstructed image, which constitutes a single iteration of the FPM algorithm. The FPM algorithm is expected to converge after several iterations.

Computational simulations can also be used to understand the performance of the FPM technique. If all the light transmitted through a two-dimensional periodic crystal is collected by an objective lens, the back focal-plane of the objective lens would have all possible diffraction orders. This corresponds to an infinite resolution, such that the real space is a perfectly resolved two-dimensional periodic crystal appearing as a spatial sequence of zeros at the location of chromium pillars and ones elsewhere. Such spatial sequence can be treated as the object under observation, and the FFT of this spatial sequence corresponds to the back focal-plane image acquired by an imaging setup with infinite resolution. Then, the low resolution real plane images used in the FPM image reconstruction algorithm can be created by simulating experimental data-acquisition process. An actual objective lens can capture only a limited angular range of the light transmitted from the periodic object. Consequently, to mimic the actual experimental data-acquisition process, the diffraction orders that cannot be captured by the objective lens should be removed from the Fourier space by

applying an appropriate low-pass filter (W), and then obtaining the corresponding low resolution real space by using the inverse FFT function. Note that in order to facilitate the understanding of the working of the FPM technique, the simulations shown here are for a one-dimensional periodic crystal, and the corresponding intensity and phase in the Fourier space is shown in terms of the numerical aperture units, which can be determined by dividing the wave-vector by $\left(2\pi/\lambda\right)$.

Performance of the FPM image reconstruction algorithm

Figs. 4.2(a-b) shows the amplitude and phase of the light transmitted by the hypothetical one-dimensional object under observation, whose periodicity is $p=500$ nm, and Figs. 4.2(c-d) shows the corresponding amplitude and phase in the Fourier space, where the spikes correspond to diffraction peaks are located at $NA=0.9$ that is associated with the periodicity in the real space. Note that, as in the actual experimental data-acquisition, the object is sequentially illuminated at 450 nm wavelength, which provides inclined illumination along the values of the wave-vectors (of the LEDs in the digitally controlled HDC) that are represented by corresponding numerical aperture values by red spots on the horizontal axis in Fig. 4.2(c), and its inset image. The intensity and phase in the Fourier space that corresponds to the experimentally acquired low resolution real plane intensity is obtained as described above, and is shown in Figs. 4.2(e) and 4.2(f), for $NA_c=0.58$ illumination corresponding to the first circular row of the LEDs in the digitally controlled HDC, and observation using an objective lens with $NA_o=1.3$.

Corresponding simulated low resolution real space intensity and phase can be obtained using FFT function of the complex Fourier space, and are shown in Figs. 4.2(g) and 4.2(h). In accordance with Abbe's theory of image formation, the simulated low resolution real space intensity has the expected periodicity, as two consecutive diffraction orders appear in the corresponding Fourier space. Note that the shape of peaks appearing in the simulated low resolution real space intensity is different from the light that is considered to be transmitted through the object under observation (shown in Fig. 4.2(a)), as only two diffraction orders appear in the corresponding Fourier space because of limited angular-acquisition of light by objective lens.

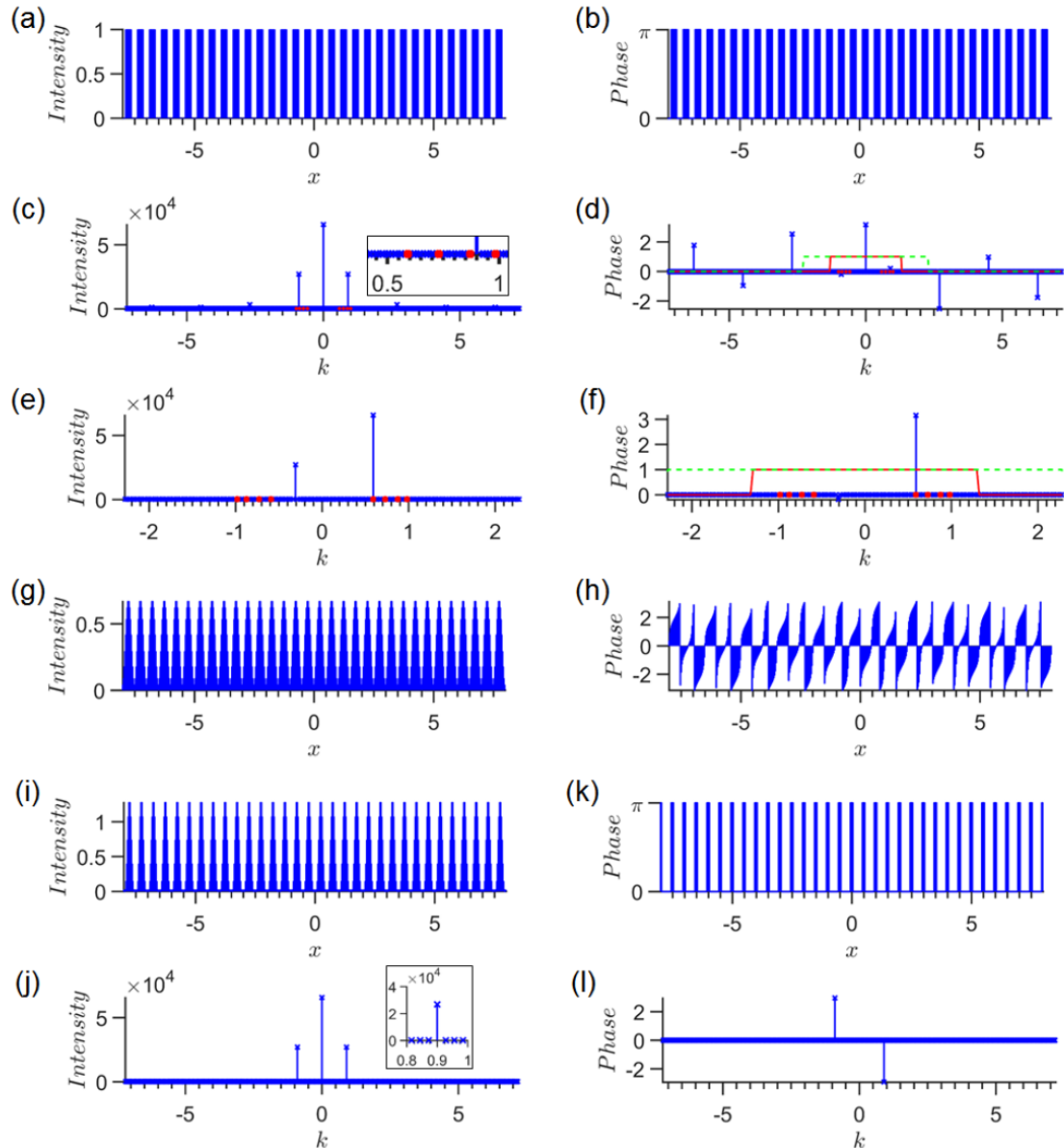


Figure 4.2 FPM image reconstruction process. Images (a-d) show the simulated real space and Fourier space intensity and phase corresponding to periodicity $p=500$ nm. Images (e-h) show process to obtain low resolution real space intensity, and corresponding phase. Images (i-l) show results of FPM reconstruction. [95]

The reconstructed real space and Fourier space obtained by processing all the low resolution real space intensity is shown in Fig. 4.2(i) and 4.2(j). As expected, the periodicity of the crystal is resolved in the reconstructed real space, and the corresponding diffraction peaks are visible in the Fourier space at $NA=0.9$, which indicates that the FPM algorithm has worked correctly.

Moreover, the phase of the real space and Fourier space obtained from the FPM image reconstruction algorithm is shown in Fig. 4.2(k) and 4.2(l). Note that although the FPM image reconstruction algorithm is known to converge very rapidly, all the one-dimensional simulation results shown in this chapter are explored up to 600 iterations to ensure that important developments do not go unobserved. Moreover, the spatial overlap between consecutive updates in the reconstructed Fourier space was determined to be 91% for $NA_o=0.8$ and 94% for $NA_o=1.3$, which is an important parameter associated with convergence of the FPM image reconstruction algorithm [91-92].

The working of FPM image reconstruction algorithm can also be verified using actual experimental data, as shown in Fig. 4.3, which shows the images associated with FPM image reconstruction algorithm that is conducted by processing the actually obtained experimental data for a periodic crystal of chromium pillars distributed in rectangular symmetry with $p_x=300$ nm and $p_y=500$ nm in mutually perpendicular in-plane directions, which were observed with an oil-immersion objective lens with $NA_o=1.3$. The experimental low resolution real plane image and back focal-plane image acquired using illumination corresponding to the first circular row of the LEDs in the digitally controlled HDC ($NA_c=0.58$) are shown in Figs. 4.3(a) and 4.3(b) respectively. Note that along with the brightest zero-order diffraction spot corresponding to the illuminating LED, higher order diffraction spots corresponding to both the periodicities are present in the Fourier plane image, and hence, corresponding periodicities are visible in the real plane image, in accordance with Abbe's theory of image formation. As expected, the reconstructed real plane and Fourier plane images that are shown in Fig. 4.3(c) and 4.3(d), which were obtained by processing all the experimentally acquired low resolution real plane images, have all the information about the periodicity of the two-dimensional periodic crystal. Also, as FPM technique is a phase-retrieval technique, the phase in the real plane is shown in Fig. 4.3(e). Experimental results are not only in excellent agreement with the simulational results, but also demonstrate that the FPM image reconstruction algorithm works for actual real-world objects.

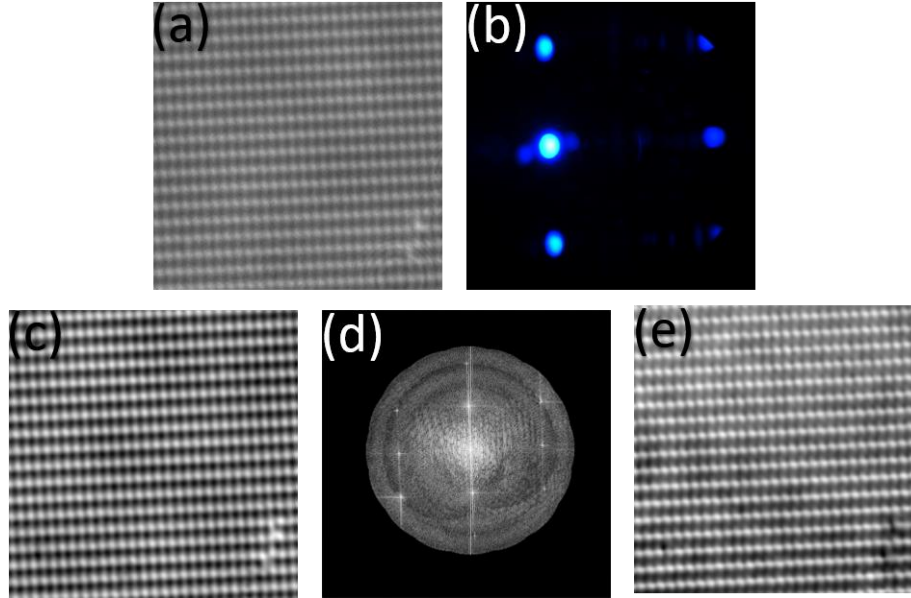


Figure 4.3 Images (a-b) show experimentally acquired low resolution images of chromium pillars structure with periodicities of 300 nm and 500 nm in mutually perpendicular directions with $NA_o=1.3$. Images (c-e) show the real plane, Fourier plane, and real plane phase obtained after FPM image reconstruction. [100]

In order to investigate the FPM image reconstruction algorithm further, we used the two-dimensional periodic crystal of chromium pillars that are distributed in rectangular symmetry with periodicity $p_x=300$ nm and $p_y=500$ nm in mutually perpendicular in-plane directions, and observed it using a dry objective lens with $NA_o=0.8$. Figs. 4.4(a-b) and 4.4(c-d) show the pairs of experimentally acquired low resolution real plane and Fourier plane images obtained using LED corresponding to $NA_c=0.58$ and $NA_c=0.73$, respectively. Figs. 4.4(e) and 4.4(f) show the pair of real plane image and Fourier plane image that were reconstructed using the FPM image reconstruction algorithm using only first two circular rows of the digitally controlled HDC. As some of the low resolution real plane images obtained with LEDs in the first two rows have the information about the horizontal or vertical periodicities of the two-dimensional crystal, the finally reconstructed real plane and Fourier plane images clearly reveal the periodicities.

On the other hand, Figs. 4.4(g) and 4.4(h) are the pair of experimentally acquired low resolution real plane and Fourier plane images obtained using LED corresponding to $NA_c=0.97$. Figs. 4.4(i) and 4.4(j) are the pair of real plane image and

Fourier plane image that were reconstructed using the FPM image reconstruction algorithm using only first two circular rows of the digitally controlled HDC. Fig. 4.4(i) shows the magnified image for the region in Fig. 4.4(k) that is marked by a red square. As none of the low resolution real plane images obtained with LEDs in the last two rows have any information about the horizontal or vertical periodicities of the two-dimensional crystal, the finally reconstructed real plane and Fourier plane images clearly reveal the periodicities.

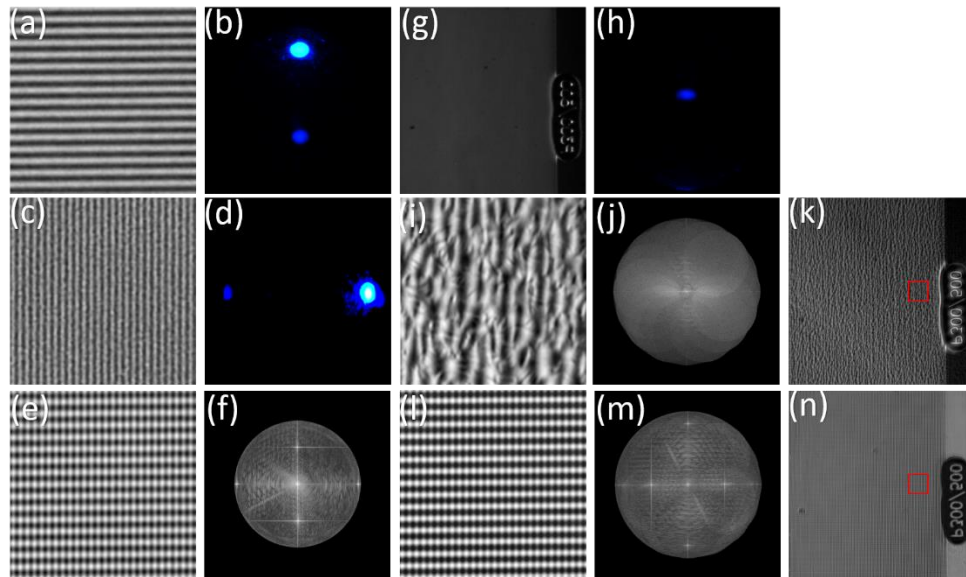


Figure 4.4 Images (a-b) and (c-d) are the pairs of real plane and Fourier plane obtained using $NA_c=0.58$ and 0.73 , respectively, and images (e-f) are corresponding FPM reconstructed images. Images (g-h) is the pair of real plane and Fourier plane images obtained using $NA_c=0.97$. Images (i-j) and (l-m) are FPM reconstructed images, which are obtained using $NA_c=0.87$ and 0.97 , and all low resolution real plane images, respectively. Images (j) and (l) show the region of interest corresponding to area marked with red square in images (k) and (n). [100]

This confirms that when none of the low resolution real plane images have any information about a certain periodicity of the object under observation, the finally reconstructed image does not have that information either. Lastly, Figs 4.4(l) and 4.4(m) show a pair of real plane image and Fourier plane image reconstructed using all experimentally acquired low resolution real plane images, which clearly reveal the periodicities of the two-dimensional periodic crystal as the information is contained in the low resolution real plane images acquired with LEDs from the first two rows of the digitally controlled HDC. Fig. 4.4(l) shows the magnified image for the region in Fig.

4.4(n) that is marked by a red square. This reconfirms that if the information of the periodicity of the two-dimensional crystals is contained in some of the images, then the corresponding periodicity is revealed in the images that are finally reconstructed using the FPM image reconstruction algorithm.

The experimentally demonstrated of the inability of the FPM image reconstruction algorithm to reveal the $p_y=500$ nm periodicity as discussed above is also corroborated by computational simulations. Low resolution real space intensity and corresponding Fourier space intensity was obtained from simulating the light that gets transmitted by a hypothetical one-dimensional periodic crystal with periodicity $p=500$ nm when it is illuminated using LEDs in third and fourth rows of the digitally controlled HDC corresponding to numerical aperture of $NA_c=0.87$ and $NA_c=0.97$, respectively, and then gets captured by a dry objective lens with $NA_o=0.8$. Figs. 4.5(a) and 4.5(b) are the pair of reconstructed real plane intensity and Fourier space intensity obtained using the last two rows of the digitally controlled HDC.

Note that although the real space intensity is periodic, the periodicity that is determined from the corresponding Fourier space intensity shown in Fig. 4.5(b) indicates that the observed periodicity in the reconstructed intensity corresponds to $NA=0.87$ (which corresponds to incorrect real space periodicity $p=517$ nm), which is the numerical aperture of the illumination from the LED in the third circular row of the digitally controlled HDC. This indicates that when the entire set of low resolution real space intensity that is processed using FPM image reconstruction algorithm does not have any information about the periodicity of the object under observation, and the incorrect periodicity appearing in the reconstructed intensity can be attributed to the illumination from the LEDs in the digitally controlled HDC. Also, this observation deserves some explanation regarding the achievable resolution for different rows of LEDs in the digitally controlled HDC. Note that the expected resolution limit when LED in the third row of the digitally controlled HDC corresponding to $NA_c=0.87$ and an objective lens with $NA_o=0.8$ would be $p_{min}=271$ nm. However, as seen in the discussion above, $p=500$ nm $>$ $p_{min}=271$ nm is not revealed after the FPM image reconstruction with $NA_c=0.87$ and $NA_c=0.97$.

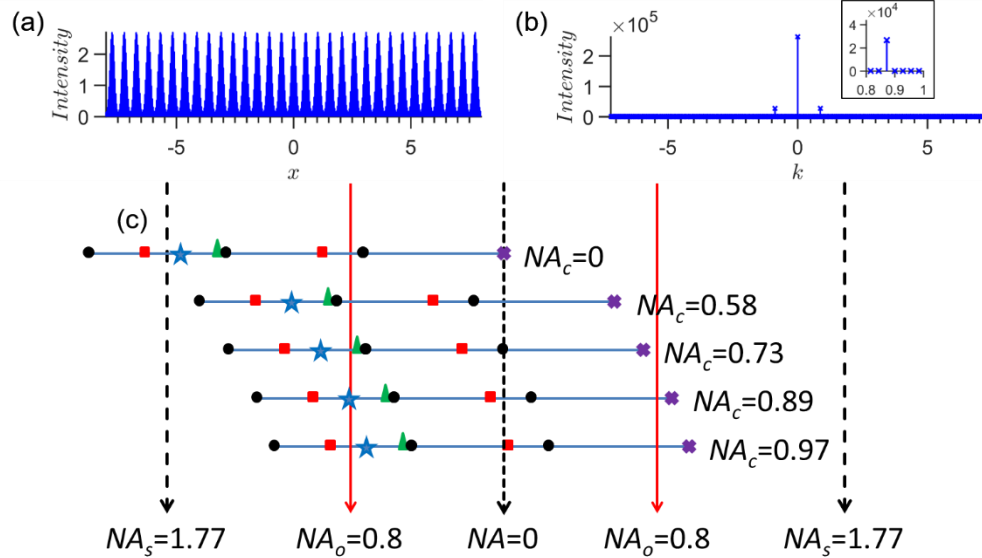


Figure 4.5 Images (a-b) are reconstructed images corresponding to $p=500$ nm period, for $NA_c=0.87$ and 0.97 . Image (c) shows the expected location of diffraction spots for different condenser numerical aperture values. [95, 100]

This conundrum can be solved by observing Fig. 4.5(c) which shows a sketch of expected location of the diffraction spots when different rows of the digitally controlled HDC are used to illuminate a periodic object under observation. Each row indicates the amount by which the diffraction orders would be shifted when inclined illumination corresponding to numerical aperture value indicated besides the line is used for illumination. The diffraction orders corresponding to the 500 nm periodicity are shown by red squares. Note that the when an objective lens with $NA_o=0.8$ is used, the zeroth diffraction order is outside the numerical aperture of the objective lens (indicated by red lines) when the LEDs in the third and fourth circular row of the digitally controlled HDC are used. Moreover, the spatial periodicity $p=500$ nm corresponds to $NA=0.9$, which indicates that the separation between the consecutive diffraction orders in the Fourier plane. Consequently, when using only third and fourth circular row of the digitally controlled HDC, only first order diffraction spot appears in the Fourier plane image, and hence, in accordance with the Abbe's theory of image formation, the periodicity $p=500$ nm is not revealed in the low resolution real plane images. This example clearly demonstrates when using inclined illumination from digitally controlled HDC, the range of periodicities that can be revealed when using inclined illumination at particular angle should be carefully considered.

Resolution limit of the imaging setups using FPM technique

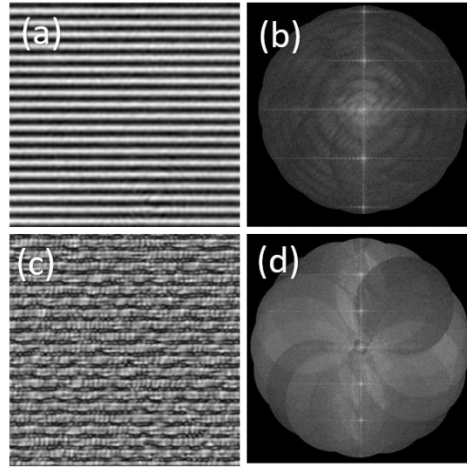


Figure 4.6 FPM reconstructed images corresponding to (a-b) $NA_c=0.58$ and 0.73 , and (c-d) $NA_c=0.87$ and 0.97 . [100]

When all LEDs of the digitally controlled HDC are sequentially used for illumination (NA_c up to ~ 1), if an objective lens with $NA_o=0.8$ is used to collect the light transmitted through the two-dimensional periodic object under observation, the lower limit of the range of periodicity that should be observed can be determined to be approximately 250 nm. For the given objective lens, the Rayleigh resolution limit can be determined to be approximately 281 nm. Consequently, to determine if the FPM technique can resolve a spatial periodicity below the Rayleigh resolution limit using an objective lens with $NA_o=0.8$, a two-dimensional periodic crystal with chromium pillars arranged in rectangular symmetry with periodicities $p_x=270$ nm and $p_y=600$ nm in mutually perpendicular directions was used. First, the periodic crystal was sequentially illuminated with all the LEDs in the first two circular rows of the digitally controlled HDC with $NA_c=0.58$ and 0.73 respectively, to obtain the low resolution real plane images, which were processed using the FPM image reconstruction algorithm, and the corresponding reconstructed real plane image and Fourier plane image are shown in Figs. 4.6(a) and 4.6(b). As indicated in Fig. 4.5(c) showing the expected location of the diffraction spots, the low resolution real plane images obtained with the first two circular rows of the digitally controlled HDC should be able to resolve the $p_y=600$ nm periodicity as it is possible of the objective lens to capture at least two consecutive diffraction orders, but the $p_x=270$ nm periodicity cannot be resolved. Consequently, the as none of the low resolution real plane images used for FPM image

reconstruction contain any information about the $p_x=270$ nm periodicity, the reconstructed real plane image in Fig. 4.6(b) reveals only the $p_y=600$ nm periodicity, and the associated reconstructed Fourier plane image has only diffraction orders related to $p_y=600$ nm periodicity. Hence, it can be concluded that the FPM image reconstruction algorithm might not be able to resolve a periodicity that is smaller than the Rayleigh resolution limit.

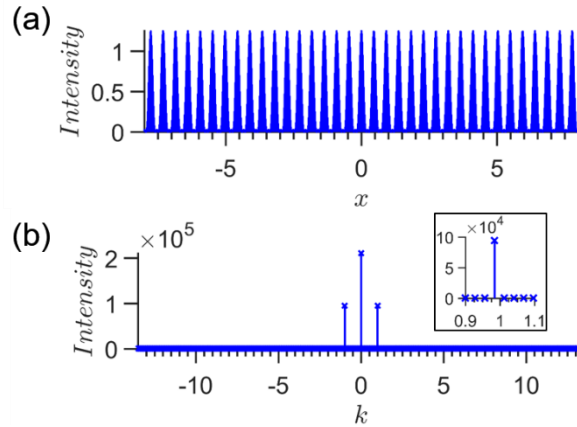


Figure 4.7 FPM reconstructed images for period $p=267$ nm that have an incorrect period of 459 nm in image (a), which can be verified by incorrect location of diffraction spikes at $NA=0.97$ in image (b). [95]

The experimental observation demonstrated in the above discussion can also be corroborated by computational simulations shown in Fig. 4.7. A hypothetical one-dimensional periodic crystal with $p=267$ nm was considered for the simulations, and corresponding low resolution real plane intensity was calculated for inclined illumination with $NA_c=0.87$ and 0.97 , which corresponds to the third and fourth circular rows of the digitally controlled HDC, and observed using a dry objective lens with $NA_o=0.8$. The reconstructed real space and Fourier space intensities obtained by processing these low resolution real space amplitude data using one-dimensional version of the FPM image reconstruction algorithm is shown in Figs. 4.7(a) and 4.7(b). Note that although the reconstructed real space intensity is periodic, an incorrect periodicity of 459 nm can be determined from the incorrect location of the diffraction spikes in the corresponding reconstructed Fourier space intensity. Note that incorrect location of the diffraction spikes matches the diffraction spikes that appear from the LED in the fourth row of the digitally controlled HDC with $NA_c=0.97$, which

is significantly different from the expected $NA=1.6875$ associated with $p=267$ nm periodicity. This observation not only confirms that the FPM technique cannot resolve periodicity below the Rayleigh resolution limit, but also indicates why an incorrect periodicity appears in reconstructed images.

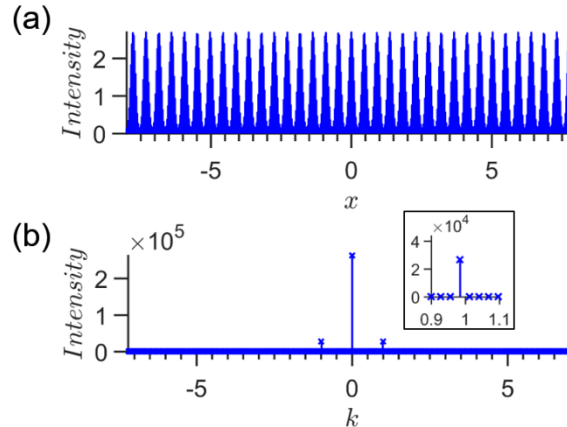


Figure 4.8 FPM reconstructed images for period $p=500$ nm that have an incorrect period of 459 nm in image (a) when only simulated low resolution real space intensity corresponding to $NA_c=0.97$ and 0.87 are used, which can be verified by incorrect location of diffraction spikes at $NA=0.97$ in (b). [95]

As indicated in Fig. 4.5(c) showing the expected location of the diffraction spots, the LED in the third circular row of the digitally controlled HDC does not produce a diffraction order in the Fourier space that can be captured in objective lens with $NA_o=0.8$. Hence, to determine if the diffraction order appearing in the Fourier space is created due to the illuminating LED, we reconsider the one-dimensional hypothetical periodic crystal with periodicity $p=500$ nm, and corresponding low resolution real plane intensity was calculated for inclined illumination with $NA_c=0.87$ and 0.97 that corresponds to the third and fourth circular rows of the digitally controlled HDC, respectively, and observed using a dry objective lens with $NA_o=0.8$.

However, for this study, the FPM image reconstruction algorithm began with calculating the simulated low resolution real space intensity using the LEDs in the fourth circular row of the digitally controlled HDC, which is then followed by LEDs in the third circular row of the digitally controlled HDC. The corresponding reconstructed real space intensity shown in Fig. 4.8(a) is periodic, but the periodicity that is determined from the corresponding Fourier space intensity shown in Fig. 4.8(b)

is 459 nm, which is associated with $NA_c=0.97$ related to fourth circular row of the digitally controlled HDC. This confirms the observation made when the FPM image reconstruction algorithm begins with the third circular row of the digitally controlled HDC in Fig. 4.5(b) that the incorrect diffraction spikes appearing in the reconstructed intensity correspond to the illumination from the LEDs used to obtain the low resolution intensity using which the algorithm begins.

In order to investigate this further, the first few steps of the FPM image reconstruction process have to be studied, as shown in Fig. 4.9. The FPM image reconstruction algorithm begins by considering that the amplitude and phase in the real space is uniformly one and zero, respectively. The low resolution real space intensity and phase shown in Figs. 4.9(a) and 4.9(b) is calculated from the shifted low-pass filtered Fourier space, as shown in equation (4.3). The intensity and phase of Fourier space shown in Figs. 4.9(c) and 4.9(d) is calculated after the information in the simulated low resolution intensity is inserted in the reconstruction process, as shown in equation (4.5). Now, the Fourier space intensity has to be shifted back to location of the wave-vector corresponding to illuminating LED, as indicated in equation (4.7). As the diffraction spike is located at $k=0$ in Fig. 4.9(d), after shifting the by $-k_j$ (which is -0.87 in numerical aperture units), the diffraction peak gets shifted to $k=-k_j=-0.87$, which is the wave-vector corresponding to illuminating LED, which causes the incorrect periodicity in the reconstructed real space and Fourier space intensity. On the other hand, the low resolution intensity and corresponding phase (that is not measured in the experimental process) is shown in Figs. 4.9(e) and 4.9(f), and the intensity and phase of Fourier space shown in Figs. 4.9(g) and 4.9(h) is calculated after the information in the simulated low resolution intensity and phase is inserted in the reconstruction process, as shown in equation (4.5). Note that on using the correct phase, the diffraction spike is now located at $NA=-0.03$, and hence, on shifting the intensity back by wave-vector of the LED used for illumination ($-k_j=-0.87$ in numerical aperture units), the diffraction spike gets shifted to $NA=-0.9$, which corresponds to correct periodicity of $p=500$ nm, hence resulting in the correct periodicity in the reconstructed real space and Fourier space intensity. Also, as the low resolution real space amplitude is constant, the information of the required shift of the

Fourier space is entirely in the phase in the real plane. However, phase is not measured during experimental data-acquisition, and consequently, FPM technique cannot be expected to reveal any spatial periodicity of a single periodic structure that is smaller than the Rayleigh resolution limit.

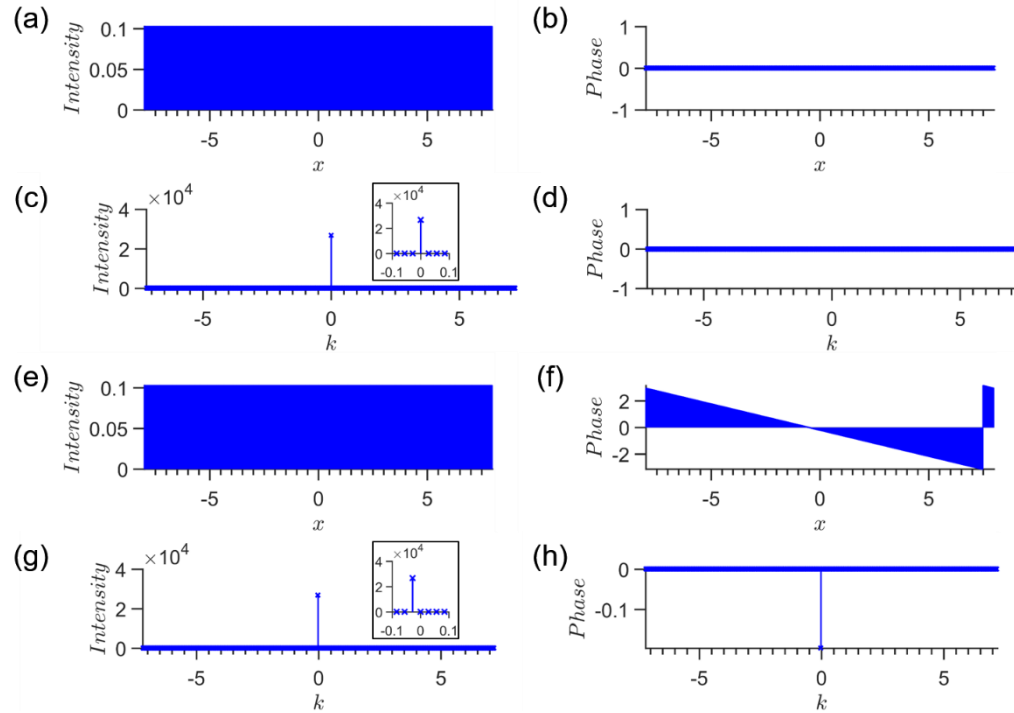


Figure 4.9 Low resolution real space and corresponding Fourier space intensity and phase in the initial steps of FPM process is shown in images (a-d). On using correct phase shown in (f) that is obtained from simulations, the initial shift in Fourier space results in correct location of diffraction spike at the end of iteration. [95]

However, recently, there have been several reports indicating that the resolution achieved using FPM technique can be better than the Rayleigh resolution limit [83, 92]. In order to solve this conundrum, the object under observation was considered to have multiple periodic structures: $p_1=267$ nm, $p_2=400$ nm and $p_3=667$ nm, and then the steps of FPM image reconstruction were studied. The corresponding intensity and phase that serves as object under observation is as shown in Fig. 4.10(a) and 4.10(b). The low resolution real space intensities that correspond to sequential illumination using all wave-vector values LEDs of digitally controlled HDC and light acquisition using an objective lens with $NA_o=0.8$ are calculated, and then they are processed using FPM image reconstruction algorithm.

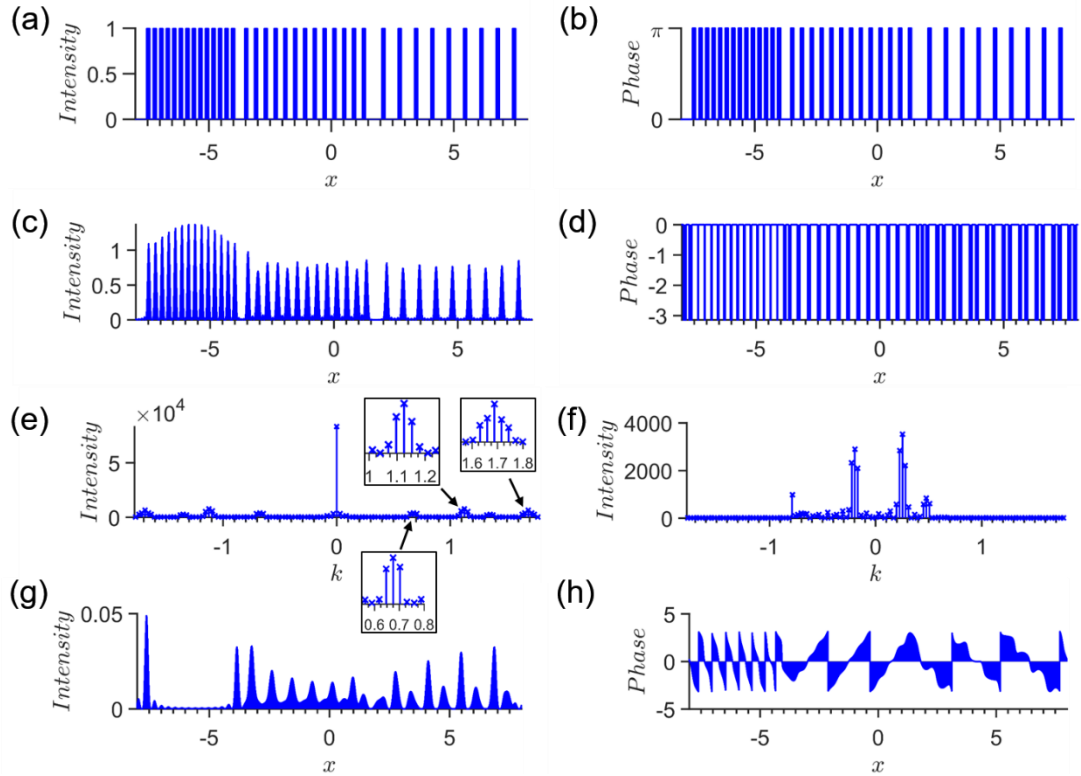


Figure 4.10 Images in (a, b) show real space intensity and phase that serves as the object under observation. The corresponding FPM reconstructed real space intensity and phase is shown in images (c-d). Images (e-h) show the beginning of the process for $NA_c=0.87$ in the first iteration of the FPM reconstruction process. [95]

The reconstructed real space and Fourier space intensity and phase are shown in Figs. 4.10(c-d) and 4.10(e-f). The correctness of the periodicity appearing in the reconstructed real space intensity shown in Fig. 4.10(c) can be verified from the correct location of the first order diffraction spikes in the reconstructed Fourier space intensity shown in Fig. 4.10(d), which is found to be at 0.675 (corresponding second order diffraction spike is at 1.35), 1.125, and 1.6875, respectively. This indicates that in the FPM technique, the presence of the larger spatial periodicities in the object under observation helps in resolving the periodicities that are smaller than the Rayleigh resolution limit.

Fig. 4.10(g) shows the real space intensity as the FPM image reconstruction algorithm begins processing the low resolution real space intensity corresponding to $NA_c=0.87$. Note that the magnitude of the initial shift of the Fourier space intensity can be determined to be $\Delta = \mp \left[\lambda/p - NA_c \right] = \mp \lambda/\Phi$, where Φ is the periodicity of the

unmeasured real space phase shown in Fig. 4.10(h), and the negative (positive) sign occurs when the illumination wave-vector is positive (negative). Thus, the initial shift is determined to be -0.255 for $p_2=400$ nm periodicity. The FPM image reconstruction algorithm should be able to calculate the initial shift as the periodicity $p_2=400$ nm is larger than Rayleigh resolution limit. Hence, when the Fourier space is shifted back by numerical aperture of the illuminating LED, the diffraction order gets relocated to $-0.255-0.87=-1.125$, which corresponds to $p_2=400$ nm periodicity. Note that the initial shift has to be applied to the entire Fourier space, and thus, the presence of spatial periodicity that is larger than the Rayleigh resolution limit helps the algorithm to reveal the periodicities that are smaller than the Rayleigh resolution limit. Consequently, the $p_1=267$ nm periodicity of reconstructed real space intensity shown in Fig. 4.10(c) appears to have been calculated correctly by the FPM image reconstruction algorithm.

Convergence of the FPM image reconstruction algorithm

As per the study of the FPM technique presented in the preceding sections, the performance of the FPM image reconstruction algorithm depends on whether the object being observed contains single or multiple periodicities, and whether these periodicities are larger or smaller than the Rayleigh resolution limit. The convergence of the FPM image reconstruction algorithm can be determined from the mean squared error metric, that compares the finally reconstructed real plane image with the perfectly periodic intensity that serves as an object under illumination [93-94]. The normalized mean-squared error metric of the DSM image reconstruction algorithm was calculated at the end of every iteration of FPM image reconstruction algorithm for up to 600 iterations, and the average value for all considered periodicities were determined to be as shown in Fig. 4.11.

First, the average value of normalized mean-squared error metric was calculated for one-dimensional FPM image reconstruction simulations that were conducted for thousands of periodic crystals whose periods were larger than the Rayleigh resolution limit corresponding to illumination pass band of $NA_o=0.8$ ($300 \text{ nm} < p < 600 \text{ nm}$). As shown in Fig. 4.11(a), the FPM image reconstruction algorithm

converges correctly for objects with single spatial periodicity that is larger than the Rayleigh resolution limit within a couple of iterations. Then, the average value of normalized mean-squared error metric was calculated for one-dimensional FPM image reconstruction simulations that were conducted for thousands of periodic crystals whose periods are smaller than the Rayleigh resolution limit corresponding to illumination pass band of $NA_o=0.8$ ($260 \text{ nm} < p < 280 \text{ nm}$).

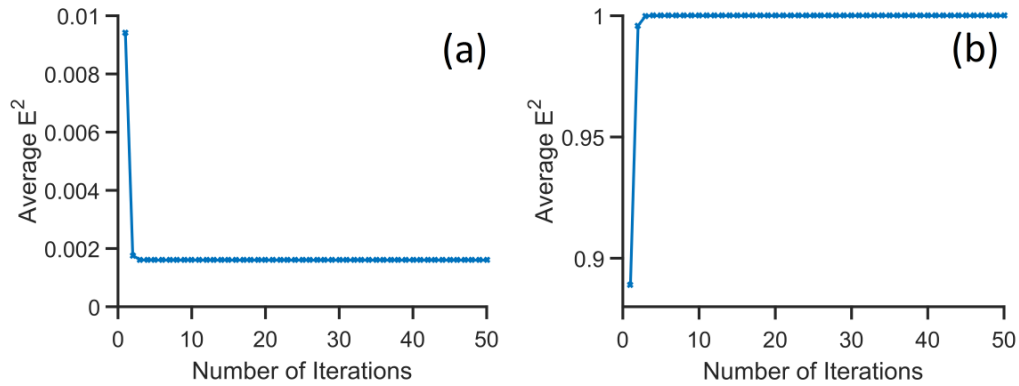


Figure 4.11 Convergence of the FPM image reconstruction algorithm. Average normalized mean-square error metric for thousands of periodicities in the following ranges (a) $300 \text{ nm} < p < 600 \text{ nm}$, and (b) $260 \text{ nm} < p < 280 \text{ nm}$, for numerical aperture value of $NA_o=0.8$ corresponding to the objective lens. [95]

As shown in Fig. 4.11(b) the FPM image reconstruction algorithm converges very quickly to an incorrect periodicity for objects with single spatial periodicity that is smaller than the Rayleigh resolution limit. This confirms that the FPM technique is a near diffraction-limited technique in photonic crystal imaging applications when the field-of-view contains a single spatial periodicity.

CHAPTER 5

DUAL-SPACE MICROSCOPY USING HEMISPHERICAL DIGITAL CONDENSERS

The variable illumination provided by digitally controlled hemispherical digital condensers (HDCs) permits implementation of phase retrieval techniques like the Fourier Ptychographic Microscopy (FPM) technique that provide enhanced resolution due to large synthetic numerical aperture with simultaneous phase recovery. In comparison to the conventional snap-shot imaging techniques, the FPM technique allows relatively higher throughput, which can be quantified in terms of the space-bandwidth product. However, FPM technique is based on processing the low resolution real plane intensity images, which do not contain any information about all the periodicities of the object under observation that are smaller than that corresponding to the Rayleigh resolution limit. Consequently, the FPM technique remains near diffraction-limited for photonic crystal imaging applications [95].

Both real space and the Fourier space possess equal amount of information of the complex optical disturbance in an imaging planes [83, 90, 96]. However, the conventional imaging sensors couples to the imaging setups do not measure phase of the complex optical disturbance. Moreover, as seen in the previous chapter, when the spatial periodicity is smaller than that corresponding to the Rayleigh resolution limit, the information about the periodicity is located in the unmeasured phase in the real plane. Hence, when imaging spatial periodicities below the diffraction limit, the real plane images are not equivalent to the Fourier plane images.

When using digitally controlled HDC to illuminate a periodic object with a spatial periodicity that is smaller than that corresponding to Rayleigh resolution limit, the separation between the diffraction orders in the Fourier space is larger than the numerical aperture of the light-collecting objective lens used in the imaging setup [81]. Hence, no two consecutive diffraction orders ever appear simultaneously in the

back focal-plane of the objective lens. The inclined illumination from the digitally controlled HDC causes the zeroth order diffraction feature to remain outside the numerical aperture of the objective lens, so that the first diffraction order can be captured. Thus, the Fourier space has some information about the spatial periodicity that is smaller than the Rayleigh resolution limit. However, corresponding real plane is has a constant intensity corresponding to the diffraction order that appears in the back focal-plane of the objective lens, and hence, it does not have any information about the associated spatial periodicity of the object. This phenomenon is in accordance with the Abbe's theory of image formation, which states that unless two consecutive diffraction orders appear in the back-focal plane of the light collecting objective lens, the information about the spatial periodicity of an object will not appear in the real plane of the imaging setup. In a way, this indicates that the back focal-plane image of the objective lens has more information than the real plane image. Hence, in order to overcome the diffraction-limited performance of the FPM technique, the Fourier plane images corresponding to the experimentally acquired low resolution real plane images can be used in the reconstruction algorithm. In the following chapter, a recently proposed phase retrieval technique called Dual Space Microscopy (DSM) has been discussed [96, 97], which is based on numerically processing the experimentally acquired low resolution real plane images and corresponding Fourier plane images to construct an image with enhanced resolution, while simultaneously recovering the phase that is lost during experimental acquisition of images.

Implementation of Dual Space Microscopy technique

The experimental setup for the DSM technique is similar to the experimental setup for FPM technique that is shown in Fig. 4.1(a) in the previous chapter. The digitally controlled HDC is used to illuminate the object under observation at various angles, and the corresponding real plane and back focal-plane images are simultaneously recorded by the cameras. These experimentally acquired images are then processed using the DSM image reconstruction algorithm, which begins by assuming that the intensity and the phase of the light transmitted through the object under observation is uniformly one and zero, respectively, whose corresponding Fourier space would be as shown in the equation below (in the beginning, $v = 0$):

$$Z_0 = A(\vec{k})e^{i\phi(\vec{k})} = \mathcal{F}[a(\vec{r})e^{i\psi(\vec{r})}] \quad (5.1)$$

A low-pass filter corresponding to the numerical aperture of the objective lens used for experimental data-acquisition (W) is applied to the reconstructed image, after the image is shifted towards the center of the Fourier plane by the amount corresponding to the wave-vector of the illuminating LED (k_j), as shown in the equation below:

$$B(\vec{k})e^{i\phi(\vec{k})} = W \cdot [A(\vec{k} - \vec{k}_j)e^{i\phi(\vec{k} - \vec{k}_j)}] \quad (5.2)$$

At this step, the DSM technique differs from the FPM technique: the information in the experimentally acquired Fourier plane images is added to the image reconstruction process, as shown below:

$$B(\vec{k})e^{i\phi(\vec{k})} \xrightarrow{\text{Replace amplitude}} B_{exp}(\vec{k})e^{i\phi(\vec{k})} \quad (5.3)$$

Using two-dimensional Fast Fourier Transform (FFT) function, the amplitude in the corresponding low resolution real plane image is replaced by the amplitude of the experimentally acquired image to add the experimentally acquired “information”, as shown in the equations below:

$$b(\vec{r})e^{i\chi(\vec{r})} = \mathcal{F}^{-1} [B_{exp}(\vec{k})e^{i\phi(\vec{k})}] \quad (5.4)$$

$$b(\vec{r})e^{i\chi(\vec{r})} \xrightarrow{\text{Replace amplitude}} b_{exp}(\vec{r})e^{i\chi(\vec{r})} \quad (5.5)$$

Then, the data is transformed back to the Fourier plane using two-dimensional inverse FFT function, and is low-pass filtered to only include the amount that can be captured by objective lens, and then shifted back to the location corresponding to the location of the wave-vector of the illuminating LED, as shown in the equations below:

$$c(\vec{k})e^{i\psi(\vec{k})} = \mathcal{F}[b_{exp}(\vec{r})e^{i\chi(\vec{r})}] \quad (5.6)$$

$$D(\vec{k})e^{i\theta(\vec{k})} = W \cdot [c(\vec{k} + \vec{k}_j)e^{i\psi(\vec{k} + \vec{k}_j)}] \quad (5.7)$$

The information already present in the Fourier space that is being reconstructed is given by the following equation, which can be derived from equation (5.2):

$$E(\vec{k})e^{i\theta(\vec{k})} = B(\vec{k} + \vec{k}_j)e^{i\phi(\vec{k}+\vec{k}_j)} \quad (5.8)$$

Hence, the “new information” from the updated data is added to the reconstructed Fourier plane image as shown in the equation below:

$$Z = Z_0 + \beta \cdot [D(\vec{k})e^{i\theta(\vec{k})} - \gamma E(\vec{k})e^{i\theta(\vec{k})}] \quad (5.9)$$

In the above equation, β and γ are image update parameters that can be adjusted between 0 and 1 for finer image reconstruction. For the simulations discussed in this chapter, the image update parameters β and γ are set to 1 and 0, respectively. Finally, after updating the reconstructed Fourier plane image, the reconstructed real plane intensity and corresponding phase are obtained using two-dimensional FFT function. Note that for subsequent pairs of the low resolution real plane image and the corresponding back focal-plane image to be processed, the new $Z_0 = Z$. These steps are repeated until all the experimentally acquired “information” in the low resolution real plane images and corresponding back focal-plane images is systematically added to the reconstructed image, which constitutes a single iteration of the DSM algorithm. The DSM algorithm is expected to converge after several iterations.

Computational simulations can also be performed to understand the DSM technique [97]. The process to create the low resolution real space intensity and Fourier space intensity corresponding to limited angular-acquisition of transmitted light is similar to that in the simulations for the FPM technique shown in the previous chapter. Fig. 5.1(a) show the two-dimensional periodic crystal with periodicities $p_x=300$ nm and $p_y=500$ nm in mutually perpendicular directions, which has been created using computational simulations, and the corresponding Fourier space is shown in Fig. 5.1(b). This pair of real and Fourier space serves as the hypothetical object for simulations that mimic actual experimental acquisition. The simulated low resolution intensity in real space and corresponding Fourier space shown in Fig. 5(c) and 5(d) are generated for $NA_c=0.97$ using the method described in the previous chapter for all wave-vector values corresponding to the illumination from LEDs in the digitally controlled HDC, and $NA_o=0.8$.

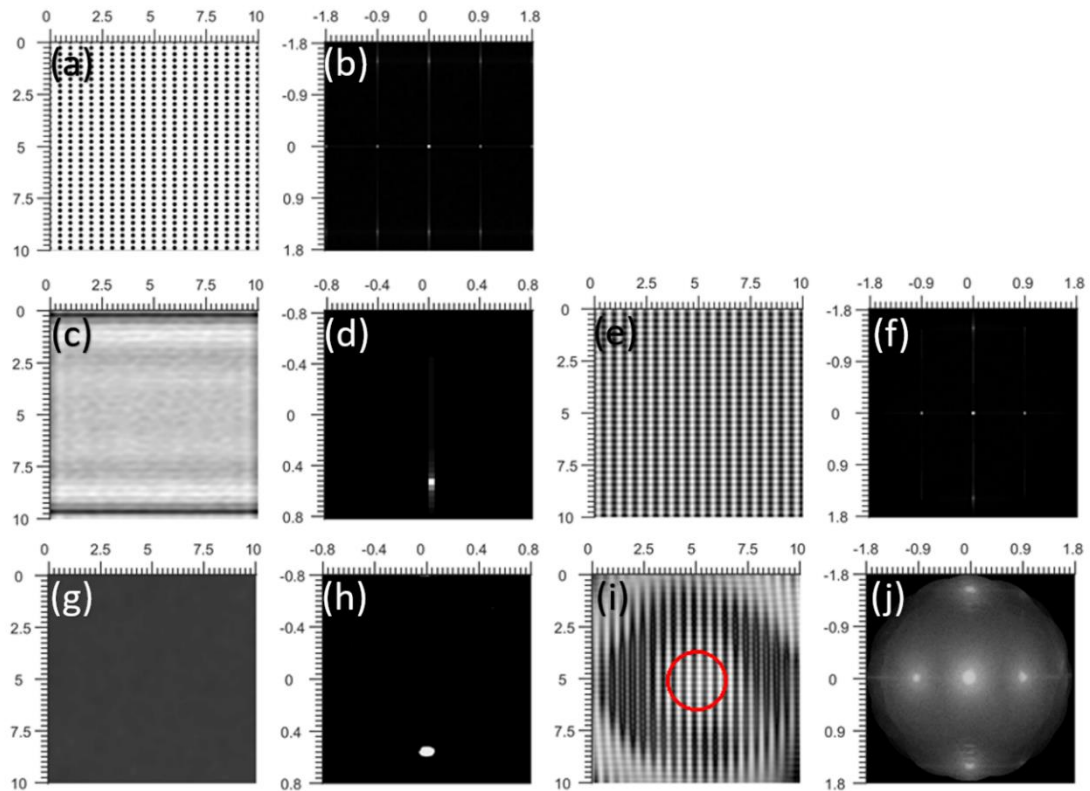


Figure 5.1 (a) is RP image that serves as the object, and (b) is the corresponding FP image. (c-d) is a pair of simulated low resolution RP image and corresponding FP image obtained using $NA_c=0.97$. (e-f) is a pair of reconstructed RP image and corresponding FP image obtained from processing simulated images. (g-h) is a pair of experimentally acquired low resolution RP image and corresponding FP image obtained using $NA_c=0.97$. (i-j) is a pair of reconstructed RP image and corresponding FP image obtained from processing experimental images. [97]

Figs. 5(e) and 5(f) show real space and Fourier space that is reconstructed by processing all the simulated low resolution intensity in real space and corresponding Fourier space using the DSM image reconstruction algorithm. The periodicity of the object is clearly visible in the reconstructed real space, and the correctness of the periodicity can be verified from the location of the first order diffraction spots at $\lambda/p_x = 1.5$ and $\lambda/p_y = 0.9$ in the reconstructed Fourier space. As discussed previously, this clearly demonstrates the sub-wavelength resolution imaging capability of the DSM technique.

The sub-wavelength resolution imaging capability of the DSM technique can also be demonstrated experimentally. For this, the low resolution real plane images

and the corresponding Fourier plane images of two-dimensional periodic crystal of chromium pillars with $p_x=300$ nm and $p_y=500$ nm were acquired using a dry objective lens with $NA_o=0.8$ for all LEDs of the digitally controlled HDC. For comparison, a pair of low resolution real plane image and corresponding Fourier plane image acquired using $NA_c=0.97$ illumination from LED of the digitally controlled HDC are shown in Figs. 5.1(g) and 5.1(h). The experimentally acquired low resolution real plane images and corresponding Fourier plane images were processed using DSM image reconstruction algorithm, and the corresponding pair of reconstructed real plane image and Fourier plane image is shown in Fig. 5.1(i) and 5.1(j). Clearly, the diffraction orders produced by the illumination from the LEDs in the digitally controlled HDC are much larger in comparison to the diffraction orders appearing in the simulated images. This indicates that the plane-wave approximation in the imaging techniques like FPM and DSM is an approximation to the actually emitted divergent beam of light. Moreover, this also reduces the field of view (FOV) in the real plane in terms of the intrinsic condenser numerical aperture of the LEDs (NA_{LED}) as follows:

$$FOV = \frac{(\lambda/NA_{LED})}{2\pi} \quad (5.10)$$

Using the Fourier plane images corresponding to the experimentally acquired low resolution real plane images, the condenser numerical aperture of the illumination from LEDs was determined to be approximately 0.05, which corresponds to FOV of approximately $1.4 \mu\text{m}$, which is in good correspondence with the field-of-view of the reconstructed real plane image shown in Fig. 5.1(i), which is shown with a red-colored circumference.

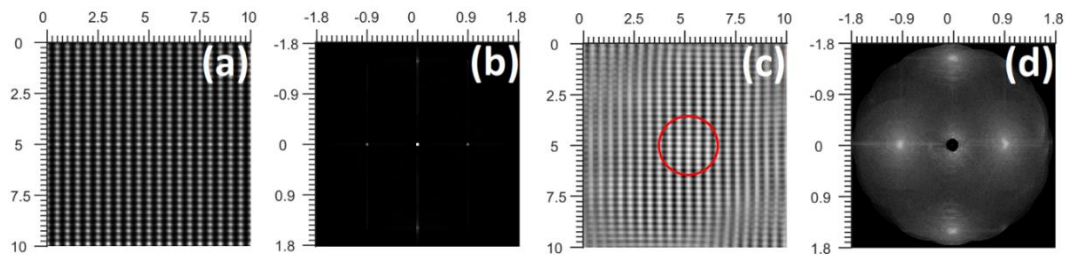


Figure 5.2 Pairs of reconstructed RP and FP images obtained using (a-b) simulated images, and (c-d) experimentally acquired images. [97]

Fig. 5.2(a-b) shows the pair of real space and Fourier space images that are reconstructed using the simulated images showing the low resolution real space intensity and corresponding Fourier plane intensity that were generated using the wave-vector values corresponding to the third and fourth circular rows of the digitally controlled HDC ($NA_c=0.87$ and 0.97) in the DSM image reconstruction algorithm. As the wave-vector values are larger than the low-pass filter associated with limited angular-acquisition of the objective lens, this simulation corresponds to imaging in dark-field configuration. Fig. 5.2(c-d) shows the pair of real plane and Fourier plane images that are reconstructed using the low resolution real plane images and corresponding Fourier plane images that are experimentally acquired in dark-field configuration using the third and fourth circular rows of the digitally controlled HDC ($NA_c=0.87$ and 0.97) in the DSM image reconstruction algorithm. The red circumference shows the effective FOV in the reconstructed real plane intensity image shown in Fig. 5.2(c). This demonstrates that the DSM image reconstruction algorithm can reveal the periodicity of the object when the experimental low resolution real plane images and corresponding Fourier plane images are obtained in the dark-field configuration.

Super-resolution imaging of periodic crystals using DSM technique

As mentioned in the previous chapter, the Rayleigh resolution limit of the experimental setup used for DSM technique that uses objective lens with numerical aperture $NA_o=0.8$ is approximately 281 nm. However, for inclined illumination from the fourth circular row of the digitally controlled HDC ($NA_c=0.97$), the minimum resolvable periodicity is determined to be approximately 254 nm. Hence, simulated low resolution real space images and corresponding Fourier space images were generated for periodic crystal with periodicities $p_x=270$ nm and $p_y=600$ nm in mutually perpendicular directions for all wave-vector values that correspond to illumination from LEDs of the digitally controlled HDC, and were processed using the DSM image reconstruction algorithm. As seen in the Fig. 5.3(a) showing the reconstructed real space image, both periodicities of the object under observation are clearly resolved, and the correctness of the periodicity can be easily verified from the location of the

first order diffraction orders at $\lambda/p_x = 1.6875$ and $\lambda/p_y = 0.75$ reconstructed Fourier space image shown in Fig. 5.3(b). In order to experimentally verify if the DSM technique can be implemented for super-resolution, a two-dimensional periodic crystal of chromium pillars that are distributed in rectangular symmetry with periodicities $p_x=270$ nm and $p_y=600$ nm in mutually perpendicular directions was used as object under observation.

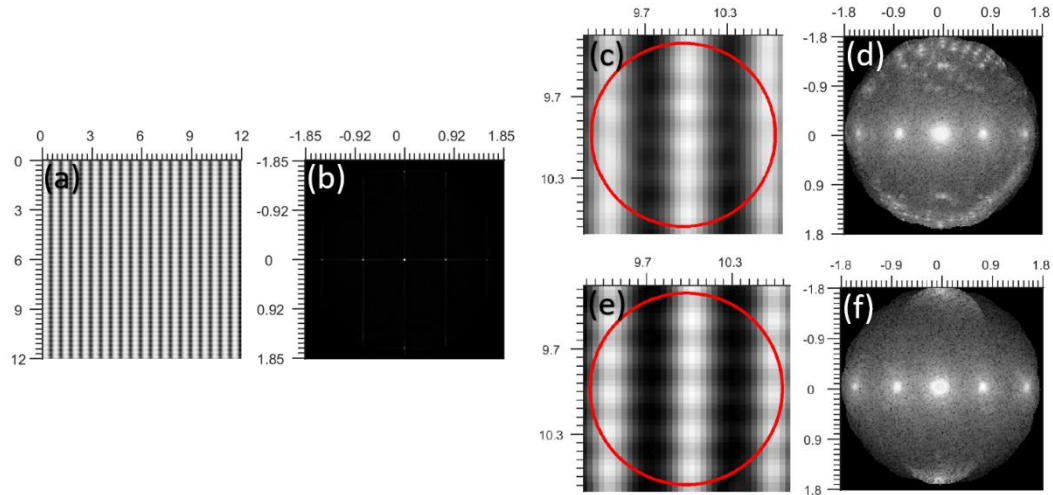


Figure 5.3 Pairs of reconstructed RP and FP images obtained from (a-b) simulated images, (c-d) experimentally acquired RP and FP images, and (e-f) experimentally acquired RP and FP images that were processed to remove noise related to reflections from the inner surface of the digitally controlled HDC source. [97]

Figs. 5.3(c-d) show the reconstructed real plane and Fourier plane images that were obtained by processing all the experimentally acquired low resolution real plane images and corresponding Fourier plane images. Unlike the simulations, the reconstructed real plane image obtained from the experimentally acquired images has two undesirable features: (1) small field of view – which can be attributed to the divergent illumination from the LEDs of the digitally controlled HDC, and (2) poor contrast – which can be attributed to the noise appearing in the experimentally acquired images due to reflections from the internal surface of the dome of the digitally controlled HDC. The effect of reflections can be identified from the noise appearing in the reconstructed Fourier plane image shown in Fig. 5.3(d).

In order to confirm this observation, we removed the noise from the experimentally acquired Fourier plane images using simple image masking

procedures, and used the resulting post-processed images in the DSM image reconstruction algorithm. The resulting reconstructed real plane image with relatively better contrast that is shown in Fig. 5.3(e), and the relatively “cleaner” reconstructed Fourier plane image shown in Fig. 5.3(f) are clearly indicating that the poor contrast in the reconstructed images shown in Figs. 5.3(c-d) can be attributed to the noise in the experimentally acquired images because of the reflections from the internal surface of the dome of the digitally controlled HDC. This undesirably small field-of-view can be made larger by replacing the LEDs with a Laser illumination source that can provide nearly plane-wave illumination, in the conventional design of the digitally controlled HDC, which should result in very narrow diffraction spots in the experimentally acquired Fourier plane images.

Convergence of the DSM image reconstruction algorithm

In this section, the convergence of the DSM image reconstruction algorithm is discussed using the simpler and faster one-dimensional version of the conventional two-dimensional version discussed in the above sections, and the corresponding results are shown in Figs. 5.4, 5.5, and 5.6. Using a low-pass filter with $NA_o=0.8$ corresponding to the limited angular-acquisition of the objective lens was used to generate the low resolution real space and corresponding Fourier space intensity, which was then processed using the DSM image reconstruction algorithm.

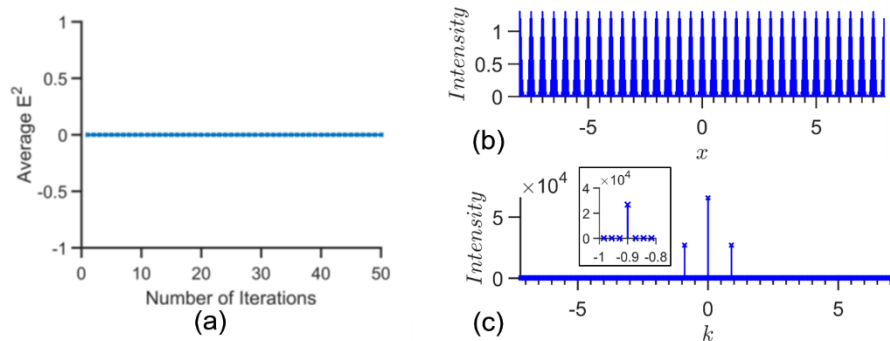


Figure 5.4 (a) Average normalized mean-squared error-metric for Group 1. (b-c) Reconstructed real space and Fourier space for $p=500$ nm from Group 1. [96]

Thousands of periodicities of crystals were analyzed to study the convergence DSM image reconstruction algorithm, which can be classified into three groups: (1) single spatial periodicity that is larger than the Rayleigh resolution limit ($300 \text{ nm} < p <$

600 nm), (2) single spatial periodicity that is smaller than the Rayleigh resolution limit, but larger than the resolution achieved by the fourth circular row of the digitally controlled HDC ($260 \text{ nm} < p < 280 \text{ nm}$), and (3) multiple spatial periodicities: with two periodicities being larger than the Rayleigh resolution limit ($300 \text{ nm} < p < 600 \text{ nm}$), and one periodicity being smaller than the Rayleigh resolution limit but larger than the resolution achieved by the fourth circular row of the digitally controlled HDC ($260 \text{ nm} < p < 280 \text{ nm}$).

Using these three groups of periodic crystals, the convergence of the DSM image reconstruction algorithm at the end of every iteration was quantified in terms of the normalized mean-squared error metric up to 600 iterations using the formulation that has been suggested in Ref. [93]. The low-pass filter corresponding to the limited angular-acquisition of the objective lens was $NA_o=0.8$.

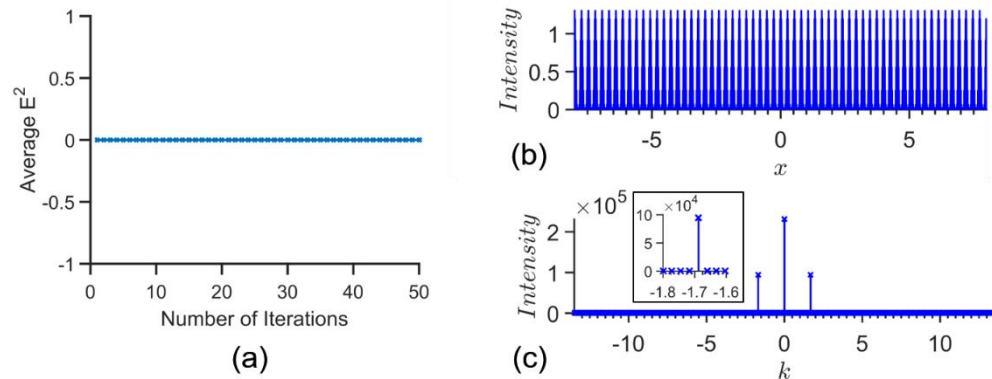


Figure 5.5 (a) Average normalized mean-squared error-metric for Group 2. (b-c) Reconstructed real space and Fourier space for $p=267 \text{ nm}$ from Group 2. [96]

Fig. 5.4(a) shows the average value of the normalized mean-squared error metric for each iteration of DSM image reconstruction algorithm used for thousands of periodicities in Group 1 that have a single spatial periodicity that is larger than the Rayleigh resolution limit ($300 \text{ nm} < p < 600 \text{ nm}$), which shows that the DSM image reconstruction algorithm rapidly converges to approximately zero for this set of periodicities. It is not possible to show the reconstructed real space for all the periodicities that were considered for simulations, however, reconstructed real and Fourier space for periodicity $p=500 \text{ nm}$ has been shown in Figs. 5.4(b) and 5.4(c).

Note that the real space reconstructed has the correct periodicity, which can be verified from correct location of the first order diffraction spikes at $\lambda/p = 0.9$.

Likewise, for Group 2 with single spatial periodicity that is smaller than the Rayleigh resolution limit, but larger than the resolution achieved by the fourth circular row of the digitally controlled HDC ($260 \text{ nm} < p < 280 \text{ nm}$), the DSM image reconstruction converges rapidly to the correct periodicity, as shown in Fig. 5.5(a). An example of the reconstructed real space obtained for a single periodicity of $p=267 \text{ nm}$ shown in Fig. 5.5(b) reveals that the periodicity was reconstructed correctly, which can be verified from first order diffraction spikes appearing at $\lambda/p = 1.6875$ in the reconstructed Fourier space shown in Fig. 5.5(c). Note that FPM image reconstruction algorithm does not converge to correct single spatial periodicity when the period is smaller than the Rayleigh resolution limit, but larger than the resolution achieved by the fourth circular row of the digitally controlled HDC.

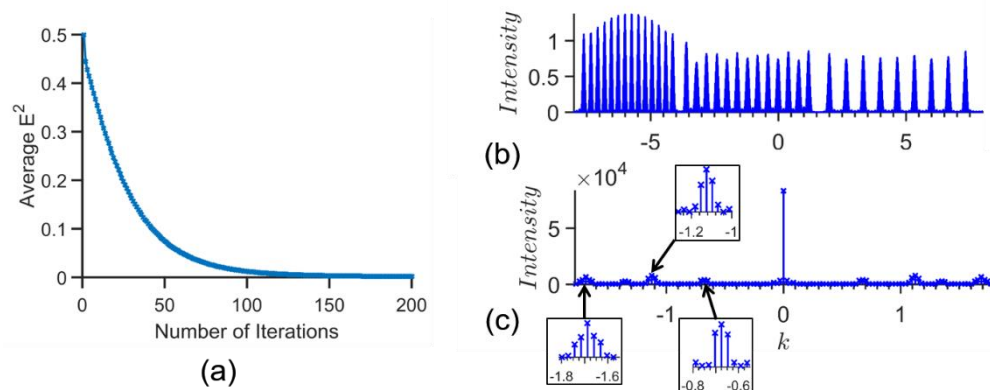


Figure 5.6 (a) Average normalized mean-squared error-metric for Group 3. (b-c) Reconstructed real space and Fourier space for $p_1=267 \text{ nm}$, $p_2=400 \text{ nm}$, and $p_3=667 \text{ nm}$, which belongs to Group 3. [96]

Lastly, for Group 3 with multiple spatial periodicities with two periodicities being larger than the Rayleigh resolution limit ($300 \text{ nm} < p < 600 \text{ nm}$), and one periodicity being smaller than the Rayleigh resolution limit but larger than the resolution achieved by the fourth circular row of the digitally controlled HDC ($260 \text{ nm} < p < 280 \text{ nm}$), the DSM image reconstruction algorithm converges at approximately 200 iterations, as shown in Fig. 5.6(a). The example shown from Group 3 has three

spatial periodicities: 267 nm, 400 nm, and 667 nm, and the reconstructed real space and Fourier space are shown in Figs. 5.6(b) and 5.6(c). Note that the correct location of the first order diffraction spikes at 0.675, 1.125, and 1.6875 appearing in the reconstructed Fourier space shown in Fig. 5.6(c) indicates that the reconstructed real space shown in Fig. 5.6(b) has converged correctly.

CHAPTER 6

CONCLUSION

This dissertation is focused on various techniques of high lateral resolution microscopy of photonic crystals. Optical characterization techniques have made tremendous progress over the last few centuries, which can be attributed to advancement in fabrication techniques and numerical processing techniques.

The study of the Ultra-Thin Condensers presented in Chapter II reveals the use of plasmonic and total internal reflection related evanescent surface waves for observing the object under observation with highly inclined illumination. The imaging structures discussed in this chapter were revealed as optical condensers for the first time. These optical condensers are several orders of magnitude smaller than the bulky conventional design of optical condensers that contains different types of optical and mechanically moving parts. Also, these Ultra-Thin Condensers are demonstrated to be capable of achieving true sub-wavelength resolution. As these optical condensers have shallow depth of penetration in to the dielectric layer, they are ideal for optical characterization of two-dimensional periodic crystals and nanomaterials. The Non-plasmonic Ultra-Thin Condensers based on total internal reflection related evanescent waves can be fabricated easily, and provide a cost-effective technique for sub-wavelength imaging. Plasmonic Ultra-Thin Condensers have an excellent potential for achieving super-resolution in the future when an appropriate high refractive index dielectric layer is used in combination with the metal layer. Moreover, the limitations brought about by the imaging optics can be removed using direct (lensless) observation techniques.

Chapter III reveals the mysterious condenser-like behavior of the wet-mounting setups that are commonly used in biological imaging laboratories. The “simplest possible microscope condenser” structure and the coverslip-sandwich condenser structure are shown to provide true sub-wavelength imaging capability for observation. The origin of the condenser-like behavior and several important characteristics of such optical condensers are revealed using a series of experimental

results and computational simulations. It is shown that these optical condensers are formed due to the light getting scattered at the inner edge of the top aperture of the oil-immersion objective lens and gets reflected back to the object under observation from the surface of the top semi-spherical lens, thus illuminating the object under observation with total internal reflection related evanescent surface waves, or by reflection from the top surface of the imaging structure. Moreover, the geometry of the condensers used for this purpose are shown to permit formation of an optical cavity, which enhances the efficiency of these condensers. These optical condensers are also shown to be easily reconfigured by altering the spacer thickness in case of coverslip-sandwich condenser structures, and by depositing a large drop of low boiling point liquid over the “simplest possible condenser” structure and coverslip-sandwich structure to provide variable numerical aperture. Along with this, an add-on optical module is presented, which not only assists in revealing the origin of the condenser-like behavior, but also capable for optical detection of two-dimensional periodic crystals with a resolution that is approximately eight times smaller than the Rayleigh resolution limit of the imaging setup. The circular condenser rings appearing in the back-focal plane of the objective lens used for observation can be used in combination with phase-retrieval techniques for deep sub-wavelength resolution.

Most of the techniques require special sample preparation to achieve high resolution imaging. However, numerical processing techniques can be used to reconstruct high resolution images by processing the acquired low resolution images. Chapter IV discusses the performance of the Fourier Ptychographic Microscopy, a phase-retrieval imaging technique, which is known to provide deep sub-wavelength resolution capability by “stitching” a large synthetic numerical aperture by using the experimentally acquired low resolution real image images, while simultaneously acquiring the unmeasured real plane phase. Using experimental results and computational simulations, it is revealed that Fourier Ptychographic Microscopy technique cannot image structure with a single spatial periodicity along mutually perpendicular directions that is smaller than the Rayleigh resolution limit. This is in contrast with the reported experimental results of super-resolution imaging of non-periodic objects using Fourier Ptychographic Microscopy technique. Also, using

experimental results and computational simulations of an object with a mixture of periodicities, it is demonstrated how the spatial periodicity larger than Rayleigh resolution limit assists in revealing the spatial periodicity that is smaller than Rayleigh resolution limit. Chapter V reveals more recently proposed Dual-Space Microscopy technique, which processes both low resolution real plane intensity images and corresponding Fourier plane intensity images with low numerical aperture to “stitch” a large synthetic numerical aperture, while simultaneously recovering the unmeasured phase. Using experimental results and computational simulations, it is demonstrated that when an object with single spatial periodicity that is less than Rayleigh resolution limit is illuminated with inclined light, the information of the spatial periodicity is not present in the real plane intensity image, however, the Fourier plane intensity image may have diffraction order spot corresponding to the periodicity. Dual-Space Microscopy technique incorporates this information of the periodicity from the Fourier plane intensity image. Using experimental results and computational simulations it is demonstrated that the Dual-Space Microscopy technique has super-resolution capability, and can be used to overcome the limitation of Fourier Ptychographic Microscopy technique. Also, a preliminary study of convergence of the Dual-Space Microscopy technique and Fourier Ptychographic Microscopy technique are presented using one-dimensional simulations, which indicates that the Dual-Space image reconstruction algorithm converges to correct periodicity after few iterations, even for periodicities smaller than the Rayleigh resolution limit.

The phase retrieval imaging techniques demonstrated in Chapter IV and V use the digitally controlled Hemispherical Digital Condensers for obtaining low resolution real plane images, and corresponding Fourier plane images with a low numerical aperture. Unlike the plane-wave approximation used in simulations, the LEDs of the source are found to emit a divergent beam of light. It is demonstrated that this divergent emission is the cause for small field-of-view in the reconstructed images in Dual-Space Microscopy technique. This undesirable feature can be removed using a Laser-based inclined-illumination source that can provide a much smaller condenser numerical aperture that can result in larger field-of-view [97, 98]. Unlike single-shot imaging methods, phase-retrieval imaging methods like Fourier Ptychographic

Microscopy and Dual-Space Microscopy are numerically intensive. As large number of images have to be acquired and processed when using these methods, real-time imaging of samples becomes difficult. One of the ways to overcome this limitation is to combine some of the experimentally acquired Fourier plane images, and then process that set with reduced number of images. Such spatial-multiplexing of images acquired by adjacent LEDs has been proposed for Fourier Ptychographic Microscopy technique [99]. However, this only reduces the number of images to be acquired by 50%. Instead, we are working on using the entire row of LEDs in Hemispherical Digital Condensers to illuminate the sample, and use the images acquired by illuminating the object with different rows of Hemispherical Digital Condensers, which can significantly reduce the number of images to be processed – for example, for the Hemispherical Digital Condensers used in Chapter IV and V, the number of image-acquisitions would reduce from 128 images to 8 images. Moreover, on achieving this, variable optical condensers formed in the wet-mounting setup could be utilized for real-time imaging.

BIBLIOGRAPHY

1. C.F. Bohren, D.R. Huffman, Absorption and Scattering of Light by Small Particles, New York, John Wiley & Sons, 1983 (pg. 336).
2. E. Devaux, T.W. Ebbesen, J. Weeber, A. Dereux, Launching and decoupling surface plasmons via micro-gratings, *Appl. Phys. Lett.* 83 (2003) 4936-4938.
3. R.W. Wood. On a remarkable case of uneven distribution of light in a diffraction grating spectrum, *Phil. Mag.* 4, (1902) 396.
4. U. Fano, "The theory of anomalous diffraction gratings and of quasi-stationary waves on metallic surfaces (Sommerfeld's waves)," *J. Opt. Soc. Am.* 31 (1941) 213.
5. D. Bohm, D. Pines, A Collective Description of Electron Interactions. I. Magnetic Interactions, *Phys. Rev.* 82, (1951) 625.
6. D. Pines, Collective Energy Losses in Solids, *Rev. Mod. Phys.* 28 (1956) 184-198.
7. L. Tonks, I. Langmuir, Oscillations in Ionized Gases, *Phys. Rev.* 33 (1929) 195.
8. U. Fano, Atomic Theory of electromagnetic interactions in dense materials, *Phys. Rev.* 103 (1956) 1202.
9. R.H. Ritchie, Plasma Losses by Fast Electrons in Thin Films, *Phys. Rev.* 106 (5) (1957) 874-881.
10. C.J. Powell, J.B. Swan, Origin of the Characteristic Electron Energy Losses in Aluminum, *Phys. Rev.* 115 (1959) 869.
11. E.A. Stern, R.A. Ferrell, Surface Plasma Oscillations of a Degenerate Electron Gas, *Phys. Rev.* 120 (1960) 130.
12. T. Turbadar, Complete absorption of light by thin metal films, *J. Mod. Opt.* 11 (3) (1964) 207-210.
13. A. Otto, Excitation of non-radiative surface plasma waves in silver by the method of frustrated total reflection, *Z. Phys.* 216 (1968) 398.
14. E. Kretschmann, H. Raether, Radiative decay of non-radiative surface plasmons excited by light, *Z. Naturf.* 23 (1968) 2135.
15. R.H. Ritchie, E.T. Arakawa, J.J. Cowan, R.N. Hamm, Surface-plasmon resonance effect in grating diffraction, *Phys. Rev. Lett.* 21 (1968) 1530-1532.
16. S.L. Cunningham, A.A. Maradudin, R.F. Wallis, Effect of a charge layer on the surface-plasmon-polariton dispersion curve, *Phys. Rev. B* 10 (1974) 3342.
17. E. Yeatman, E. Ash, Surface plasmon microscopy, *Electron. Lett.* 23 (1987) 1091-1092.
18. A.T.M. Lenferink, R.P.H. Kooyman, J. Greve, An improved optical method for surface plasmon resonance experiments, *Sensors and Actuators B* 3 (1991) 261-265.
19. H.E. de Bruijn, R.P.H. Kooyman, J. Greve, Surface plasmon resonance microscopy: improvement of the resolution by rotation of the object, *Appl. Opt.* 32 (1994) 2426-2430.
20. C.E.H. Berger, R.P.H. Kooyman, J. Greve, Resolution in surface plasmon microscopy, *Rev. Sci. Instrum.* 65 (1994) 2829-2836.
21. E.M. Yeatman, Resolution and sensitivity in surface plasmon microscopy and sensing, *Biosensors and Bioelectronics* 11 (1996) 635-649.

22. H. Kano, S. Mizuguchi, S. Kawata, Excitation of surface plasmon polaritons by a focused laser beam, *J. Opt. Soc. Am. B* 15 (1998) 1381–1386.
23. P.I. Nikitin, A.N. Grigorenko, A.A. Beloglazov, M.V. Valeiko, A.I. Savchuk, O.A. Savchuk, G. Steiner, C. Kuhne, A. Huebner, R. Salzer, Surface plasmon resonance interferometry for micro-array bio-sensing, *Sens. Actuat. A* 85 (2000) 189–193.
24. A.N. Grigorenko, A.A. Beloglazov P.I. Nikitin C. Kuhne G. Steiner, R. Salzer, Dark-field surface plasmon resonance microscopy, *Opt. Comm.* 174 (2000) 151-155.
25. C.D. Geddes, I. Gryczynski, J. Malicka, Z. Gryczynski, J.R. Lakowicz, Directional surface plasmon coupled emission: a new method for high sensitivity detection, *Biochem. Biophys. Res. Commun.* 307 (2003) 435-439.
26. N. Calendar, Theory and Simulation of Surface Plasmon-Coupled Directional Emission from Fluorophores at Planar Structures, *Anal. Chem.* 76 (2004) 2168-2173.
27. J. Zhang, C.W. See, M.G. Somekh, M.C. Pitter, S.G. Liu, Wide-field surface plasmon microscopy with solid immersion excitation. *Appl. Phys. Lett.* 85 (2004) 5451–5453.
28. T. Velinov, M. Bivolarska, S. Russev, K. Bransalov, M.G. Somekh, Polarization control scheme for surface plasmon and optical guided mode control detection, *Sens. Actuat. B* 100 (2004) 325–332.
29. S.I. Bozhevolnyi, Localization phenomena in elastic surface-polariton scattering caused by surface roughness, *Physical Review B* 54 (1996) 8177-8185.
30. B. Hecht, H. Bielefeldt, L. Novotny, Y. Inouye, D.W. Pohl, Local excitation, scattering, and interference of surface plasmons. *Physical Review Letters* 77 (1996) 1889-1892.
31. I.I. Smolyaninov, C.C. Davis, J. Elliott, A.V. Zayats, Resolution enhancement of a surface immersion microscope near the plasmon resonance, *Opt. Lett.* 30 (2005) 382-384.
32. I.I. Smolyaninov, J. Elliott, A.V. Zayats, C.C. Davis, Far-field optical microscopy with a nanometer-scale resolution based on the in-plane image magnification by surface plasmon polaritons, *Phys. Rev. Lett.* 94(5) (2005) 057401.
33. J.B. Pendry, Negative refraction makes a perfect lens, *Phys. Rev. Lett.* 85 (2000) 3966–3969.
34. D.O.S. Melville, R.J. Blaikie, Super-resolution imaging through a planar silver layer, *Opt. Exp.* 13 (2005) 2127–2134.
35. Z. Liu, H. Lee, Y. Xiong, C. Sun, X. Zhang, Far-field optical hyperlens magnifying sub-diffraction-limited objects, *Science* 315 (2007) 1686.
36. J.B. Pendry, S.A. Ramakrishna, Near-field lenses in two dimensions, *J. Phys. Condens. Matter* 14 (2002) 8463.
37. Z. Liu, S. Durant, H. Lee, Y. Pikus, N. Fang, Y. Xiong, C. Sun, X. Zhang, Far-field optical superlens, *Nano Lett.* 7 (2007) 403–408.

38. S. Durant, Z. Liu, J.M. Steele, X. Zhang, "Theory of the transmission properties of an optical far-field superlens for imaging beyond the diffraction limit." *J. Opt. Soc. Am. B* 23 (2005) 2383–2392.
39. S.P. Frisbie, C. Chesnutt, M.E. Holtz, A. Krishnan, L. Grave de Peralta, A.A. Bernussi, Image formation in wide-field microscopes based on leakage of surface plasmon-coupled fluorescence, *IEEE Photon. J.* 1 (2009) 153–162.
40. D.B. Desai, D. Dominguez, A.A. Bernussi, L. Grave de Peralta, Ultra-thin condensers for optical subwavelength resolution microscopy, *J. Appl. Phys.* 115 (2014) 093103.
41. L. Grave de Peralta, Metal slab superlens - negative refractive index versus inclined illumination: discussion, *J. Opt. Soc. Am. A* 32 (2015) 1729-1735.
42. J.D. Jackson, *Classical Electrodynamics*, J. Wiley and Sons, New York, 1975.
43. J.A. Porto, F.J. Garcia-Vidal, J.B. Pendry, Transmission resonances on metallic gratings with very narrow slits, *Phys. Rev. Lett.* 83 (1999) 2845-2848.
44. G.I. Stegeman, R.F. Wallis, A.A. Maradudin, Excitation of surface plasmons by end-fire coupling, *Opt. Lett.* 8 (1983) 386-389.
45. E. Kretschmann, Die bestimmung der oberflächenrauigkeit dünner schichten durch messung der winkelabhängigkeit der streustrahlung von oberflächenplasmaschwingungen, *Opt. Comm.* 10(4) (1974) 353-356.
46. L. Novotny, B. Hecht, D.W. Pohl, Interference of locally excited surface plasmons, *J. Appl. Phys.* 81(4) (1997) 1798-1806.
47. J.J. Burke, G.I. Stegeman, T. Tamir, Surface-polariton-like waves guided by thin, lossy metal films, *Phys. Rev. B* 33(8) (1986) 5186—5201.
48. D. Sarid, W. Challener, *Modern Introduction to Surface Plasmons: Theory, Mathematica Modeling and Applications*, Cambridge University Press, New York, USA 2010.
49. W.A. Murray, S. Astilean, W.L. Barnes, Transition from localized surface plasmon resonance to extended surface plasmon-polariton as metallic nanoparticles merge to form a periodic hole array, *Phys. Rev. B* 69 (2004) 165047.
50. T. Velinov, M.G. Somekh, S. Liu, Direct far-field observation of surface-plasmon propagation by photo-induced scattering, *Appl. Phys. Lett.* 75 (1999) 3908–3910.
51. K.M. McPeak, S.V. Jayanti, S.J.P. Kress, S. Meyer, S. Iotti, A. Rossinelli, D.J. Norris, Plasmonic films can easily be better: Rules and recipes, *ACS Photonics* 2 (2015) 326-333.
52. S. Ekgasit, C. Thammacharoen F. Yu, W. Knoll, Influence of the metal film thickness on the sensitivity of surface plasmon resonance biosensors, *Appl. Spectrosc.* 59 (2005) 661-667.
53. R.A. Ferrell, Predicted Radiation of Plasma Oscillations in Metal Films, *Phys. Rev.* 111, (1958) 1214.
54. R.H. Ritchie, Surface plasmons in solids, *Surface Science* 34 (1973).
55. I. Gryczynski, J. Malicka, K. Nowaczyk, Z. Gryczynski, J.R. Lakowicz, Effects of Sample Thickness on the Optical Properties of Surface Plasmon-Coupled Emission, *J. Phys. Chem. B* 108 (2004) 12073-12083.

56. M.W. Knight, Y. Wu, J.B. Lassiter, P. Nordlander, N.J. Halas, Substrates Matter: Influence of an Adjacent Dielectric on an Individual Plasmonic Nanoparticle, *Nano Letters* 9(5) (2009) 2188-2192.
57. D. Zhang, Q. Fu, M. Yi, X. Wang, Y. Chen, P. Wang, Y. Lu, P. Yao, H. Ming, Excitation of Broadband Surface Plasmons with Dye Molecules, *Plasmonics* 7 (2012) 309–312.
58. A.N. Grigorenko, P.I. Nikitin, A.V. Kabashin, Phase jumps and interferometric surface plasmon resonance imaging, *Appl. Phys. Lett.* 75 (25) (1999) 3917–3919.
59. M. McGuirk, C.K. Carniglia, An angular spectrum representation approach to the Goos-Hänchen shift, *J. Opt. Soc. Am.* 67 (1977) 103-107.
60. A.V. Kabashin, S. Patskovsky, A.N. Grigorenko, Phase and amplitude sensitivities in surface plasmon resonance bio and chemical sensing, *Opt. Exp.* 17 (2009) 21191-21204.
61. J. Zhang, M.C. Pitter, S. Liu, C. See, M.G. Somekh, Surface-plasmon microscopy with a two-piece solid immersion lens: bright and dark fields, *Appl. Opt.* 45 (2006) 7977-7986.
62. http://www.chromeon.de/images/products/Rhodamine_6G_spectra_big.jpg
63. A. Demetriadou, A.A. Kornyshev, Principles of nanoparticle imaging using surface plasmons, *New J. Phys.* 17 (2015) 013041.
64. H.J. Simon, J.K. Guha, Directional surface plasmon scattering from silver films, *Opt. Comm.* 18(3) (1976) 391-394.
65. A. Drezet, A. Hohenau, D. Koller, A. Stepanov, H. Ditlbacher, B. Steinberger, F.R. Aussenegg, A. Leitner, J.R. Krenn, Leakage radiation microscopy of surface plasmon polaritons, *Materials Science and Engineering: B*, 149 (3) (2008) 220-229.
66. C.J. Regan, R. Rodriguez, S.C. Gourshetty, L. Grave de Peralta, A.A. Bernussi, "Imaging nanoscale features with plasmon-coupled leakage radiation far-field superlenses," *Opt. Exp.* 20 (2012) 20827-20834.
67. D. Dominguez, D.B. Desai, C.J. Regan, R. Lopez-Boada, A.A. Bernussi, L. Grave de Peralta, Observation of coherence-related phenomena in experiments with surface plasmon polaritons excited by fluorescence, *Opt. Comm.* 315 (2015) 270-274.
68. C.J. Regan, O. Thiabgoh, L. Grave de Peralta, A.A. Bernussi, Probing photonic Bloch wavefunctions with plasmon-coupled leakage radiation, *Opt. Express* 20, 8658-8666 (2012).
69. I. Gryczynski, J. Malicka, K. Nowaczyk, Z. Gryczynski, J.R. Lakowicz, Effects of Sample Thickness on the Optical Properties of Surface Plasmon-Coupled Emission, *J. Phys. Chem. B* 108 (2004) 12073-12083.
70. D. Zhang, Q. Fu, M. Yi, X. Wang, Y. Chen, P. Wang, H. Ming, Contrast Enhancement in Fluorescence Microscope by Plasmonic Coupling, *Plasmonics* 7 (2012) 209–214.
71. D.G. Zhang, X.C. Yuan, J. Bu, G.H. Yuan, Q. Wang, J. Lin, X.J. Zhang, P. Wang, H. Ming, T. Mei, Surface plasmon converging and diverging properties modulated by polymer refractive structures on metal films, *Opt. Express* 17(14) (2009) 11315-11320.

72. J.R. Krenn, H. Ditlbacher, G. Schider, A. Hohenau, A. Leitner, F.R. Aussenegg, Surface plasmon micro- and nano-optics *J. Microsc.* 209(3) (2003) 167-172.
73. A. Hohenau, J.R. Krenn, A.L. Stepanov, A. Drezet, H. Ditlbacher, B. Steinberger, A. Leitner, F.R. Aussenegg, Dielectric optical elements for surface plasmons, *Opt. Lett.* 30(8) (2005) 893-895.
74. M.U. Gonzalez, J.C. Weber, A.L. Baudrion, A. Dereux, A.L. Stepanov, J.R. Krenn, E. Devaux, T.W. Ebbesen, Design, near-field characterization, and modeling of 45° surface-plasmon Bragg mirrors, *Phys. Rev. B* 73 (2006) 155416.
75. M.U. Gonzalez, A.L. Stepanov, J.C. Weber, A. Hohenau, A. Dereux, R. Quidant, J.R. Krenn, Analysis of the angular acceptance of surface plasmon Bragg mirrors, *Opt. Lett.* 32 (2007) 2704-2706.
76. C.J. Regan, D. Dominguez, L. Grave de Peralta, A.A. Bernussi, Far-field superlenses without metal, *J. of Appl. Phys.* 113 (2013) 1831051.
77. R. Lopez-Boada, C.J. Regan, D. Dominguez, A.A. Bernussi, L. Grave de Peralta, Fundamentals of optical far-field subwavelength resolution based on illumination with surface waves, *Opt. Express* 21(2013) 11928-11942.
78. D.B. Desai and L. Grave de Peralta, Optical condensers formed in wet-mounting setup, *Appl. Opt.* 54 (2015) 3580-3587.
79. D.B. Desai, M.M.S. Aldawsari, B.M.H. Alharbi, S. Sen, and L. Grave de Peralta, Comprehensive study of unexpected microscope condensers formed in sample arrangements commonly used in optical microscopy, *Appl. Opt.* 54 (2015) 7781-7788.
80. D. Dominguez, M. Alhusain, N. Alharbi, A.A. Bernussi, and L. Grave de Peralta, "Fourier plane imaging microscopy," *J. Appl. Phys.* 116, 103102 (2014).
81. H. Köhler, On Abbe's theory of image formation in the microscope, *Opt. Acta* 28 (1981) 1691-1701.
82. A. Vainrub, O. Pustovyy, V. Vodyanoy, Resolution of 90 nm ($\lambda/5$) in an optical transmission microscope with annular condenser, *Opt. Letters* 31(2006) 2855-2857.
83. G. Zheng, R. Horstmeyer, and C. Yang, Wide-field, high-resolution Fourier ptychographic microscopy, *Nature Photonics* 7 (2013) 739-745.
84. D. Dominguez, L. Molina, D.B. Desai, T. O'Loughlin, A.A. Bernussi, L. Grave de Peralta, Hemispherical digital optical condensers with no lenses, mirrors, or moving parts, *Opt. Express* 22 (2014) 6948-6957.
85. J.W. Goodman, *Introduction to Fourier Optics* (McGraw-Hill, 1968).
86. J.M. Rodenburg, Ptychography and related diffractive imaging methods, *Advances in imaging and electron physics* 150 (2008) 87-184.
87. A.M. Maiden, J.M. Rodenburg, M.J. Humphry, Optical ptychography: a practical implementation with useful resolution, *Optics Lett.* 35 (2010) 2585-2587.
88. A.M. Maiden, M.J. Humphry, F. Zhang, J.M. Rodenburg, Superresolution imaging via ptychography, *J. Opt. Soc. Am. A* 28 (2011) 604-612.

89. R.W. Gerchberg, W.O. Saxton, A practical algorithm for the determination of the phase from image and diffraction plane pictures, *Optik* 35 (1972) 237-246.
90. R. Horstmeyer, C. Yang, A phase space model of Fourier ptychographic microscopy, *Opt. Express* 22 (2014) 338–358
91. K. Guo, S. Dong, P. Nanda, G. Zheng, Optimization of sampling pattern and the design of Fourier ptychographic illuminator, *Opt. Express* 23 (2015) 6171.
92. X. Ou, R. Horstmeyer, G. Zheng, C. Yang, “High numerical aperture Fourier ptychography: principle, implementation and characterization,” *Opt. Express* 23 (2015) 3473.
93. J.R. Fienup, Invariant error metrics for image reconstruction, *Appl. Opt.* 36 (1997) 352-357.
94. X. Ou, G. Zheng, C. Yang, Embedded pupil function recovery for Fourier ptychographic microscopy, *Opt. Express* 22 (2014) 4960-4972.
95. D.B. Desai, M.V. Zhelyeznyakov, M. Alotaibi, L. Grave de Peralta, Using Fourier Ptychographic microscopy for photonic crystal imaging applications, *J. of Optics* (in review).
96. D.B. Desai, M.V. Zhelyeznyakov, S.A.S. Alanzi, L. Grave de Peralta, Simulation study of dual-space microscopy, *Appl. Opt.* 55 (2016) 7294-7300.
97. D.B. Desai, S. Sen, M.V. Zhelyeznyakov, W. Alanzi, L. Grave de Peralta, Super-resolution imaging of photonic crystals using the dual-space microscopy technique, *Appl. Opt.* 55 (2016) 3929-3934.
98. C. Kuang, Y. Ma, R. Zhou, J. Lee, G. Barbasathis, R.R. Dasari, Z. Yaqoob, P.T. So, Digital micromirror device-based laser-illumination Fourier ptychographic microscopy, *Opt. Express* 23 (2015) 26999–27010.
99. L. Tian, X. Li, K. Ramchandran, L. Waller, Multiplexed coded illumination for Fourier ptychography with LED array microscope, *Biomed. Opt. Express* 14 (2014) 3093.
100. S. Sen, D.B. Desai, M.H. Alsubaie, M.V. Zhelyeznyakov, L. Molina, H. Sari-Sarraf, A.A. Bernussi, L. Grave de Peralta, Imaging photonic crystals using Fourier plane imaging and Fourier ptychographic microscopy techniques implemented with a computer controlled hemispherical digital condenser, *Opt. Comm.* 383 (2017) 500-507.